Spring 4-19-2021

Handling and Manipulation of Water- and Air- Borne Biological Samples Using Liquid-Infused Surfaces

Daniel P. Regan
University of Maine, daniel.regan@maine.edu

HANDLING AND MANIPULATION OF WATER- AND AIR- BORNE BIOLOGICAL SAMPLES USING LIQUID-INFUSED SURFACES

By

Daniel P. Regan

B.S. Miami University, 2017

A DISSERTATION

Submitted in Partial Fulfillment of the

Requirements for the Degree of

Doctor of Philosophy

(in Biomedical Engineering)

The Graduate School of Biomedical Science and Engineering

The University of Maine

May 2021

Advisory Committee:

Caitlin Howell, Assistant Professor of Chemical and Biomedical Engineering, Advisor

Michaela Reagan, Faculty Scientist II at Maine Medical Center Research Institute

Andre Khalil, Professor of Chemical and Biomedical Engineering

Douglas Bousfield, Professor of Chemical and Biomedical Engineering

Richard Corey, Director of the VEMI Lab

HANDLING AND MANIPULATION OF WATER- AND AIR- BORNE BIOLOGICAL SAMPLES USING LIQUID-INFUSED SURFACES

By Daniel P. Regan

Dissertation Advisor: Dr. Caitlin Howell

An Abstract of the Dissertation Presented
in Partial Fulfillment of the Requirements for the
Degree of Doctor of Philosophy
(in Biomedical Engineering)
May 2021

Research on novel materials to handling water- and airborne samples for biological threats analysis is in great demand due to the COVID-19 pandemic. Work conducted on a new field of material science, called liquid-infused surfaces, demonstrate strong potential for the handling and manipulation of biological samples. As a result of the field's infancy, only a limited number of studies have explored how liquid-infused surfaces can apply droplet manipulation strategies to address real-world problems. Presented in this dissertation are two platforms that leverage liquid-infused surfaces to address the challenges associated with handling water- and airborne biological samples. When dealing with waterborne biological samples, the paper-based materials commonly used in point-of-care devices rely on capillary forces to drive droplet movement, but this mechanism can result in significant sample loss. To simultaneously localize and concentrate with minimal loss, liquid-infused surfaces were fabricated by infusing silicone release paper with polydimethylsiloxane oil. Functionality was provided by folding the polymer surfaces into 3D geometries of the sample which enabled clean separation into predefined locations. The liquid-infused surfaces permitted ~3.4-fold increase in

concentration of bacterial samples within a material that resisted adhesion, enabling downstream analysis. To capture airborne biological samples, many current methods suffer from pathogen recirculation, harsh chemical extraction protocols, and retention of captured airborne pathogens. Here, liquid nets are explored as a new method of filter-based air sampling, focused on improving the release of capture bioaerosols. Liquid nets were fabricated with traditional liquid-infused surface materials, polytetrafluorethylene (PTFE) filters were infused with perfluoropolyether oil, as well as melt-blown polypropylene high-efficiency particulate air (HEPA) filters wetted with perfluoropolyether oil. The PTFE liquid nets significantly improved the rate at which the captured *Escherichia coli* aerosol droplets were transferred for culturing on agar plates compared to the bare PTFE controls. Similarly, results from the HEPA filters demonstrated that the liquid nets improved the release of the captured *E. coli,* in comparison to the bare HEPA filters. The improvements to bacterial transfer provided by liquid nets present a new filter-based air sampling method to capture and detect biological threats within the surrounding environment.

DEDICATION

To the public health personnel on the front lines, thank you.

ACKNOWLEDGEMENTS

First, I would not be where I am today with the love and support of my family. It is not often that a son or daughter says they are going to work on a doctorate, let alone to do so in a state where the moose population outnumbers that of its largest city. I would like to thank the Graduate School of Biomedical Science and Engineering, especially my mentor Dr. Caitlin Howell, for giving me an opportunity when no one else would. I am grateful to have a mentor that let me drive the direction of my dissertation to match my passion and future career aspirations.

I would be remiss if I did not mention the incredible support network and group of mentors that I have been fortunate to gather along my various journeys. To the Buckeye Boys State Counselor Staff and the American Legion, the scout leaders of Troop 221, coaches, and St. Charles Borromeo Parish, thank you for giving me a space to mature as a young man. To Ms. Hara and Mr. Jeckel, thank you for giving me chance to find my passion for biotechnology and engineering. To the United States Senate Youth Program, thank you for believing in me and showing a kid from Cleveland what a future in public service could look like. To the Department of Chemical, Paper, and Biomedical Engineering at Miami University, thank you for valuing students and reminding of the impact bioengineers can have. To Dr. Zeb Baker and Randi Thomas, Esq. thank you for treating students like family and going above and beyond to make our experience one of a kind. To Dr. Michael Kennedy, thank you for giving me my start as a researcher.

TABLE OF CONTENTS

LIST OF TABLES

LIST OF FIGURES

CHAPTER 1

INTRODUCTION TO MANIPULATION STRATEGIES ON BIOLOGICAL SAMPLES

There is a large and growing need for low-cost, portable, and durable devices which can provide information on the presence and composition of biological and chemical materials in our environment.[1,2] Multi-drug resistant bacteria[3,4] in hospital-acquired and secondary infections[5,6] pose a substantial threat to human health, as do the inevitable outbreaks of bacterial and viral epidemics such as Ebola, cholera, and Zika.[7] Through the work of many researchers, companies, and communities, these threats have been met with innovation in point-of-need (PON) detection systems which monitor biomarkers or other indicators of airborne biological threats. Currently, simple PON devices are widely used as both paper and other disposable assays,[8] while advances in synthetic biology[9] and engineering of microfluidic devices[10,11] are showing tremendous promise for expanded capabilities in the future. Yet despite these advancements, there remain several major challenges to realizing the full capability of on-site detection systems for both waterborne and airborne samples.

PON detection platforms are designed to provide information that enables a decision for a course of action at the site of need. However, the results delivered by current widely available platforms suffer from a lack of either specificity or precision, often requiring that samples be sent to brick-and-mortar laboratories for further testing.[1,2,12] At the same time, more specific and precise approaches to detection being developed in laboratories around the world face the challenge of scale-up[1,2,13] and the current lack of established validation protocols.[8,13] In addition, a fully integrated system which combines sample preparation and analysis would likely facilitate the use of PON devices; however, when dealing with heterogeneous biological or

environmental materials the complexities associated with handling, mixing, and transport are noteworthy.[1,13,14]

Beginning to approach the challenges associated with enabling the next generation of PON testing devices will require technology that is by its nature integrative, adaptive, and versatile. Although multiple solutions will doubtlessly be required, one such approach that has recently generated attention is the use of liquid-infused surfaces, often referred to as either slippery liquid-infused porous surfaces (SLIPS) or lubricant-impregnated surfaces (LIS). Inspired by bio-active and dynamic wet surfaces in nature,[15,16] this platform technology is proving to be adaptable to multiple applications, including the control of biological materials,[17–19] medical surfaces[16,20,21] and droplet movement.[22–24] Furthermore, liquid-infused surfaces are more often being used as a method of facilitating synergy between multiple functionalities such as anti-adhesion, environmental responsiveness, self-healing capabilities, and surface chemistry control.[16]

1.1. Droplet Interactions with Liquid-Infused Surfaces

Liquid-infused surfaces are created by trapping a thin layer of liquid on a surface through a combination of physical means, such as capillary action, and chemical means, such as van der Waals forces.[25] When the trapped liquid is immiscible with a given contaminant, the resulting liquid layer presents an anti-fouling surface which is pressure stable and even able to self-heal due to its liquid nature.[15] An in-depth discussion of the physics and chemistry behind liquid-infused surface can be found in any one of several recent reviews on the subject;[16,26,27] however, one of the attractive properties of these surfaces is their ability to be created on a wide range of substrates, from polymers to metal to paper, using different types of infusing

liquids.[16,28,29] In all cases, droplet interactions with fully-functional liquid-infused surfaces are characterized by a low contact angle hysteresis (CAH ≤ 10°), or the difference between the receding and advancing contact angles of a droplet sliding along the surface. This measurement can be viewed as proportional to the energy required to shift a droplet from a static to dynamic state, and is generally used to illustrate the ease with which droplets can be translated from one location to another.[30]

While immiscibility of the infusing liquid with the sliding droplet is critical for the system to work, the way in which the droplet interacts with the liquid layer is variable. Recent investigations using confocal optical interferometry[31] have revealed three possible equilibrium states for a droplet at rest interacting with a liquid layer: one in which the infusing liquid is fully displaced and the droplet makes full contact with the surface (failure); one in which the liquid is partially displaced and the droplet makes contact with several discrete areas on the surface (partial failure); and a final one in which the liquid layer remains congruent underneath the droplet, allowing the droplet to effectively hydroplane/oleoplane across the surface (functional). Which state a liquid infused surface/droplet pair will produce depends greatly on the composition of the liquid as well as the composition and texture of the solid surface. However, the stability of any given combination of solid substrate, infusing liquid, and impinging fluid under static conditions can be predicted via a spreading parameter, which takes into account the surface and interfacial energies.[32] It has also been demonstrated that putting the droplet into motion can alter a partially-failed state into a fully functional state. In this case, the stability of the liquid-infused surface under dynamic conditions can be predicted by the Landau-Levich-Derjaguin law, where film thickness is related to the capillary number of

the system.[31] When droplets are in motion across a liquid-infused surface, the speed with which they travel can be tuned by altering the viscosity, with more viscous infusing liquids slowing the rate of motion.[33]

Additional studies on liquid layer/droplet interaction have looked into a unique set of phenomena that occur on liquid-infused surfaces: the creation of a wetting ridge (or wetting skirt), the displaced infusing-layer liquid which rises up partially around the droplet; and the wrapping layer, the thin encapsulation film of the infusion liquid around the droplet (**Figure 1.1**).[34–36] Both of these phenomena have been shown to affect evaporation rates of the drop,[34] and

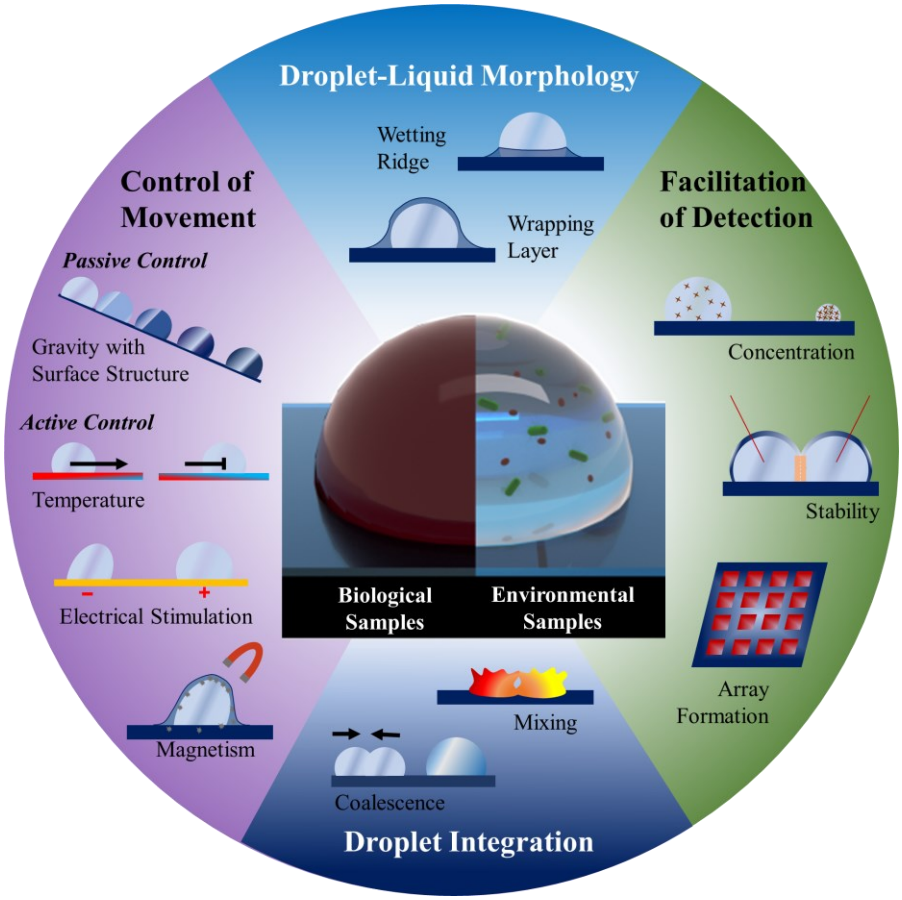

Figure 1.1. Schematic illustration of the different morphologies, movement control methods, and detection-facilitating properties of droplets on liquid-infused surfaces.

increase the rate of stripping of the infusing liquid from the surface when the droplet falls off of the infused surface, bringing its wetting ridge and wrapping layer with it.[35,36] Whether or not a wrapping layer forms can be tuned by selecting specific infusing-repelling liquid pairs, although this is most achievable when repelling other low-surface-tension liquids.[32,37]

In the application of liquid-infused surfaces, particularly in anti-fouling capacities, much attention has been given to the understanding and improvement of their self-healing capabilities and ultimate longevity.[16,38] Attempts at limiting the rate of depletion of the infusing liquid by liquid layer stripping have recently included increasing the viscosity of the infusing layer to slow or prevent wetting ridge and wrapping layer formation,[37] creating a system of vascularized channels within the surface substrate that can be filled with the infusing liquid to continually self-replenish the depleted liquid layer,[39] building in self-secreting droplet reservoirs[40–42] adding amphiphilic porous cellulose nanofibers to the surface microstructure to act as infusing-layer reservoirs and provide additional capillary force to retain the infusing liquid,[43] and adding a brush-like low molecular weight PDMS graft over initial surface and spin coating the infusing layer to increase the robustness of the layer.[44] Other options to address longevity have looked to tuning the crosslinking density of infused polymers, which have been shown to have an effect of longevity in the face of repeated removal of the infusing liquid overlayer.[45]

While not yet investigated with individual droplets, there have been several reports of modifying either the repelling liquid or the solid to introduce an additional degree of functionality to the system. For example, work responding to the need for liquid-infused surfaces to not only resist adhesion by contaminating bacteria, but also prevent them from

multiplying was addressed by using and infusing liquid doped with bacterial quorum sensing inhibitors,[46] the antimicrobial agent triclosan[47] or nitric oxide.[48] The doped liquid was found to release the active molecules slowly over time, producing the desired dual response. Another potential concern with liquid-infused surfaces is the entrainment of organic molecules into the infusion layer. A recently reported method to address this issue is to graft a photocatalyst, like titanium dioxide, onto the solid surface. Upon contamination of the infusing layer, UV illumination of the liquid-infused surface photocatalytically decomposed the organic contaminants.[49] Further advances in controlled release and incorporation of active molecules in the infusing liquid layer may also present an interesting opportunity to achieve multi-faceted responses in the interaction of droplets containing biological or environmental samples with liquid interfaces.

1.2. Droplet Manipulation on Liquid-Infused Surfaces

One critical issue in the creation of self-contained PON detection platforms is development of methods to incorporate both sample preparation and detection within the same small area. Preparation steps may require sample separation, mixing with buffers or reagents, or concentration, while detection likely requires movement along a path to a detection site, as has been demonstrated for some PCR applications.[50,51] Current research on droplet manipulation on liquid-infused surfaces offers several promising approaches which may prove useful in further achieving this goal.

1.2.1. Passive Control via Surface Structure Modification

Surface structure or texture is a crucial element of liquid-infused surfaces, and is one of the most accessible parameters to alter to achieve controlled droplet movement. For example,

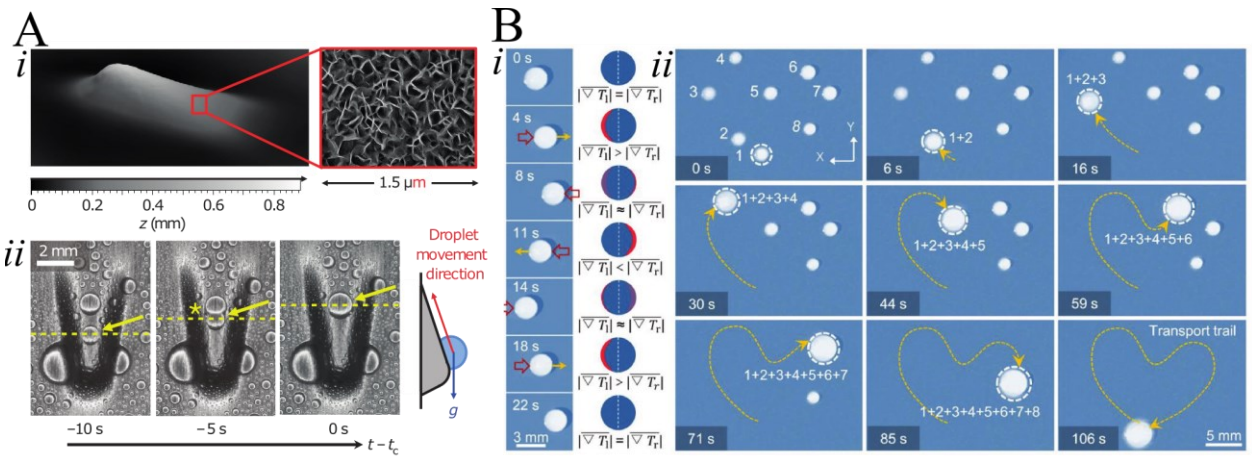

Figure 1.2. A) ***i*** A profilometer image (oblique view) showing nanostructure (inset) infused with lubricant, and the tangentially connected bottom slope. ***ii*** Time-lapsed optical images of condensed water droplets on an asymmetric bump rotated 180° relative to gravity. The yellow asterisk indicates coalescence with another drop, while the dotted yellow line tracks the vertical progress of the droplet. Reproduced with permission.[52] Copyright 2016, Macmillan Publishers Limited. B) ***i*** Time-sequence images (top view) of reversible light-induced motion of a water droplet (≈5 μL) on a horizontal POS. Insets show schematic in top view of ∇T changes within droplet. ***ii*** Time sequence images (top view) of sequentially light-induced coalescence of droplets on POS. There are eight water droplets (numbered with 1–8, volume of each droplet varies between ≈3 and 5 μL). Droplet 1 can be moved to coalesce with droplet 2 and sequentially coalesce with others to form a larger droplet along a designed "heart"-shaped trajectory in 106 s. Yellow dashed lines in each image indicate transport trail of droplet. Reproduced with permission.[65] Copyright 2018, Wiley-VCH.

creating liquid-coated convex asymmetric structures at the millimeter scale, as seen in **Figure 1.2A**, led to six-fold increase in accumulative droplet growth (coalescence) over flat controls, and could also induce droplet transport, which moved opposite the force of gravity.[52] A further liquid-infused surface fabricated on a stretchable elastomer with aligned microscale wrinkles was found to accelerate droplet coalescence in the direction of alignment.[53] Stretching was also used in conjunction with liquid-infused surfaces made with inverse opal patterning as a method of reporting the wetting state of the surface. Upon stretching, the wetting state transitions from one in which the liquid layer is present on top of the surface structure to one in which the surface structure is exposed. At this point the droplet pins to the surface and a color change due

to the disruption in transparency of the inverse opal film is visible.[54] Other approaches have made use of structured surface gradients such as V-shaped ramps to influence droplet motion.[55] Mathematical modeling of these systems was used to predict the interfacial tension and therefore the speed with which the droplet was driven along the gradient.[56] A different strategy using gravitational forces was implemented in an omnifluidic device. Using a titanium dioxide nano-textured surface, microchannels were created within the liquid-infused surface via UV exposure in defined patterns. This set-up resulted in solvents with less affinity for the infusing layer than the surface displacing the liquid and entering the microchannel for gravity-driven transport and droplet mixing.[57] In another method of controlling droplet movement, polyelectrolyte films in a layer-by-layer assembly were patterned on an otherwise flat film. When infused and then subjected to mild shear stress, the infusing liquid was depleted from the flat areas while remaining on the textured areas. Droplets moving along the surface would pin on the flat regions, but continue to move over the textured regions, resulting in a guided pathway.[58] A defined-pathway approach using a liquid-infused surface was also described for directing the movement of underwater bubbles.[59] an approach which may prove useful in the PON testing of gaseous compounds.

1.2.2. Active Control via Temperature

Active control of liquid droplets can be achieved using stimulus-response platforms.[60] and when combined with liquid-infused surfaces offers a range of possibilities for dynamic and complex droplet-handling systems. Liquid-layer-facilitated droplet manipulation via thermal stimuli was the first method to branch out from the passive structural approach. Exposure to temperatures exceeding 200 °C was found to increase droplet velocity by 1,000 times compared

to a room-temperature control.[61] A study using a gradient from 70 °C to 20 °C showed a similarly increased droplet velocity, changing by a factor of five from the cool end to the warm end.[62] Surfaces with temperature-controlled tunable wettability have also been developed using paraffin wax as the infusing "liquid". Transition between the cool, solid wax and the warm liquid wax resulted in a change from pinned to free-moving droplet.[63,64] Tuned light scattering due to the transition in state of the wax was used as a method for self-reporting of wettability transition states with these surfaces.[63] Temperature gradient drivers for droplet motion have also been created using near infrared-light irradiation (NIR) on infused photoresponsive organogels which incorporated Fe_3O_4 in the liquid layer.[65] Illumination with NIR light resulted in localized temperature gradients, which could be used to influence the pathway of the droplet. An advantage of the photoresponsive organogel is that it retains the ability to stimulate droplet movement in a fully reversible manner. This setup allowed for sequential droplet coalescence and real-time droplet guidance (**Figure 1.2B**).

1.2.3. Active Control via Electrical Stimulation

In addition to temperature, electrical stimulation has also emerged as a method to manipulate droplet motion on liquid-infused surfaces. When using reduced graphene oxide films as the surface substrate, voltage pinning was achieved below 10 V for water droplets and below 2 V for KCl droplets.[66] Other work used silicone oil as an infusing liquid on a fluorinated membrane coated with a fluorinated silane self-assembled monolayer.[67] In this unique setup in which the surface chemistry was mismatched with the infusing liquid chemistry (in contrast to most other liquid-infused surfaces where the surface and liquid chemistry are similar), the voltage required to change the contact angle of a droplet on the surface was reduced from >100

V to 5 V presumably due to the ease with which the mismatched chemistry allowed dewetting of the surface. Beyond voltage pinning and manipulation of contact angles, liquid-infused surfaces have also been used to facilitate the manipulation of the shape and dynamics of droplets. Liquid-infused dielectric elastomers akin to muscle tissue were used to elongate droplets vertically, cause oscillations within the droplet, induce accelerated multi-droplet collisions and mixing, and even propel of droplets vertically off the surface (**Figure 1.3A)** by inducing substrate oscillations from 23 to 261 Hz.[68] Further

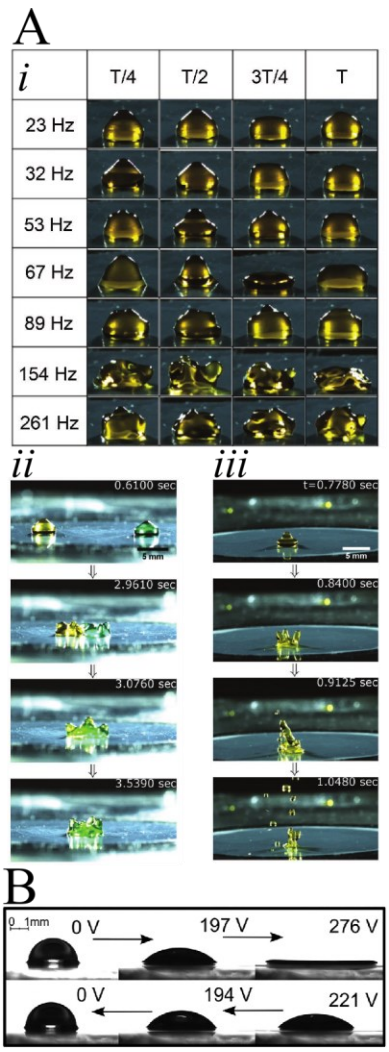

Figure 1.3. A) ***i*** Pictures showing the different oscillation modes of a 20 μL water droplet on a horizontally placed dynamically actuated poroelastic film at frequencies ranging from 23-261 Hz with voltage amplitude of 14 kV. Four pictures for each mode of self-oscillation at a time interval of a quarter of the periodicity *T*. ***ii*** Pictures before, during and after the mixing of two 20 μL droplets on the dynamic poroelastic film actuated at 147 Hz frequency and 12 kV voltage. ***iii*** Pictures in time sequence showing jetting of a 20 μL water droplet placed on the dynamic poroelastic film actuated at 154 Hz frequency and 16 kV voltage. Reproduced with permission.[68] Copyright 2018, Wiley-VCH. B) Side view images of a droplet of glycerol on a spiral dielectrowetting device. Reproduced with permission.[69] Copyright 2017, AIP Publishing.

work showed that exposing a liquid-infused surface created on gold to a 275 V electric field could reversibly deform a droplet into a thin film, as seen in **Figure 1.3B**.[69] The improvement of digital microfluidics represents another potential application of liquid-infused surfaces.[70] Building off of traditional microfluidics, digital microfluidics incorporate electrode circuits to manipulate droplets electrostatic forces. Digital microfluidic devices could have their droplet control mechanisms optimized with the integration of a liquid-infused surface. Surface acoustic wave technology combined with liquid-infused surfaces[71] may improve upon the introduction and work-flow of pump-based microfluidic cell sorters, especially in regards to the introduction of a sample into the device.[72]

1.2.4. Active Control via Magnetism

While temperature and electrical control of droplets on liquid-infused surfaces have proven versatile, several recent works have demonstrated the capabilities of magnetically-driven systems as a method to achieve unique outcomes with droplet and even particles. In a magnetically-actuated liquid-infused system, the liquid is infused with magnetic nanoparticles to create a ferrofluid which can be moved and shaped when exposed to a magnetic field. When moving droplets across such a surface, the wrapping layer plays a critical role as its encapsulation of the droplet allows the ferrofluid to act as a vehicle to be manipulated by magnetic fields. Using this approach, even weak magnetic fields are able to vertically elongate droplets, induce droplet coalescence (**Figure 1.4A**), and guide droplet movement.[73] Using a ferrofluid layer covering a hexagonal nickel array, micro particles could be segregated into discreet groups by magnetically depleting the ferrofluid in the center of each hexagon, as seen

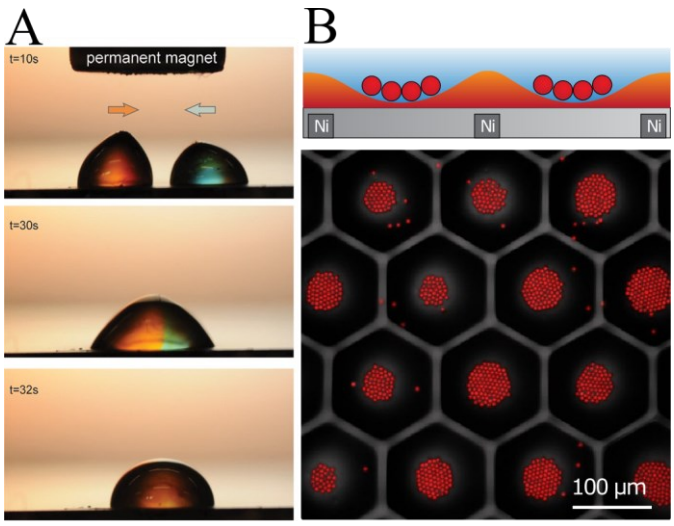

Figure 1.4. (A) Two water droplets (dye used to color droplets) are placed on ferrofluid-infused surface. A magnet is lowered vertically directly between droplets and causes them to move toward one another and coalesce. Reproduced with permission.[73] Copyright 2014, AIP Publishing. (B) Schematic (top) and confocal fluorescence (bottom, showing top view) images showing the confinement of colloidal particles by the macro-topographical response of a thin layer of ferrofluid alone and the confinement of colloidal particles. Schematics are not shown to scale. Reproduced with permission.[74] Copyright 2018, Macmillan Publishers Limited.

in **Figure 1.4B**.[74] A further study examined the effects of the strength of the magnetic field and the concentration of the ferrofluid on droplet moment, finding that these parameters can be tuned to control the speed of gravity-driven droplets as well the degree of stick-slip movement.[75] This work also found nonlinear friction at work in droplets moving across ferrofluid-infused surfaces due to the presence of the wetting ridge, suggesting an interesting new set of tunable parameters for complex droplet manipulation strategies which may facilitate unique PON detection approaches.

1.3. Use for Detection Facilitation

The ability of liquid-infused surfaces to facilitate detection has only recently begun to be explored. For this reason, despite the promise of the active control of droplets on liquid-infused surfaces, applications have mainly used passive droplet control. However, the breakthrough potential demonstrated by passive liquid-infused surfaces in detection scenarios suggests a promising future of applications using active droplet control.

In one of the first reports of the use of liquid-infused surfaces to facilitate detection, sub-femtomolar analyte detection via surface-enhanced Raman scattering (SERS) was made possible due to the ultra-low friction surfaces presented by liquid-infused materials.[76] Droplets containing extremely dilute concentrations of a model analyte were concentrated via

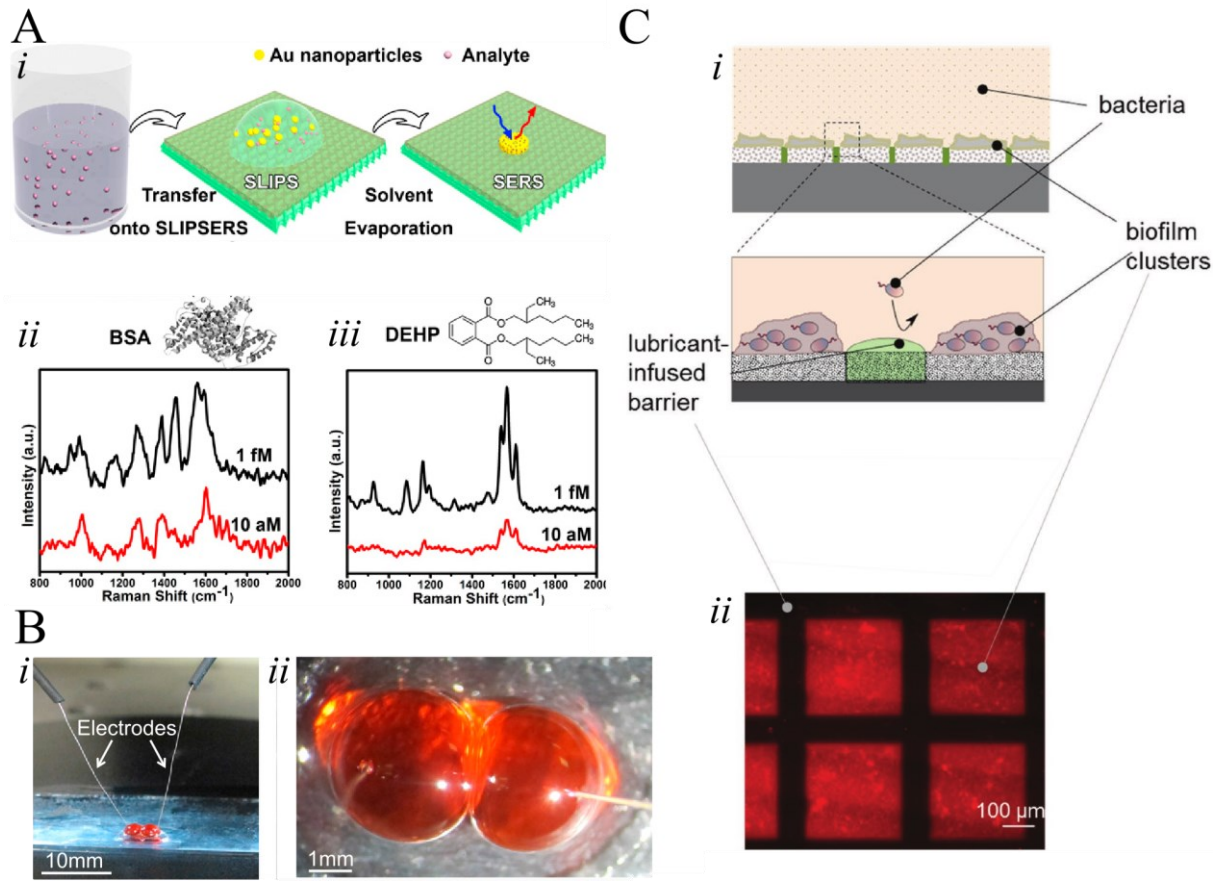

Figure 1.5. (A) Liquid-phase detection of biological species and environmental pollutants using SLIPS and surface-enhanced Raman spectroscopy (SERS): ***i*** Schematic illustration of the liquid phase detection. ***ii*** BSA in water. ***iii*** DEHP in ethanol. Reproduced with permission.[76] Copyright 2016, the National Academy of Sciences of the United States of America. (B) ***i*** Side-view and ***ii*** top-down photographs of noncoalescing water droplets with inserted electrodes. Reproduced with permission.[77] Copyright 2014, the National Academy of Sciences of the United States of America. (C) Formation of patterned liquid surfaces: ***i*** Bacteria cultured on the substrate adhere to the hydrophilic areas but are repelled by the SLIPS regions. ***ii*** Fluorescence staining and image analysis of P. aeruginosa biofilm on hydrophilic squares separated by SLIPS barriers. Reproduced with permission.[79] Copyright 2016, Wilev-VCH.

evaporation on an infused surface. The low friction of the surface allowed all of the analyte molecules to remain within the shrinking droplet, rather than getting pinned at the edges in a coffee-ring effect. After all the solvent evaporated away, the concentrated point of analyte molecules was able to be detected using surface-enhanced Raman scattering (**Figure 1.5A)**.

In a second breakthrough, a platform was designed to monitor diffusion across a lipid bilayer formed between non-coalescing droplets.[77] This setup took advantage of an inherent wrapping layer to create two stable droplets on the liquid-infused surface. When the droplets contained phospholipids, it was found that the lipids would migrate toward the interface between the two droplets and replace the wrapping layer, creating a stable bilayer. Importantly, this droplet- supported bilayer was stable in air under ambient temperature and pressure, as opposed to the previous requirement that the entire system be submerged in oil to maintain the integrity of the lipid layer. Initial measurements on these supported bilayers included measuring single-channel gating events across the membrane using standard electrodes (**Figure 1.5B)**, demonstrating sensitivity in addition to stability, which may be useful in PON detection of aerosols.

The rise of multi-drug-resistant pathogens poses a number of challenges, some of which may be addressed with earlier detection. Toward this goal, a third breakthrough saw the use of liquid-infused surfaces as templates to create liquid-liquid micro-patterns though guided liquid displacement.[78] When exposed to bacteria, discreet biofilm micro-clusters with defined geometries such as those shown in **Figure 1.5C** could be formed.[79] High-throughput PON antibiotic susceptibility test using this approach could play an important role in speeding effective treatment and controlling the spread of resistant microorganisms.

1.4. Conclusions

With the increasing level of danger posed by antibiotic resistance, environmental contamination, the spread of infectious diseases, and harmful applications of synthetic biology, technologies which provide more efficient and more effective ways of providing information at the point of need will be increasingly in demand. The ability of liquid-infused surfaces to enable the control of droplet movement both passively and actively, as well as facilitate detection through liquid manipulation methods not possible on solid surfaces, provides a new set of tools for enabling efficient and effective PON detection systems and may be useful in improving the performance of existing technologies.

As liquid-infused surface technology has only recently come to the forefront as an effective and versatile droplet manipulation method, the creative application and adaptation of these systems is an underpopulated area ripe for research. For example, open-channel analyte[80] and gas-exchange[81] detection platforms could benefit from liquid-infused surfaces which limit sample loss via evaporation or surface adhesion, while simultaneously providing a method of sample concentration. The range of molecules being detected, and methods of biological sample analysis conducted by potentiostat-based bandages[82,83] could be expanded due to the ability of liquid-infused surfaces platforms to resist adhesion by complex biological samples. Environmental testing using multi-droplet analysis[84] could benefit from the electrically- and magnetically-controlled liquid-infused platforms to facilitate droplet translation and mixing. And finally, current detection platforms which handle and manipulate microliter sample volumes could be conducted in an open-channel analysis format without risk of rapid

evaporation. In these applications and others, liquid-infused surfaces may prove one of the keys necessary to develop the PON detection systems of the future.

1.5. Acknowledgements

This chapter has been based on work previously published in *Current Opinions in Colloid and Interface Science*, doi: 10.1016/j.cocis.2019.01.012; authors: Daniel P. Regan and Caitlin Howell.

CHAPTER 2

FABRICATION OF LOW-COST PAPER-BASED PLATFORMS

2.1. Introduction

Paper is currently a prominent and versatile platform on which to create POC technologies due to its low cost, portability, and wide availabilty.[10,85–87] Paper, a renewable and biodegradable resource, is widely used in biotechnological applications ranging from relatively simple microfluidics[87–89] to complex analytical devices,[90–93] many of which are either already in or actively being moved to market.[86,94] Further expanding the use of paper-based technology will require addressing current limitations of the platform. For example, nearly all paper-based systems rely on capillary action to move fluid from one location to another. Although this completely passive approach to liquid handling is beneficial in that it does not require pumping or other energy input, the distribution in diameter and length of the natural fibers that comprise paper can result in the delivery of an inconsistent volume of liquid to the detection site,[86] and can cause a volume loss of up to 50% as the pores of the paper substrate are filled with the sample liquid.[91] While this may not affect tests in which the sample volume is large, it may hinder the use of paper-based POC tests in which the sample volume is expected to be small or in which there is a low concentration of analyte present. In addition, the fibrous nature of paper hinders the flow of large particles, making it difficult to transport cells over distances without significant losses.[95] While traditional laboratory procedures like centrifugation and filtration are efficient methods of bacterial sample preparation, they are often not engineered for operation in resource-limited settings where power-free operation and portability are among the top design constraints.

As discussed in **Chapter 1**, liquid-infused surfaces have recently generated interest as a class of materials which can be used to repel a wide range of biologically-relevant fluids,[16,21] as well as mammalian cells[17,96] and bacteria.[18,39] These systems make use of a thin layer of immiscible liquid immobilized on the surface of a chemically-matched polymer, which is saturated with an excess amount of the liquid and serves as a reservoir to replenish the surface when it becomes depleted.[19,39,40,41,45,97] The type of infusing liquid can be selected from a range of options based on the intended application, but non-toxic silicone oils are often used together with polydimethylsiloxane (PDMS) polymers as both are relatively low-cost, widely available, and immiscible with water-based biological samples. In studies on infused polymers, the samples are frequently solid polymer blocks[39,41,44,98–100] or coatings for rigid materials such as glass[96] or plastic,[17] despite the fact that such polymers can be used to coat a variety of different flexible materials, including fabric[101] and paper.[59]

In this chapter, paper substrates are synergistically combined with infused polymer surfaces in an effort to expand the capabilities of paper-based fluid handling systems for complex samples. Results from surface characterization tests show that the low adhesion properties of liquid-infused surfaces are preserved when fabricated on a range of different paper substrates, including a commercially-produced silicone release paper. With a suitable paper substrate to fabricate liquid-infused surfaces, the next chapter will leverage the paper's foldability to manipulate waterborne samples.

2.2. Fabrication of Liquid-Infused Surfaces

Samples of paper measuring 26 cm^2 (5.1 cm × 5.1 cm) were sourced from Staples multipurpose copier paper, Whatman #1001-240 11 μm filter paper, HP brochure paper 180g,

and Leneta RP-1K silicone release paper (SRP). To fabricate liquid-infused polymers, Sylgard 184 PDMS was mixed in a 10:1 ratio of base to crosslinker and manually coated onto samples of paper (with the exception of the pre-coated SRP) using a 9.5 mm stainless steel applicator rod with a wet film thickness of 102.5 μm. Blocks of 10:1 PDMS were prepared by pouring the mixture into petri dishes and degassing the mixture under vacuum for 30 minutes. The curing of all PDMS surfaces was performed at 70°C in an Isotemp 60L Oven FA (Thermo Fisher Scientific, Pittsburgh, PA) for three hours followed by immersion in 10 cSt PDMS oil for 24 h to infuse samples and form the liquid layer. Once removed from the PDMS immersion, oversaturation of the PDMS oil was removed by tilting the samples vertically to allow run-off.

2.3. Characterization of Liquid-Infused Surfaces

2.3.1. Materials and Methods

A dyed 50 μL water droplet (200uL FD&C Blue #1 dye in 50mL of water) was placed onto each of the dry control surfaces and liquid layer surfaces and images were taken with an EOS Rebel T5 camera (Canon, Taipei City, Taiwan). Contact angle measurements from each surface image were collected using the low-bond axisymmetric drop shape analysis ImageJ plug-in.[102] Sliding angle measurements were collected on dry (n=5) and liquid layer (n=5) squares (5.1 cm x 5.1 cm) for both SRP and PDMS. These samples were placed onto an adjustable angle stage, initially positioned at 0° relative to the benchtop. A 30 μL droplet of deionized water was pipetted onto the sample surface and the stage was manually tilted until the sustained droplet movement across the surface was observed, upon which the digital angle gauge's reading was recorded. Droplet speed measurements of the dry control (n=5) and liquid layer (n=5) SRP and PDMS samples were conducted on the tilt stage at a fixed angle of 30°

relative to the benchtop. A 30 μL droplet of deionized water was pipetted onto the sample surface and a stopwatch was used to time the interval between when the leading edge of the droplet crossed the start and finish demarcations, spaced 6.4 cm apart. The rate of uptake for the PDMS oil into SRP was calculated as the SRP's change in mass over time (**Fig. A.1**). Sliding angle and droplet racing measurements were collected on dry (n=1) and liquid-infused (n=1) squares (5.1 cm x 5.1 cm) for the printer paper, brochure paper, and filter paper (**Fig. A.2**). The same protocol listed above was used for these tests with one exception, the droplet racing was performed at a fixed 15°, compared to the above 30° relative to the benchtop.

2.3.2. Results and Discussion

To test the versatility of liquid-infused polymer system on paper, we fabricated liquid layers on four different types of paper substrates. The first three substrate types were standard printer paper, brochure paper, and filter paper; all of which were hand-coated with a ~100 μm overlayer of a standard PDMS polymer (Sylgard 184) using a draw-down bar to control thickness. The fourth substrate type was a commercially available SRP, which came pre-coated with a thin layer of siloxane for a total sheet height of 127 μm. **Figure 2.1A** shows images of the four substrates before coating (above) and after coating and infusing with a PDMS liquid (below) to create the liquid-infused surface.[39,45] A droplet of dyed water is included to demonstrate the change in surface properties before and after coating and infusion. As expected, before infusion the water droplet eventually soaked into all paper substrates except for the SRP, where it was prevented from doing so by the siloxane coating. After coating and infusion, the contact angle of the dyed water droplet was consistent across all samples at 95° ±4°. To test the functionality of these materials, the minimum angle at which a 30 μL droplet of

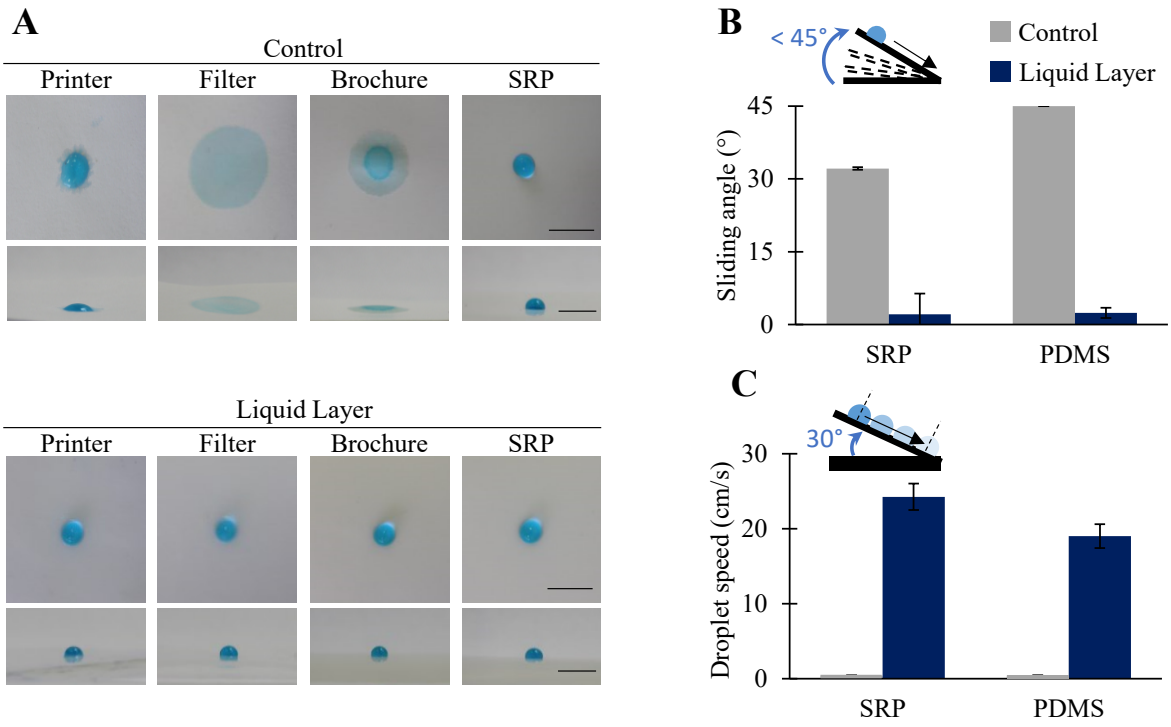

Figure 2.1. A) Images of different paper substrates types with a 50 µL droplet of dyed water to show the substrate-liquid interaction before (above) and after (below) coating and infusion. SRP indicates commercial silicone release paper. Scale bars are 10 mm in length. B) Angle at which a water droplet would slide down the substrate surface for dry controls (light grey) vs samples with a liquid layer (dark blue) for both SRP and PDMS (n=5). C) Speed at which a water droplet would travel from point to t_o point t_f on either a dry control (light grey) or liquid-infused surface (dark blue) tilted at 30°.

water would slide was assessed,[36,103] along with measurements of the speed with which the droplet moved along the surface.[31,104] SRP was chosen as the focus for these experiments as it was the most simple to fabricate of the four and was expected to be the least prone to variability due to its commercial manufacture; however, similar results were also observed for the three hand-coated samples types (**Fig. A.2**). Tests were conducted using solid blocks of infused PDMS for comparison. **Figure 2.1B** shows the results of the sliding angle tests for both the infused and dry (non-infused) substrates. The droplets on the dry materials show very high sliding angles: 32.2 ±0.3° for the dry SRP and 45°, the test's maximum value, for the dry PDMS blocks. In

contrast, the infused versions of both sample types gave sliding angle values of 2.1 ±4.3° and 2.4 ±1.1° for the SRP and PDMS, respectively, demonstrating very low adhesion of the water droplet on the surface.[15] The sliding angle results were echoed in the droplet speed tests shown in **Figure 2.1C**, where the droplets moved on the dry control surfaces at a rate of 0.3 ±0.1 cm/s for SRP and 0 cm/s (no movement) for the PDMS. For the samples with a liquid layer, the rates increased to 24.1 ±1.8 cm/s for SRP and 18.8 ±1.8 cm/s. Together, these results demonstrate that functional infused polymer surfaces can be fabricated on different paper substrate types. Importantly, they further indicate that this effect can be achieved on a commercially available substrate (SRP) using a simple 30-minute infusion in silicone oil (**Fig. A.1**), building on previous work using gas-phase chemical functionalization of paper surfaces followed by addition of a liquid layer to create fluid-repellant surfaces[105] or dip-coating paper with a PDMS/silica nanoparticle solution followed by infusion.[59]

2.4. Bacterial Retention Tests

2.4.1. Materials and Methods

Sylgard 184 silicone elastomer base and curing agent were mixed in a 10:1 ratio to create 1 mm thick PDMS sheets. After 1 h of degassing, the polymer was placed in the oven at 70°C until cured. The PDMS sheets were then cut to match the size of a glass microscope slide. SRP was also prepared to match the size of a glass microscope slide. Stock solutions of *Escherichia coli* EMG2 with the protein expression plasmid pBBR-MCS5 GFP in 2 mL of miller lysogeny broth and *Staphylococcus aureus* NCTC8532) in 2 mL of tryptic soy broth were prepared in a shaker incubator (MaxQ 6000, Thermo Fisher Scientific, Pittsburgh, PA) at 37°C and 70 rpm for 18 h. The *S. aureus* stock was then dyed with SYTO 9 green fluorescent nucleic acid stain. The liquid-

infused surfaces for both PDMS and SRP (n=3) were infused in 10cSt PDMS oil overnight. Dry control surfaces for PDMS and SRP (n=3) were immersed in 95% methanol for 10 minutes before testing to aid in the removal of dust particles from the surface. Surfaces were then placed on standard glass microscope slides. A 50 μL bacterial droplet was placed onto the top of each surface and slides were tilted until the sustained movement of the droplet occurred down the entire surface length. Surfaces were imaged using an EVOS FL AUTO inverted fluorescence microscope (Life Technologies, Carlsbad, CA) using its GFP LED light cube. PDMS surfaces were imaged with the surface upright, whereas the SRP surfaces required an additional slide to sandwich the surface and were placed on the stage with the surface side towards the lens. PDMS surfaces were imaged with a user-generated scan centered at the middle of the droplet's pathway which was a 3x30 composite with the 10X objective. The SRP dry controls were imaged at three locations along the droplet's pathway with 10×, 20×, and 40× objectives. SRP surfaces with a liquid layer were imaged at three locations along the droplet's pathway with z-stacking to capture images every ~18 μm along the z-axis to capture various positions on the SRP's surface. Fluorescent images collected were analyzed with ImageJ.

2.4.2. Results and Discussion

When considering the handling of biological and environmental samples, the preservation of high levels of antigen during translation between the sample inlet and detection site is critical, as is the delivery of a precise and repeatable volume. This has historically been a problem in traditional paper-based lateral flow assays as variable amounts of the fluid volume, in some cases up to 50%,[91] can become trapped within the paper fibers during capillary flow.[86] Retention of the sample within the paper fibers can be particularly problematic for samples

which contain larger particles, such as bacteria.[95] In contrast, many prior studies on liquid-infused polymers and other liquid-infused surfaces have demonstrated the ability of these systems to permit the movement of an entire liquid droplet from one point to the other,[106,107] as

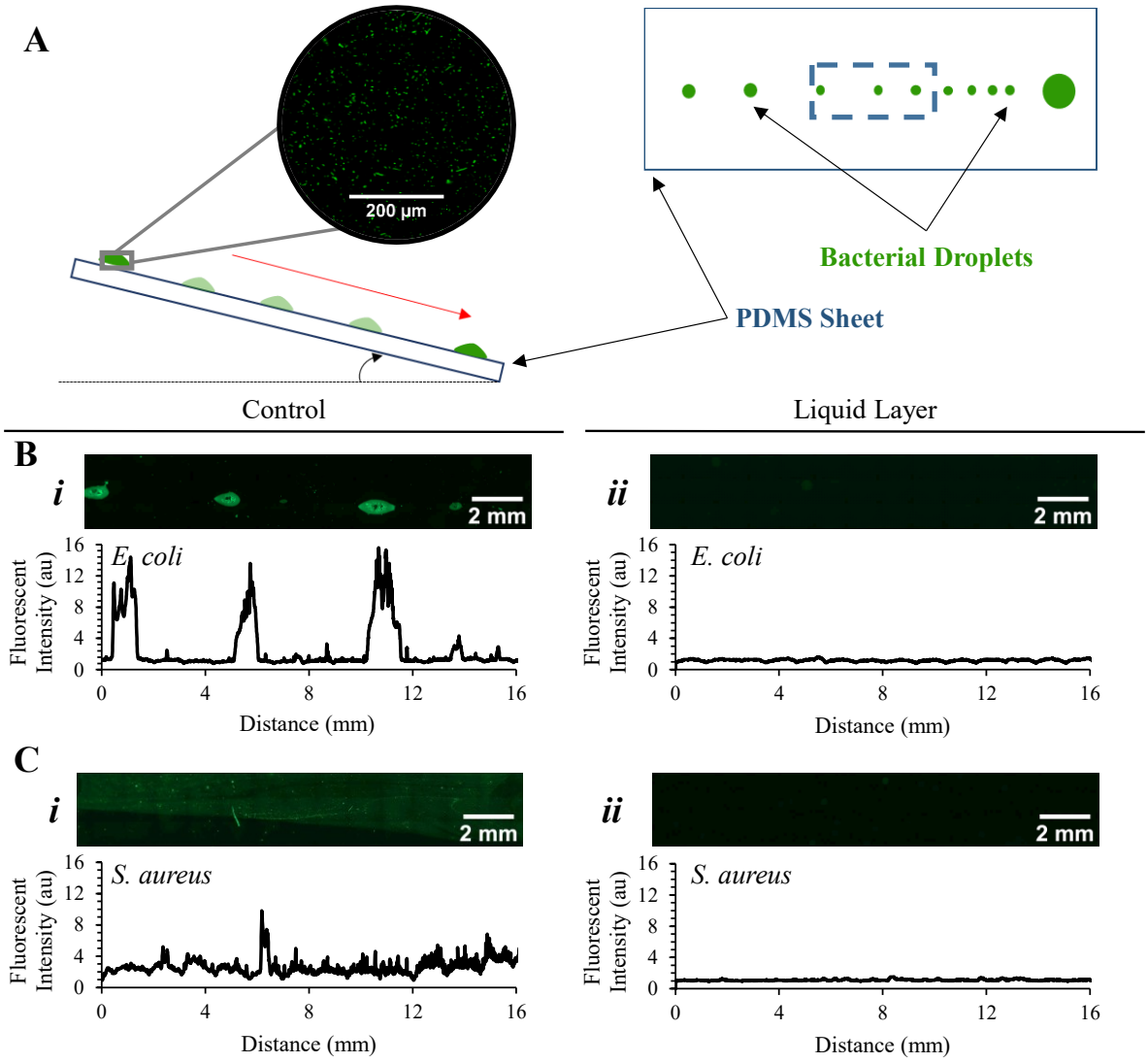

Figure 2.2. A) Schematic of the experimental setup: a droplet containing concentrated bacterial solution slides across the sample surface (left) and the path is imaged after the droplet has passed (right). B) Representative fluorescent microscopy images (top) and fluorescent intensity measurement plots (bottom) of the sample surface after passage of a droplet containing *E. coli* over dry control PDMS (*i*) and PDMS with a liquid layer (*ii*). C) Representative images (above) and intensity plots (below) after passage of a droplet containing *S. aureus* over dry control PDMS (*i*) and PDMS with a liquid layer (*ii*).

well as resist the irreversible adhesion of bacterial cells.[18,45] However, there have not yet been investigations into the ability of liquid-infused surfaces to resist adhesion of bacterial cells within a droplet moving across a surface; a point which could help mitigate the loss of large particles during sample translation in paper-based systems. To test this, we examined the liquid-infused surfaces after the passage of a 50 μL droplet of a nutrient medium densely packed with bacterial cells (10^7-10^8 CFU/mL); the results are shown in **Figure 2.2**. Two different bacterial species were used in this experiment, *E. coli* and *S. aureus*, due to their clinical and environment relevance[108–111] as well as different surface adhesion strategies.[112,113] A schematic of the experimental setup is illustrated **Figure 2.2A**. For these tests, transparent PDMS blocks are shown to avoid interference from the autofluorescence of the cellulose fibers within the paper; similar results were seen on the SRP samples (**Fig. A.3**).

Figure 2.2B*i* shows a representative image of one sample (out of 3) from the tests with a droplet containing *E. coli* moving across a dry control surface (above) and its corresponding fluorescent intensity plot (below). Scan for all of the replicates are presented in **Figure A.4**. Microdroplets containing bacteria, the result of droplet breakup, can be seen along the movement pathway in the image of the sample surface with the corresponding peaks in intensity plotted below. In **Figure 2.2B*ii***, however, there is no fluorescent signal evident on the image of the infused polymer surface after the droplet has passed, either in the image or the plot below. A representative result for the corresponding experiments with *S. aureus* across a dry control surface and liquid-infused surface are given in **Figures 2.2C*i*** and **2.2C*ii*,** respectively. Scans for all of the replicates are presented in **Figure A.5**. Upon movement across the dry surface, the droplet appears to leave behind a path of individual cells as opposed to

microdroplets that were observed for the *E.coli*-containing droplet. However, similar to the results for *E. coli* on the liquid-infused surface, no fluorescent signal is detected on the infused surface suggesting that no bacteria are left behind. These results are in agreement with multiple previous studies showing reduced adhesion of bacterial cells after exposure of liquid-infused surfaces in bulk media.[18,39,45]

2.5. Conclusion

The results presented in this chapter demonstrate the ability to fabricate paper-based liquid infused polymer surfaces for a low-cost platform. We have demonstrated how printer, brochure, and filter paper, as well as paper mass-manufactured with a silicone coating, can be used as substrates for liquid-infused surfaces. Where most of the bulk paper substrates required coating with PDMS before infusion, the commercially available SRP's existing silicone layer enabled this substrate to be infused without any surface modifications. The likeness between the infused PDMS and infused SRP's sliding angle and droplet speed measurements indicated that these were two functional liquid-infused surfaces. With the supporting information that the infused PDMS system did not retain bacterial droplets as they slide across its surface, the SRP substrate was selected to move forward with droplet manipulation experiments. The next stage of this project will leverage paper's foldability to create geometric designs to manipulate waterborne samples for applications in austere and resource-limited settings.

2.6. Acknowledgements

This chapter has been based on work previously published in *Biointerphases*, doi: 10.1116/1.5114804; authors: Daniel P. Regan, Chloe Lilly, Abigail Weigang, Liza R. White, Emily J. LeClair, Alexander Collins, and Caitlin Howell.

CHAPTER 3

LEVERAGING GEOMETRIC MANIPULATIONS OF PAPER-BASED PLATFORMS TO HANDLE WATERBORNE SAMPLES

3.1. Introduction

The 21st century has seen a rise of the biotechnology industry driven by increasingly innovative healthcare solutions. In recent years, inexpensive and robust biotech platforms that permit health assessment and treatment at the point of care or point of need have been of growing interest due to their ability to be used in rural or resource-limited environments.[2,11,12] Point-of-care (POC) technology is increasingly in demand to serve as a low-cost alternative to traditional laboratory equipment,[2,12,114,115] to monitor the spread of epidemics,[116] and to track biological threats that can arise after natural disasters.[117,118] In the design of POC systems, built-in sample handling methods which can accommodate the often complex test sample are desirable as they allow for easier use and increased accuracy of the final result.[106] This chapter will apply the paper-based liquid-infused surfaces developed in **Chapter 2** to simultaneously localize and concentrate waterborne samples.

By folding the paper into functional 3D geometries, we demonstrate how the combination of the slippery overlayer with the paper substrate can be used to precisely control the location and form of a liquid sample containing a model analyte (rhodamine) undergoing concentration via evaporation. Furthermore, we demonstrate how this principle can be applied to simultaneously concentrate and localize a solution containing bacterial cells. These results demonstrate the potential of liquid-infused surfaces on foldable paper substrates for the

handling of complex solutions, and may provide new sample handling options in the design of portable and power-free platforms for application in resource-limited settings.

3.2. Localization of Dyed Solutions

3.2.1. Materials and Methods of Geometric Manipulations to Localize Dyed Solutions

With the materials from **Chapter 2**, SRP was folded into three functional geometries: single cups, arrayed cups, and multichannel vessels. The dry controls of each geometry were left untreated, and the liquid-infused surfaces for each geometry were submerged in 10 cSt PDMS oil overnight. Upon removal, the single cups and each cup within the array were filled with 3 mL of 0.01% rhodamine 6G solution in deionized water. The multichannel vessels were filled with 90 mL of the 0.01% rhodamine 6G solution. The vessels were inserted into the oven at 50°C. An EOS Rebel T5 camera was used to image the dry control cups (n=3) at time 0 and 22.5 h, and the cups with a liquid layer (n=3) were imaged at time 0 and 138 h during evaporation. ImageJ was used to analyze the color intensity, recorded as arbitrary units (au), along the median line of the single cups for the 22.5 h images of the dry control and 138 h images of the liquid layer. Images of the dry control arrays (n=3) were taken at time 0, 3.5, and 24 h; the liquid layer arrays (n=3) were taken at time 0, 22, and 139 h throughout the evaporation process. The dry control (n=3) and liquid layer (n=3) multichannel vessels were imaged at time 0, 12, and 24 h during evaporation.

3.2.2. Results and Discussion of Localizing Dyed Solutions

Paper's ability to be folded is unlike most solid materials that have previously been used as substrates for liquid-infused surfaces. Folding paper substrates can be used to produce 3D geometries that hold liquid, resembling pockets or cups, as previously demonstrated by Glavan

and Whitesides et al.[105] Furthermore, Yang and Wong et al.[76] have recently shown that liquid-infused surfaces can concentrate biological and environmental compounds in solution. We investigated how these two concepts could be synergistically combined to yield the simultaneous concentration and localization of an analyte-containing solution in SRP cups with a liquid-infused surface. A solution of 0.01% rhodamine 6G dye in distilled water was placed in the cups and allowed to evaporate at 50°C. The sample analyte used, rhodamine 6G, provides a color contrast ideal for conducting image analysis detailing sample localization. This technique

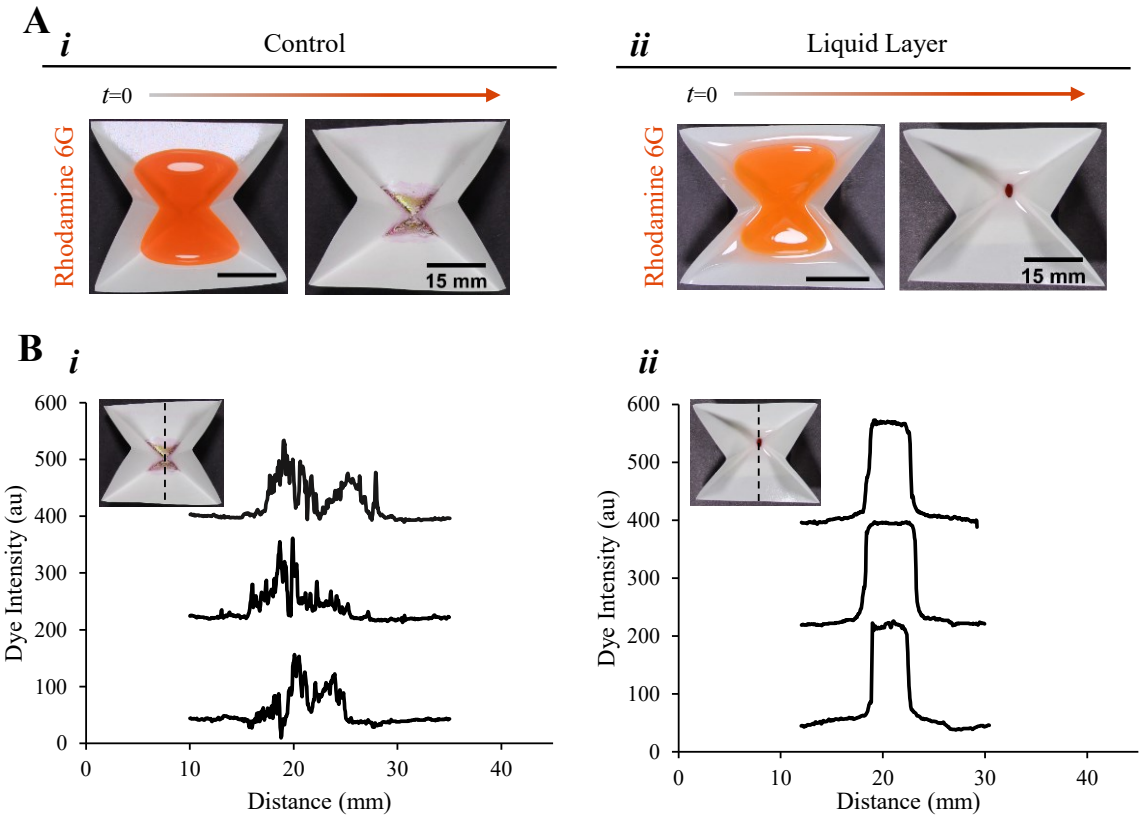

Figure 3.1. A) Images of paper with dry control surfaces (*i*) and liquid-infused surfaces (*ii*) folded into cups containing 3 mL of a rhodamine dye solution. The initial solution (left) is compared to near total evaporation (right). B) Measurements of the dye's intensity along the line of analysis of the dye remaining on the dry control surfaces (*i*) and liquid-infused surfaces (*ii*) for three independent samples after evaporation using ImageJ. Insert: image with the line of analysis indicated. Samples are offset for clarity.

enables macroscale level analysis unattainable with biological samples, however, it does not account for interactions of bacterial samples, such as adhesion, replication, and cell death. **Figure 3.1A** shows the rhodamine solution with the cups before and after evaporation. Before evaporation, each cup contained 3 mL of the rhodamine solution. In addition, cups with the liquid layer show the reflective liquid coating on both the sides of the cup and wrapped over the sample, as previously reported.[29,36,37] After evaporation, the dye is spread across the walls of the bottom third of the control cup, compared to the cups with a liquid layer which show all of the dye collected at a discrete point at the bottom. Cups with a liquid layer continued to have the sample covered with a layer of the infusing liquid, preventing the rhodamine solution from being completely dried out. **Figure 3.1B** shows the localization of the rhodamine dye as an increase in intensity relative to location. Measurements of the dry controls display several spikes in intensity across the cup diameter (9.5 ±1.3 mm), while samples with the liquid-infused surfaces show a single plateaued intensity spike of uniform width (4.4 ±0.6 mm). Further investigation of the SRP cups infused with viscosities ranging from 1.5 cSt to 10 cSt is detailed in **Appendix B**. Evaporation-assisted localization at 70°C is shown in **Figure B.1** and at ambient room-temperature is shown in **Figure B.2.**

The 3D geometry of the folded cups was designed to localize the sample into a pre-defined location (the lowest point of the cup) as evaporation acted upon the sample. In **Figure 3.1A** it is evident that the dyed sample trended towards a general localization at the bottom point in both the dry controls and the samples with the liquid layers; however, it can also be seen that more rhodamine was successfully localized in target area in samples with liquid-infused surfaces. Previous work has indicated that the presence of an immiscible surface liquid

layer enables evaporation of a droplet with a nearly constant contact angle.[34] This effect can be leveraged to concentrate very dilute solutions on a flat surface due to the fact that particles contained within the droplet do not become trapped at the contact line.[76] The liquid layer shifts the flow of molecules within the solution during evaporation from the surface to the top of the solution rather than outward toward the contact line, preventing the coffee ring effect.[119,120] A lack of contact line pinning and associated particle buildup appears to be occurring on the liquid-infused surfaces presented here, helping to guide the majority of the rhodamine dye particles to precisely

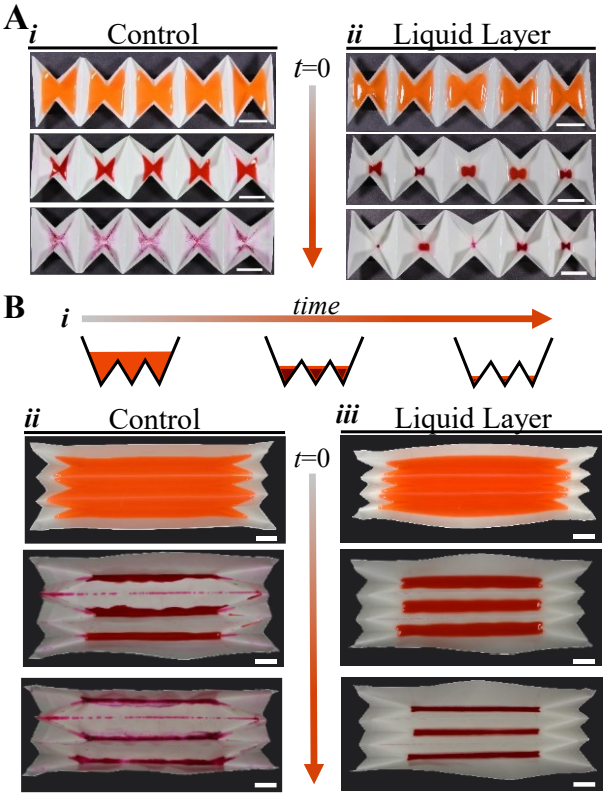

Figure 3.2. a) Images of an array of cups at before (top), during (mid), and after (bottom) evaporation of a rhodamine dye solution for samples made with dry control surfaces (*i*) and liquid-infused surfaces (*ii*). B) Schematic outlining the functioning of a sample geometries designed to separate one contiguous volume of liquid into three separate concentrated volumes (*i*) followed by images of the geometries made with either dry control surfaces (*ii*) or liquid-infused surfaces (*iii*). Scale bars in (A) and (B) are 20 mm in length.

localize at the predetermined points within the folded paper cups. In addition, the presence of a wrapping layer over the samples on liquid-infused surfaces prevented the rhodamine sample from evaporating completely: these samples were still liquid after ~138 h compared to controls which dried completely after only ~23 h at 50°C. This observation may prove useful in applications where having the sample remain in a liquid state is desirable for further processing

and analysis. In addition, the rate of sample evaporation could likely be tuned by changing the volatility of the infusing liquid.[45]

Figure 3.2 shows the concept of geometry-defined sample localization expanded into an array format. In **Figure 3.2A**, images of an array of five cups filled with the rhodamine dye solution are shown before, during, and after evaporation at 50°C are presented. The effect is the same as in the single cup shown in **Figure 3.1**: the dry controls have dye remaining along the walls of the cups (**Fig. 3.2A*i*)** while the cups with a liquid layer show all the dye collected at defined points (**Fig. 3.2A*ii*)**. **Figure 3.2B*i*** shows an array geometry which separates one large sample volume into three separate concentrated volumes via evaporation. Images of the dry control (**Fig. 3.2B*ii*)** and liquid layer ([**Fig. 3.2B*iii*)** samples are presented before, during (~12 h), and after evaporation (~24 h). After 12 h, both the control and liquid layer samples have transitioned from one contiguous sample volume into three separate sample volumes within the channels. It can be seen that the samples on dry control surfaces have a non-uniform contact line between the sample and the walls at 12 h. After 24 h, the control has approached total evaporation and the rhodamine dye is non-uniformly adsorbed along the lower edges of the channel walls. In contrast, the samples with the liquid layer showed highly uniform behavior throughout evaporation, and even lines of concentrated sample after 24 h. In both cases, some rhodamine dye was present at the ridges in between the channels, suggesting that where the paper was folded outwards the integrity of the silicone coating was compromised and rhodamine to seep through to the paper layer underneath. This effect was much more pronounced in the dry control samples, however, as the silicone coating liquid in the liquid-infused samples likely saturated the paper and prevented the dye from adhering.

3.3. Concentration of Bacterial Samples

3.3.1. Materials and Methods

The single cup geometry from Section 3.2.1 was used to contain bacterial solutions during evaporation. For the liquid layer condition, 36 cups were submerged in 10 cSt PDMS oil overnight, and 36 cups were left unaltered to serve as the dry control. Stock solutions of *E. coli* and *S. aureus* were prepared in 2 mL of Miller LB incubated at 37°C for 18 h, and 2 mL of TSB incubated at 37°C for 9 h, respectively. Stock solutions were serially diluted into 0.1X PBS to reach a colony forming unit (CFU) count of 10^5 CFU/mL. Dilute PBS was used to yield a final concentration of 1.0X when the sample reached minimum volume (10X). A 3 mL volume of this solution was added into each of the cups, which were placed in an incubator set at 40°C and loaded with trays of magnesium sulfate to aid the evaporation process. Three stages of analysis were established as independent ranges of volumetric concentration within the cups, corresponding to a roughly three-fold (1mL), five-fold (0.6mL), and ten-fold (0.3mL) changes in volume, reached after 5.5 (±0.25), 7.5 (±0.25), and 10.3 (±0.7) h, respectively. The final volumes of each cup were removed with a syringe and the volume recorded. All experimental conditions were performed with an n=6 except for the liquid layer samples containing *S. aureus*, which had an n=5. Post-evaporation CFU counts were conducted by spreading 100 μL of a diluted sample onto LB growth plates for *E. coli* and TSB growth plates for *S. aureus*; a control plate of the 0.1X PBS was also prepared for CFU analysis. All CFU plates were counted after 24 h of incubation. A paired two-tailed t-test (Microsoft Excel) was used to determine statistical significance. A confidence interval of 95% was used with assumptions of a continuous dependent variable,

independent observations, normal distribution of the dependent variable, and absence of outliers were made.

3.3.2. Results and Discussion

One of the limitations of many paper-based detection platforms is a lack in sensitivity,[8,11,121,122] which can present challenges in applications where the concentrations of analytes may be relatively low. To address this, samples can be concentrated on-site via methods such as centrifugation[8,11,123] or filtration[10,85] for biomolecules, or a growth-based enrichment step for microorganisms.[8,122] However, these processes often require additional equipment or resources. Alternative methods which can achieve the result of concentration without the need for additional materials could therefore prove valuable in the expansion of paper-based technology. Tests were conducted to determine whether the simultaneous concentration and localization effects observed in **Figures 3.1** and **3.2** could be applied to clinically-relevant samples. For these experiments, we chose bacteria as targets due to their importance in both medicine and the environment, as well as their active surface adhesion tendencies: bacteria are well-known to seek out and irreversibly attach to surfaces in the first step of biofilm formation.[112,124]

Figure 3.3 presents the effect of the concentration of bacterial cells in solution via evaporation in dry control versus liquid-infused cups. As shown in the schematic in **Figure 3.3(a)**, as evaporation progresses, it is expected that bacterial cells in the dry control surfaces will stick to the sides of the cup, while samples in the liquid layer surfaces will slide into the bottom of the cup, similar to what was seen in **Figures 3.1** and **3.2** with the rhodamine dye. **Figure 3.3B** shows the number of gram-negative *E. coli* cells present in the cups as the liquid

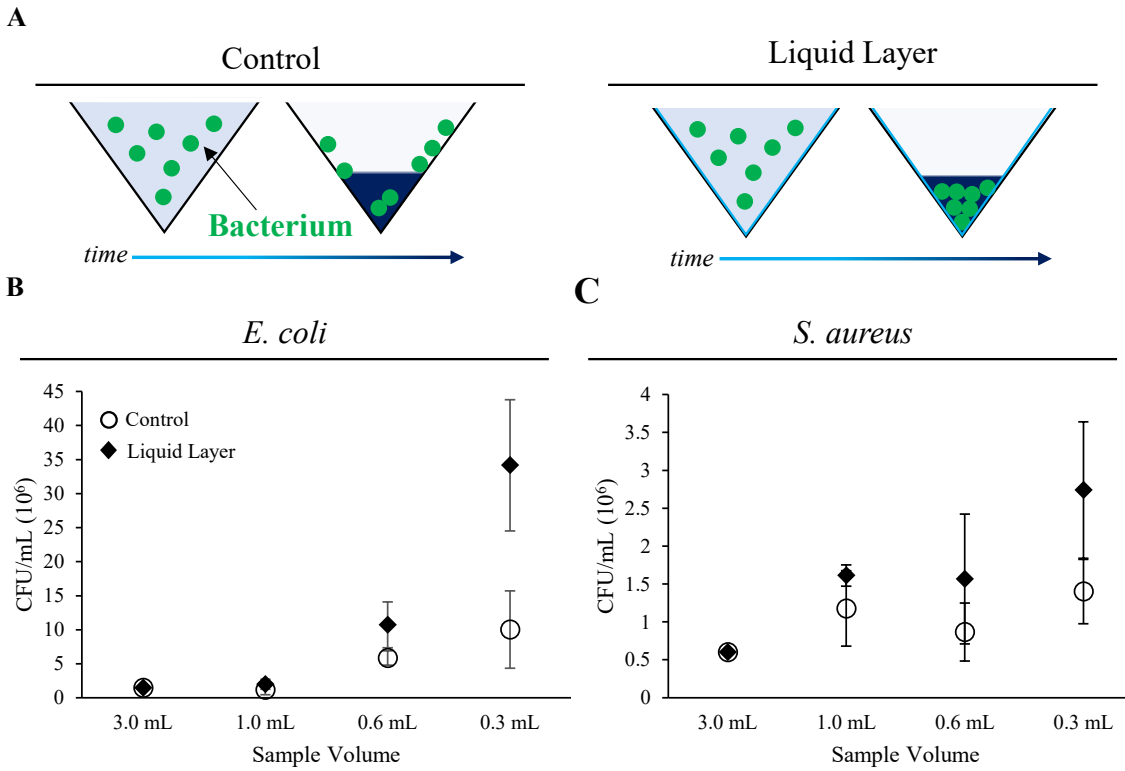

Figure 3.3. A) Schematic of the evaporation process on bacteria-containing liquid sample in cups made with dry control surfaces (left) and liquid-infused surfaces (right). B) The number of colony-forming units per mL in liquid containing *E. coli* taken before evaporation (3.0 mL liquid volume) as well as at three points during evaporation (1.0, 0.6, and 0.3 mL liquid volumes). Counts are shown for samples with dry control surfaces (open circles) as well as with liquid-infused surfaces (filled diamonds). C) Results from a similar experiment with a *S. aureus*-containing liquid.

volume decreases due to evaporation. Samples were initially loaded with 3 mL of a 0.1X PBS solution containing 1.5×10^6 CFU/mL. After ~5.5 h of evaporation at 40°C, the liquid volume in the cups had reached approximately 1 mL (a 3X concentration). At this point, both the dry controls and the samples with the liquid layer had relatively similar CFU values (1.2×10^6 $\pm7.5\times10^5$ and 2.0×10^6 $\pm6.4\times10^6$, respectively). After ~7.5 h, analysis conducted via a paired two-sample t-test revealed that difference had widened to a significantly different 5.9×10^6 $\pm1.1\times10^6$ CFU/mL in the dry control cups and 1.1×10^7 $\pm3.4\times10^6$ CFU/mL in the cups with the liquid layers

(P=0.008). Finally, after ~10.5 h, the control samples showed 1.0×10^7 $\pm5.4\times10^6$ compared to 3.4×10^7 $\pm9.6\times10^6$ CFU/mL for the samples with the liquid layers (P=0.004).

In comparison, **Figure 3.3C** shows the data collected in a similar experiment conducted with the gram-positive *S. aureus*. The initial 3 mL of 0.1X PBS solution contained 6.0×10^5 CFU/mL. After ~5.5 h at 40°C, the volume within the cups had reached 1 mL in which bacterial concentrations measured 1.2×10^6 $\pm5.0\times10^5$ and 1.6×10^6 $\pm1.4\times10^5$ CFU/mL for dry control and liquid layer samples, respectively. After ~7.5 h there was a minimal change in concentration, with the dry control at 8.7×10^5 $\pm3.8\times10^5$ CFU/mL and the liquid layer at 1.6×10^6 $\pm8.6\times10^5$ CFU/mL. The final observation was conducted after ~10 h where the dry control showed 1.4×10^6 $\pm4.2\times10^5$ CFU/mL and the sample on a liquid layer 2.7×10^6 $\pm9.0\times10^5$ CFU/mL (P=0.06).

The results shown in **Figure 3.3** support the hypothesis that the presence of a liquid layer contributes to a higher concentration of bacterial cells in a solution concentrated by evaporation than dry controls for *E. coli*. However, the total number of cells in the solution at the last two analysis times also suggest that these bacteria were growing during the evaporation process: at the final time point, the volume was concentrated 10 times (3 mL to 0.3 mL). If the starting concentration of bacterial cells was concentrated 10 times, the result would have been 1.4×10^7 CFU/mL; however, the measured value for the samples with the liquid layer was almost 2.5 times that value (3.4×10^7 CFU/mL), indicating growth. This increase observed in the *E. coli* data set should not be anticipated for all waterborne samples, as several confounding variables may have contributed to the 2.5-fold concentration above expectation. Additional experiments would be required to explore the factors contributing to the growth of the bacteria during the concentration process. One potential factor was the presence of a small amount of medium

present in the starting concentration which itself became concentrated as evaporation progressed, as well as the established non-toxicity of the silicone oil in the samples with liquid surfaces.[36] Often, collections of waterborne samples do not meet the thresholds required for detection via point-of-care or culture-based analysis.[125,126] Increasing the number of bacteria within a sample by providing them with growth media, known as an enrichment step, is a commonly used method to improve the detection limit of bacterial tests.[109] The observation that this can be done in conjunction with evaporative concentration may prove useful in engineering bacterial sample preparation platforms. It should be noted, however, that proper dilution of the sample is critical prior to evaporation, as simultaneous concentration of salts and other materials along with the bacterial cells could have an adverse effect on the latter's ability to grow. Over-concentration could lead to high levels of salts in the solution and subsequent bacterial dehydration, resulting in cellular death. The most extreme concentration in this study finished with bacteria in 0.3 mL of ~1.0X PBS solution, providing an environment that avoided dehydration and osmotic stress on the bacterial cells.

The results for *S. aureus* are less clear. Each point of analysis showed that solutions in cups with a liquid layer were more concentrated than the corresponding dry control samples. However, none of these differences were statistically significant, including for the most concenterated sample (P=0.06). The difference in results between *E. coli* and *S. aureus* may be due to environmental sensitivity: *S. aureus* begins to experience temperature-related death near 43 °C,[127] compared to *E. coli* near 47 °C.[128] Although set at 40 °C, the incubators likely experienced some fluctuations in temperature which may have contributed to the observed results. However, the lack of a difference as large as those seen for *E. coli* between dry controls

and cups with liquid layers suggest that *S. aureus* is likely interacting with the liquid layer in a different way. This observation agrees with previous results that have shown differences in how different species[18] or even different strains of bacteria interact with liquid layers.[129] Nevertheless, the results indicate that liquid-infused polymers on paper can be used to concentrate bacteria in solution.

3.4. Summary and Conclusions

The results presented in this work show how paper substrates can be combined with liquid-infused surfaces to form functional platforms for the simultaneous localization and concentration of rhodamine dye solutions as well as media containing *E. coli* and *S. aureus* cells. When the paper substrates with liquid-infused surfaces were folded into cups, they could be used to simultaneously concentrate and localize a solution of rhodamine dye into target points at the bottom of the cups much more efficiently than samples without a liquid coating. This approach could be expanded into an array format with multiple cups, as well as to a multi-channel vessel which intrinsically separated a single large sample volume into three discrete lines of concentrated solution. Simultaneous concentration and localization was also investigated for solutions containing *E. coli* and *S. aureus*. Significantly more *E. coli* cells were observed in the samples with liquid-infused surfaces compared to dry controls. An increase in the number of *S. aureus* cells was also observed for samples with liquid-infused coatings, although this number did not rise to the level of significance. These findings demonstrate how liquid-infused polymers can be used as a functional surface coating in conjunction with defined sample geometry to achieve synergistic effects, and may prove useful in the development of integrated sample handling systems for POC platforms.

3.5. Acknowledgements

The author thanks Dr. Phil Kim and Prof. Dr. Michael Grunze for helpful discussions as well as Prof. Andre Khalil for his guidance during the image analysis portion of the work. This chapter has been based on work previously published in *Biointerphases*, doi: 10.1116/1.5114804; authors: Daniel P. Regan, Chloe Lilly, Abigail Weigang, Liza R. White, Emily J. LeClair, Alexander Collins, and Caitlin Howell.

CHAPTER 4

SYSTEM DESIGN AND EVALUATION OF BIOAEROSOL GENERATION AND FILTRATION FOR AIRBORNE SAMPLE HANDLING

4.1. Background

As the world hurries to take back control over SARS-CoV-2, the viral pathogen causing the COVID-19 pandemic, scientific efforts behind countermeasures and pathogen identification have gained increased attention.[130] From both a public health and national security standpoint, it is critical to have a functioning biosurveillance infrastructure to monitor the presence and spread of biological threats.[116,131] Knowledge of the pathogens that are transmitted via the aerosol route is limited,[132–134] and this knowledge is compounded as the pathogens that make up bioaerosols will likely change as climate patterns shift.[135] Furthermore, such strategies are needed in space where the immune system, microbial growth,[136] and bioaerosol dynamics[137] are much different than on Earth. The collection and identification of airborne pathogens is important not only for monitoring potential exposure, but to conduct bioinformatic analysis to track mutations and shifts in the genomics and proteomics of the pathogen.[132] In addition to tracking changes within a known pathogen, biosurveillance is need for monitoring high risk environments. Travel hubs and modes of mass transportation are of particular concern due to the risk of human-to-human transmission, as well as spreading the disease to a new region.[131,138,139] Biosurveillance measures are also needed to monitor the presence and spread of pathogens that cause hospital-acquired infections, for both patients and health care workers.[134,140–143] While much of the focus is on the identification of transmissible pathogens,

airborne bacteria also account for a range of health issues from allegories, asthma, autoimmune disorders, and have been linked to mental health.[143]

To conduct surveillance of bioaerosols, scientists turn to a variety of air samplers. Two factors which influence the type of sampler used are the environment in which the sampler is deployed and the desired analysis.[144,145] Liquid impingers are often turned to when maintaining viability is desired; however, these platforms can face issues of sample loss, re-aerosolization, and low capture efficiency.[146,147] While filter-based sampling offers the best range of particle size capture, factors such as desiccation and impaction can reduce the viability of captured pathogens.[145,147,148] One modification to filter-based sampling to increase pathogen viability and transfer is to use gelatin filters, but the lack of temperature stability limited the operational parameters to short-duration use, even in moderate temperatures.[149]

Liquid net (LN) filtration aims to improve the performance of filter-based air samplers by providing a catch-and-release mechanism. To get the benefits of liquid impingers while maintaining the versatility of filters, a liquid layer is added to the filter substrate. Previously, liquids have been added to filtration membranes to produce liquid-gated membranes,[19,150] in which the infusing liquid is selected to have chemical affinity to the filter.[16] In turn, the infusing liquid forms a "gate" which can be deformed and reformed as a the threshold transmembrane pressure is first surpassed and then falls back below that threshold pressure, respectively.[150] Most studies using the liquid gate approach have used commercial polytetrafluoroethylene (PTFE) filters and infused with a PFPE oil;[19,150–152] although others have used elastomers,[153] polyvinylidene fluoride (PVDF) membranes,[154–156] functionalized polyethylene terephthalate (PET),[157] and electrochemical surface modifications to stainless steel.[158] These systems have

primary been studied as a filter for multiphase separations,[150,153,158] separating emulsions,[157] preventing fouling of inorganic matter,[152,158] increasing flux recovery against organic foulants,[19] and improving the durability of filters for water treatment.[158]

In this chapter, the concept of a liquid net filtration, in which liquid coats the filter fibers and is used to capture and release airborne pathogens is established. Presented in this chapter are three aerosol generation and filtration systems used to evaluate the performance of the liquid nets. The first system used a bubbler flask to generate aerosolized *E. coli* but was not selected due to its variance in droplet generation over time. The second aerosolization and filtration design used a syringe nebulizer in which the aerosol generated did not exit the aerosol chamber. The third and final design implemented ultrasonic diffuser, which provided an acceptable method of aerosol generation. The successful pilot run results with the ultrasonic diffuser system led to this design being used to analyze the performance of liquid nets for all subsequent chapters.

4.2. Bubbler Flask Design

4.2.1. Fabrication

The first filtration system assembled, depicted in **Figure 4.1**, was modified from the system designed to assess flux recovery in liquid-gated membranes.[19] A 500 mL filtration flask (Pyrex) was sealed with a rubber stopper modified with a section of high-density polyethene tubing (1/8″ inner diameter, ¼″ outer diameter) that extended into the base of the flask. This component served as the source flask, designed to generate aerosols as the PV-35 vacuum pump (Precision Scientific Co.) pulled air through the polyethylene tubing into the bacterial solution within the flask, causing bubbling and aerosol generation. Once aerosols were

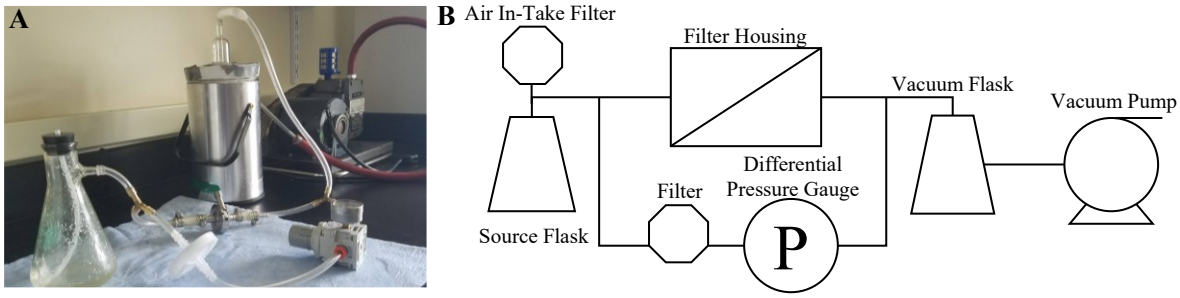

Figure 4.1. A) Image of the first aerosolization system, the bubbler flask design. B) Process flow diagram of the bubbler flask design.

generated, the negative pressure pulled the air through a parallel split, in which one line contained a QF-16 stainless steel filter housing (Kurt J. Lesker Co.) in which held the filters, and the other parallel line was set with a pressure gauge (SMC) to observe transmembrane pressure. If any aerosol bypassed the filters, they were collected in a 500 mL vacuum trap and dewar flask (Chemglass Life Sciences) before damaging the vacuum pump.

4.2.2. Materials and Methods

Stock solutions of *E. coli* EMG2 with the protein expression plasmid pBBR-MCS5 GFP in 2 mL of LB Miller containing 5 μg/mL gentamicin sulfate were prepared in a shaker incubator at 37 °C and 100 rpm for 20 h. From the stock solution, 1 mL of stock was diluted into 9 mL of 1× PBS. The bacterial solution within the source flask was comprised of 1 mL of the diluted *E. coli* stock and 400 mL of 1× PBS, for a final concentration of ~8.3×10^5 cells/mL.

Unlaminated 1.0 μm PTFE filters were purchased from Sterlitech Corp and were cut to the size of the housing for a diameter of 17 mm, a cross sectional area of ~2.3 cm^2. The low viscosity (82 cSt) Krytox 103 or high viscosity (1535 cSt) Krytox 107 PFPE oils (DuPont) was pipetted on top to infuse the filters. Both a low (90 μL) and high (180 μL) infusing volumes were tested as these were determined to be the near minimum and near maximum infusion limits.

For the filtration tests, pre-cut filters, either infused or dry control, were loaded into the filter housing. The source flask was disconnected from the system while the vacuum pump ran for a three-minute primer to deform the PFPE liquid and open any blocked pores. The flask was immediately reconnected, and the system was run for another three minutes as aerosols were generated. One set of PTFE filters had a recovery period of 15 minutes, while another set of filters had a 30-minute recovery period. These isolation periods were based on flux recovery data previously observed in liquid-gated membranes, where a 15% and 60% recovery of initial membrane flux was achieved after a 15- and 30-minute recovery periods, respectively.[19] Once the isolation times were completed, the filters were physically impressed onto LB agar plates three times. Plates were incubated at 37 °C for 24 hours before CFU counts were recorded.

4.2.3. Testing and Conclusions

Evaluation of the control PTFE and PTFE-Liquid Nets (PTFE-LNs) was conducted by normalizing the CFU totals of two data sets, for a total of 9 independent filters (n=9) per infusion and isolation condition. Details on the original CFU counts and normalized data for these sets are provided in **Appendix** C. Normalization for each filter was conducted by dividing the total CFUs transferred and dividing it by the starting concentration of the *E. coli* solution within the source flask. Since multiple runs with different starting concentrations were used, normalization was needed for comparable results. Those averages and standard deviations were then multiplied by 10^5 to bring values greater than 1.0 for easier visual analysis. The results of this analysis are presented in **Figure 4.2**, in which the grey bars are the averages of the PTFE and PTFE-LNs that underwent a 15-minute recovery, and the navy bars are the corresponding filters which experienced a 30-minute recovery. The lowest counts for each

recovery period were the control PTFE filters, in which the normalized values for the 15-minute recovery period were 6.53 ±8.75 CFU/membrane, and the 30-minute 1.79 ±1.88 CFU/membrane. Similarly, the highest CFU counts were both the PTFE-LNs infused with 90 μL of Krytox 107: the 15-minute recovery yielded 70.3 ±60.3 CFU/membrane, while the 30-minute recovery gave 64.6 ±47.0 CFU/membrane.

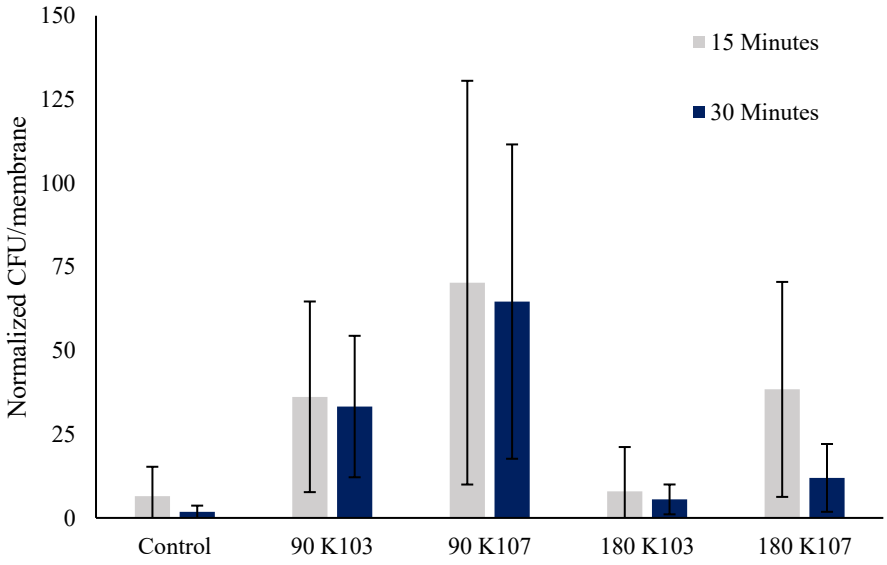

Figure 4.2. Normalized CFU counts generated from control PTFE and each infusion condition of the PTFE-LNs from the bubbler flask design. Grey bars plotted represent the average and standard deviation for filters that underwent a 15-minute recovery, while navy bars correspond to the 30-minute recovery data.

The large standard deviation within each experimental condition is a result of the inherent variability within the aerosolization system. The source flask is serving as a batch system depleted by 3-minute aerosol periods per filter. Due to the aerosol generation occurring at the base of the solution volume, total exposure varied from the first filter of the run to the final filter. This inherent variability within the system accounted for too many confounding

factors. While the bubbler system provided preliminary testing for filter fabrication and liquid net viability, improvements needed to be made to generate a viable data set.

4.3. Syringe Nebulizer Design

4.3.1. Fabrication

After assessment of the previous system's failures, improvements to aerosol delivery were prioritized. Inspiration for the second aerosolization system came from syringe nebulizers often used to administer intranasal medication. For this new system, shown in **Figure 4.3**, a compressed air line was installed connected to a flowmeter (Dwyer Instruments) to control the flowrate. The outgoing airline was connected to the first port on a four-way stop cock. The middle port of the stop cock served as the Leur taper connection for a 3 mL syringe containing

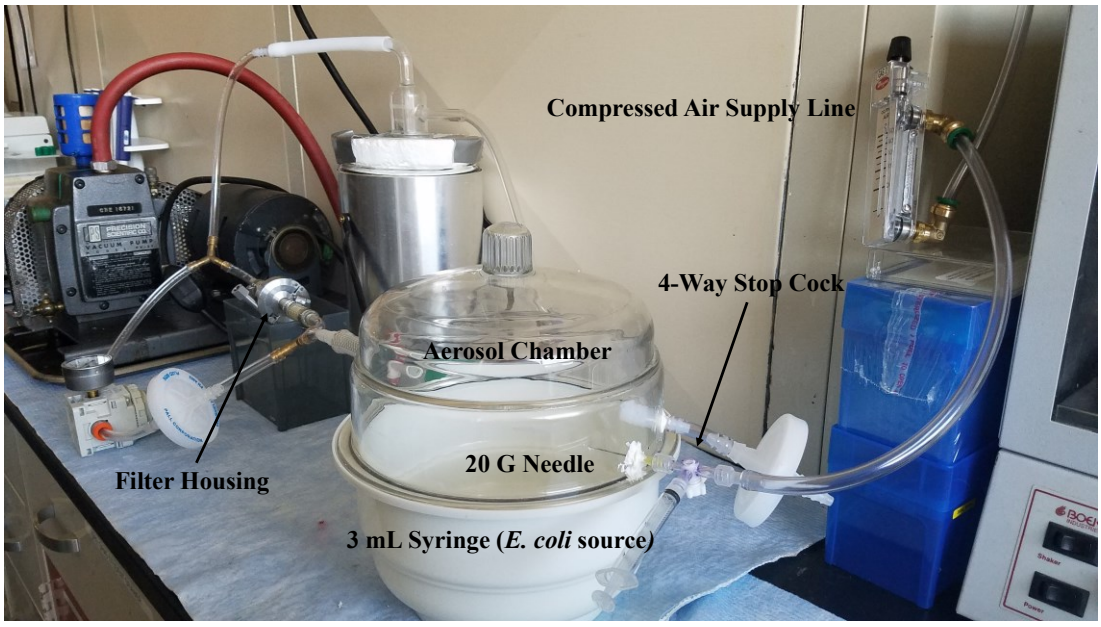

Figure 4.3. Image of the second aerosolization system, the syringe nebulizer design. The compressed air supply (top right) forced the *E. coli* solution from the 3 mL syringe (bottom center) through the 20-gauge needle to form an aerosol stream. That stream was enclosed within the aerosol chamber as the vacuum pump pulled the stream towards the filter housing, (left center) in which the system remained the same from the previous design.

the *E. coli* solution, and the final port was fixed with a 20-gauge needle that was inserted and sealed into an aerosol chamber. An air inlet port was drilled and capped with a 0.2 μm air filter (Pall Corporation) to maintain a sterile flow of air through the chamber. The aerosol chamber, a modified 19.7 cm diameter vacuum desiccator (Bel-Art), replaced the source flask (seen in **Fig. 4.1**) from the previous bubbler flask system.

4.3.2. Materials and Methods

Stock solutions of *E. coli* were cultured following the protocol listed in **Section 4.2.2.** From the stock solutions and 1× PBS, two serial dilutions were performed. Unlaminated 1.0 μm PTFE filters were cut and infused, again following the procedure in **Section 4.2.2.** Two data sets were generated following this protocol, where each of the following filter conditions had a sample size of n=3: dry control, 90 μL K103, and 90 μL K107. The first data set used *E. coli* at a concentration of 1.74×10^{7} CFU/mL, while the second data set used 1.74×10^{6} CFU/mL.

To test filtration, a PTFE filter was loaded into the filter housing. The vacuum pump ran for a three-minute primer to deform the PFPE liquid and open any blocked pores. Following the three-minute primer the flowmeter was opened to 450 cc/min and the 3 mL of *E. coli* solution was injected into the system. Once all 3 mL were aerosolized, the flowmeter was returned to 0 cc/min and the vacuum remained on for a one-minute dwell time to clear any remaining aerosol. The PTFE filters were isolated for 15 minutes before stamping onto LB agar plates three times. Plates were incubated at 37 °C for 24 hours before CFU counts were recorded.

4.3.3. Testing and Conclusions

Several iterations of the syringe nebulizer system were tested before the protocol from **Section 4.3.2.** was implemented for the best chance at success. In this approach, multiple data

sets were collected, using high concentration of *E. coli*, and a high flowrate to generate a fine aerosol mist. However, the results from the best-case scenario again resulted in unacceptably large variation (see complete data set in **Appendix D**). The mode of CFUs transferred and counted was 0 for all but the PTFE-LNs infused with Krytox 107 and exposed to 1.74×10^7 CFU/mL, in which the total counts for the three LNs were 0, 1, and 2 CFUs. The main limitation in this system was considered to be the size of the aerosol chamber. After the completion of each data the aerosolized *E. coli* solution that was retained formed a pool of liquid at the base of the aerosol chamber. The dispersion pattern and velocity of the aerosol mist were too great compared to the size of the chamber and resulted in ~70-90% of the sample impacting the walls of the chamber. The design of the next system needed to generate an aerosol mist that could be suspended within the aerosol chamber but pulled through the system's tubing to be filtered by the control PTFE and PTFE-LNs.

4.4. Ultrasonic Diffuser Design

4.4.1. Fabrication

To resolve issues related to the generation of the aerosol, the syringe nebulizer was swapped out for an ultrasonic diffuser. The ultrasonic diffuser (InnoGear) operates as a batch system, capable of holding 100 mL of bacterial solution. Similar ultrasonic diffusers have shown their devices generate aerosols with an average diameter of 3.4 μm.[159] The diffuser was placed in the aerosol chamber, as depicted in **Figure 4.4**. All modifications to the chamber were sealed with silicone caulking. Again, negative pressure was pulled across the filters placed in a QF-16 stainless steel housing and obtained using a PV-35 vacuum pump. Transmembrane pressure was observed using a pressure gauge, preceded by a Vacushield filter (Pall Corporation) to

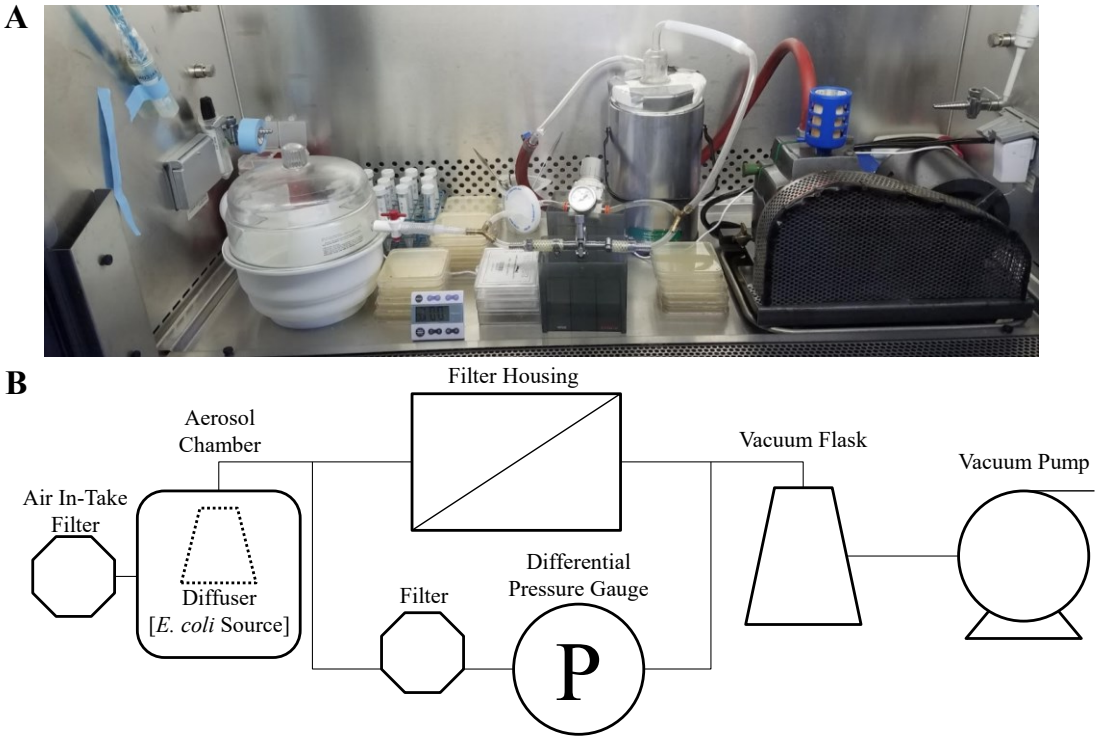

Figure 4.4. Image of the ultrasonic diffuser aerosolization system within a biological safety cabinet (A) and its process flow diagram (B).

prevent contamination within the line. Bypassed aerosol droplets were collected in a vacuum trap and dewar flask. All experiments conducted using the ultrasonic diffuser were performed with the system placed within a biological safety cabinet.

4.4.2. Aerosolization and Filtration Materials and Methods

Stock solutions of *E.coli* were cultured following the protocol from **Section 4.2.2.** Serial dilutions of the stock were conducted into 1× PBS and adjusted to an optical density at 600 nm (GENESYS 10S UV-Vis, Thermo Fisher Scientific) of 0.004A relative to the 1× PBS blank, bringing the starting concentration between 10^5–10^6 CFU/mL. A volume of 80 mL was placed into the ultrasonic diffuser. Dry control filters and LNs were randomized for their run order in the filtration. Once the filter was placed in the housing, a one-minute cycle with only the vacuum powered on, to deform the liquid around the pores, was run. Immediately following

that phase was the six-minute aerosolization stage in which the ultrasonic diffuser and vacuum were both running. Once six minutes was reached, the diffuser was turned off while the vacuum remained on for one minute to clear the aerosol chamber. Then, the filter was removed from the housing and placed into a conical tube for a set recovery phase. After the recovery phase the filters were physically impressed onto LB Miller agar plates (containing 5 μg/mL gentamicin sulfate) applying pressure by sweeping curved forceps over the entire filter. Each filter was impressed nine consecutive times. Plates were then incubated at 37 °C for 24 h before conducting CFU counts.

4.5. Conclusions

In this chapter, several aerosol generation and filtration systems were designed to test the performance of liquid nets, a filter with liquid-coated fibers used to capture and release airborne pathogens. The first system tested was the bubbler flask design. The variation in droplet generation over time required modifications to the aerosol generation mechanism. The second system accounted for this by using a syringe nebulizer and an aerosol chamber. However, this system experienced high aerosol retention with the chamber, preventing the aerosol to reach the filter housing. The third and final system was replaced the syringe nebulizer with an ultrasonic diffuser. This system generated a consistent aerosol mist that filtered through the system aerosol chamber and to the filter housing, as expected. The positive results of the ultrasonic diffuser system meant that a standard mechanism for evaluation of liquid nets was established. Using the ultrasonic diffuser system, the next step was to investigate how altering parameters like the pore size and infusing properties affected the performance of PTFE-LNs.

4.6. Acknowledgements

Parts of this chapter are being prepared for peer-review publication and have been incorporated into a patent application.

CHAPTER 5

OPTIMIZATION OF PTFE FILTERS FOR LIQUID NET FILTRATION

5.1. Introduction

In the previous chapter, the concept of liquid net filtration was introduced and the aerosolization system needed to test LN filtration was established. As mentioned in **Section 4.1.3**, the engineering behind liquid nets is rooted in the field of liquid-infused surfaces (LIS). While previous studies have used LIS principles to create liquid-gated membranes for applications like phase separations and wastewater treatment, no group has applied such materials for bioaerosol filtration. Here, PTFE filters and PFPE lubricant oil are used to investigate the optimal parameters for LN filtration by evaluating the transfer of captured aerosolized *E. coli* via bacterial culture analysis. Filters were physically impressed onto agar plates to transfer and grow the captured *E.* coli from each dry control filter and LN run through the system. While gross CFU counts are used to evaluate the total capture-and-release performance of the filters and PTFE-LNs, a new metric, the bioaerosol rate of release value, is introduced to analyze filter performance. This normalized metric, or R-value, provides insight as to the retention of the total captured load over each physical removal step. The properties of LNs should result in improved rate of release, as shown by lower R-values, over those of the dry control filters as the infused PFPE oil is expected to separate from the surface along with any associated pathogens. Specifically, this improvement should manifest in the results as lower R-values earlier in the stamping cycle and staying near or at zero once it is approached.

This chapter set out to establish the optimal configuration and parameters for LN filtration using PTFE filters and PFPE infusing oil. Previous studies using liquid-gated

membranes showed that a longer recovery phase and a higher viscosity yielded greater membrane flux recovery compared to shorter recovery phases and lower viscosities.[19] Therefore, the effects of PFPE viscosity, PFPE infusing volume, recovery time, and pore size were evaluated with PTFE membranes. The first optimization tests were conducted using PTFE filters with a 1.0 μm pore size. PTFE-LNs were fabricated using both low (82 cSt) and high viscosity (1535 cSt) PFPE Krytox oils. For each viscosity, a low volume, or near minimum volume required for homogenous infusion, and a high volume, the near maximum amount of oil applied before over-saturation, of the PFPE oil was used and infusion density (volume of PFPE oil over the cross-sectional area) was calculated. These filters were then run through the filtration cycle and tested over three different recovery phases: 0-, 15-, and 30-minutes. Based on the information from the 1.0 μm tests, 10 μm liquid nets were then tested for their optimal configuration. The final study aimed to understand the effects of temperature over a 24-hour recovery phase. The effect of temperature over an elongated period was performed to understand the potential shelf-life between filtration and pathogen release for laboratory and remote settings. The results presented in this chapter demonstrate the ability of liquid nets to capture and release aerosolized *E. coli* at significantly lower R-values than bare PTFE filters, providing a new application of liquid-infused surface in liquid net filtration.

5.2. Materials and Methods

All filters were cut to the size of the housing for a diameter of 17 mm/cross sectional area of ~2.27 cm^2. Unlaminated 1.0 and 10 μm PTFE filters were purchased from Sterlitech Corp. The low viscosity, 82 cSt, Krytox 103 (K103) and high viscosity, 1535 cSt, Krytox 107 (K107) PFPE oils (DuPont) was pipetted on top to infuse filters. For the 1.0 μm pore size filters, the low volume,

80 μL, and high volume, 160 μL, infusing values were prepared as detailed in **Table 5.1**. The volume/area dose of 13.6 ±1.1 μL/cm^2 aligned with the reported 13 μL/cm^2 of K103 on 5.0 μm PTFE filters.[152] These infusion volumes were halved for the 10 μm pore size filters, as the 10 μm filters are nearly half as thick, at 130 μm, compared to the 1.0 μm filters (203-305 μm).

Table 5.1. List of PTFE-LNs with Corresponding Infusing Liquid Properties

Filter Type	Volume (μL)	Krytox Oil	Viscosity (cSt)	Volume/Area (μL/cm^2)
1.0 μm PTFE	80	103	82	13.6 ±1.1
1.0 μm PTFE	80	107	1535	20.1 ±3.2
1.0 μm PTFE	160	103	82	15.3 ±1.8
1.0 μm PTFE	160	107	1538	33.1 ±3.5
10 μm PTFE	40	103	82	7.5 ±1.2
10 μm PTFE	40	107	1535	16.3 ±2.1
10 μm PTFE	80	103	82	8.8 ±0.5
10 μm PTFE	80	107	1538	27.4 ±2.8

5.2.1. Surface Characterization

Bare PTFE filters (n=3) were used to conduct contact angle measurements. A 10 μL water droplet (200 μL FD&C Blue #1 dye in 50 mL of water) was placed onto each of the bare filter surfaces. Each independent filter was tested in three locations. Images were taken with an EOS 5D Mark II camera (Canon) and measured using the low-bond axisymmetric drop shape analysis ImageJ plug-in.[102] Sliding angle measurements were collected on all bare control filters and the Liquid Nets listed in **Table 5.1**. Three independent filters were tested (n=3) with five replicates per filter. Samples were set at 0° on an adjustable angle stage with a digital angle gauge (AccuMASTER, Calculated Industries). A 25 μL water droplet (200 μL of FD&C Yellow #5 and FD&C Blue #1 dye in 50 μL of water) was pipetted onto the filter surface, then the stage was manually tilted until sustained droplet movement was observed and the gauge's angle reading was recorded. Scanning electron microscopy (SEM) images were capture on an AMRay

1820 set to 10 kV. Prior to imaging, dry control filters were mounted with adhesive carbon tapes on aluminum stubes. The samples were then sputter coated (Cressington) with gold-palladium until the coating was 4 nm thick.

5.2.2. 1.0 µm Pore Size Recovery

Three independent experiments were conducted to investigate the effects of the recovery phase on 1.0 µm PTFE filters. A sample size of n=3 was used for each experiment, including three bare control PTFE filters and three of each 1.0 µm PTFE filter listed in **Table 5.1**. The filtration protocol previously detailed in **Section 4.4.2** was used for each of the three experiments, in which recovery phases of 0-, 15-, and 30-minutes were used for each new experiment, respectively. The run order of the filters was randomized (see **Appendix E for order**). Statistical analysis of the rate of release R-values (**Section 5.2.5**) for PTFE-LNs was conducted in R-Studio by a 3×2×2 ANOVA, Tukey's Honest Significant Difference (HSD) post hoc tests, in which interactions within and/or between the recovery phase, volume, and viscosity were investigated. Analysis between the control PTFE filters and the PTFE-LNs was conducted via Welch two-sample t-tests. For samples not meeting the assumption of normality then the Mann-Whitney Non-Parametric Analysis was performed. If the PTFE-LN with the lowest R-value did not have a P-Value ≤ 0.05, then no more comparisons were performed for that stamp number.

5.2.3. 10 µm Pore Size Recovery

Two independent experiments were conducted to investigate the effects of the recovery phase on 10 µm PTFE filters. A sample size of n=3 was used for each experiment, including three bare control PTFE filters and three of each 10 µm PTFE filter listed in **Table 5.1**. The

filtration protocol previously detailed in **Section 4.4.2** was followed with one amendment, in which the filtration system and loaded diffuser were run for a 15-minute build-up phase before running the first filter. This change was implemented after preliminary tests where CFUs were not transferred for the first 3–5 filters, and then a steady increase in CFUs growth continued thereafter. The first experiment set the recovery phase to 15 minutes, while the second experiment was set to 30 minutes. The run order of the filters was randomized, available in **Appendix F**. Statistical analysis of the PTFE-LNs across every recovery experiment was conducted by a 2×2×2 ANOVA and Tukey's HSD post hoc tests within R-Studio. Following the protocol described in **Section 5.2.2**, the rate of release data for stamps 2-4 were investigated for statistical significance.

5.2.4. Temperature-Based Recovery

Twenty-seven 1.0 μm PTFE filters were prepared to investigate a 24-hour recovery at three different temperatures: 4 °C, 26 °C, and 40 °C. Bare control filters, low volume K103, and high volume K103 PTFE-LNs were tested at each temperature range with sample size of n=3. The filtration protocol described in **Section 4.4.2** was followed; however, the volume loaded into the ultrasonic diffuser was increased from 80 mL to 90 mL, with an additional 50 mL added after the 15th filter was cycled. An alternating run order was followed as detailed in **Appendix G**. Statistical analysis was conducted via two-factor ANOVAs in R-Studio, with Tukey's HSD post hoc tests, in which interactions within and between the recovery temperature and infusion volume were investigated in relation to the total CFUs transferred, and then the rate of release R-values. Again, significant interactions between the dry controls and the PTFE-LNs were conducted following the steps in **Section 5.2.2**.

A

	Stamp 1	Stamp 2	Stamp 3	Stamp 4	Stamp 5	Stamp 6	Stamp 7	Stamp 8	Stamp 9
Theoretical 1	100	100	100	100	100	100	100	100	100
Theoretical 2	100	90	80	70	60	50	40	30	20
Theoretical 3	200	100	50	25	12	6	3	1	0
Theoretical 4	125	25	5	1	0	0	0	0	0

B

	Stamp 1	Stamp 2	Stamp 3	Stamp 4	Stamp 5	Stamp 6	Stamp 7	Stamp 8	Stamp 9
Theoretical 1	1.00	1.00	1.00	1.00	1.00	1.00	1.00	1.00	1.00
Theoretical 2	1.00	0.90	0.80	0.70	0.60	0.50	0.40	0.30	0.20
Theoretical 3	1.00	0.50	0.25	0.13	0.06	0.03	0.02	0.01	0.00
Theoretical 4	1.00	0.25	0.05	0.01	0.00	0.00	0.00	0.00	0.00

C

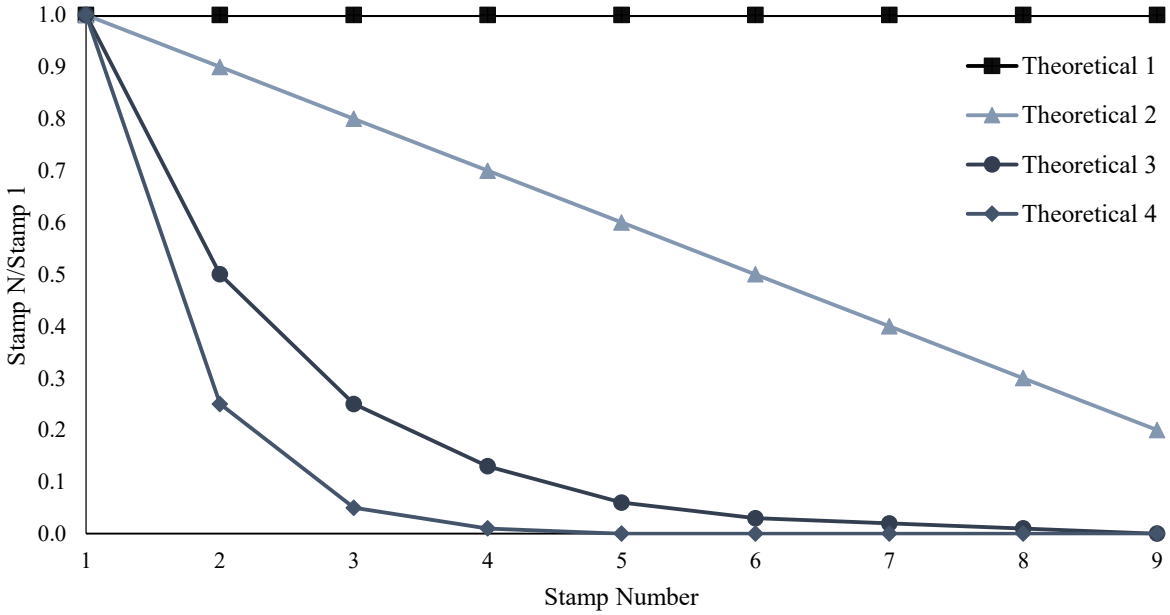

Figure 5.1. A) Table of transferred CFUs for each stamp of four theoretical filters. B) Table of the calculated Rate of Release values for the each of the four theoretical filters. C) Graph of theoretical Rate of Release values. Theoretical 1, black boxes, maintained a value of 1 for every stamp (R=1). Theoretical 2, light blue triangles, decreased by 0.1 ($R_S=R_{S-1}-10$) each stamp. Theoretical 3, blue circles, was halved every stamp ($R_S=R_{S-1}/2$). Theoretical 4, grey blue diamonds, decreased by a factor of 5 ($R_S=R_{S-1}/5$) until it reached zero at stamp number 5.

5.2.5. Rate of Release Calculation

The main analysis used to evaluate the performance of the dry controls and LNs was the trend in each filters Rate of Release. The Rate of Release (R_S) was calculated as the amount of

CFUs (C_s) transferred during each stamp over the amount of CFUs transferred during the initial stamp (C_i):

$$R_S = C_S/C_i$$

This value was computed on each stamp for every filter tested, thereby normalizing each filter's first stamp to a value of 1. Thus, the fewer stamps a filter takes to approach and maintain an R-value near 0, the better the filter is at releasing its captured bioaerosol load as demonstrated in **Figure 5.1**. This becomes increasingly important for pathogens that exist in low concentration among the physical ratio of bioaerosol particulates. These pathogens are prone to be misrepresented in cultural analysis when if the total capture-load is not transferred from the filter. Therefore, it is important to account for a filter's rate of release when determining their performance for air sampling.

5.3. Results and Discussion

5.3.1. Surface Characterization

To understand the surface topography of the dry control PTFE filters, SEM images were collected. The 1.0 μm pore size PTFE filters exhibited a microrough surface, as seen in **Figure 5.2A**. Contact angle measurements were conducted on the 1.0 μm PTFE filters to further investigate the bare filter's surface properties (**Fig. 5.2B**). The bare PTFE filters (n=3) exhibited a contact angle of 133 ±3°. These results reaffirm the fact that PTFE is a hydrophobic material. The low standard deviation indicates the relative homogeneity of hydrophobicity across the surface of the bare PTFE filters. The final characteristic experiment conducted on the 1.0 μm PTFE filters was the sliding angle analysis (**Fig. 5.2C**). These measurements were conducted with a 25 μL water droplet to understand the compatibility and wetting between the PTFE substrate and

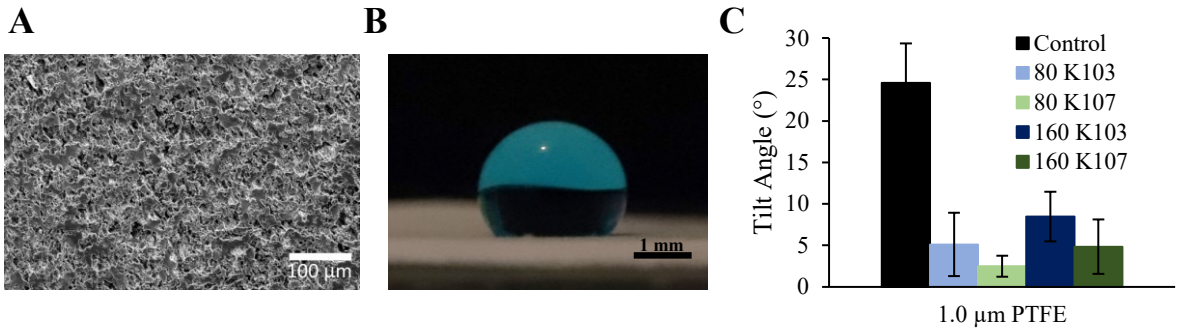

Figure 5.2. A) SEM image at 200× magnification of 1.0 µm PTFE filter's surface. B) Representative image of PTFE's contact angle. C) Sliding angle measurements graphed for the bare PTFE control (black) and each 1.0 µm PTFE-LN: 80 µL K103 (light blue), 80 µL K107 (light green), 160 µL K103 (navy blue), and 160 µL K107 (dark green).

PFPE infusing liquid. For the bare PTFE filter, the sliding angle was relatively high at 24.6 ± 4.8°. For PTFE filters infused with the low viscosity K103, the sliding angle measurements yielded values of 5.1 ±3.8° (infused with 80 µL) and 8.5 ±3.0° (infused with 160 µL). Similarly, filters infused with the high viscosity K107 were recorded at 2.5 ±1.3° (infused with 80 µL) and 4.8 ±3.3° (infused with 160 µL). The decrease in tilt angle by infusing the bare PTFE filter with the PFPE lubricant is consistent with previous studies on liquid-infused surfaces.[16,106,160] The sliding angle metric is indicative of the liquid layer's interaction with the material surface. Low sliding angles indicate a stable liquid layer in which the droplet can freely flow across the liquid's surface, whereas higher sliding angles are most likely due to strong interactions with the filter's surface, causing droplet pinning. These surface property results support the claim that PTFE filters infused with PFPE oil form liquid-infused surfaces and should perform similarly to the liquid-gated membranes previously published.[152]

5.3.2. 1.0 µm Pore Size

The first recovery phase investigated using the 1.0 µm PTFE filters was the 0-minute recovery to establish a baseline performance. For the 0-minute recovery experiment, filters were

immediately stamped onto the agar plates once the one-minute purge phase of the aerosol chamber was completed. After the 24-hour incubation period, the transferred CFUs were counted for each stamp for analysis. The starting concentration of the *E. coli*-PBS solution loaded into the ultrasonic diffuser was 1.05×10^{6} CFU/mL. Results from the Rate of Release calculations are displayed in **Figure 5. 3**, in which the R-value (y-axis) is plotted as a function of the stamp number (x-axis). Analysis from the Tukey HSD's post hoc test investigating the relationship between the recovery time and infusion volume revealed a significant difference existed (P=0.05) between the 80 µL and 160 µL volumes for the third stamp. These PTFE filters infused with 80 µL of K103 and K107 had R-values of 0.043 ±0.047 and 0.046 ±0.034, respectively; whereas the PTFE filters infused with 160 µL of K103 and K107 had R-values of

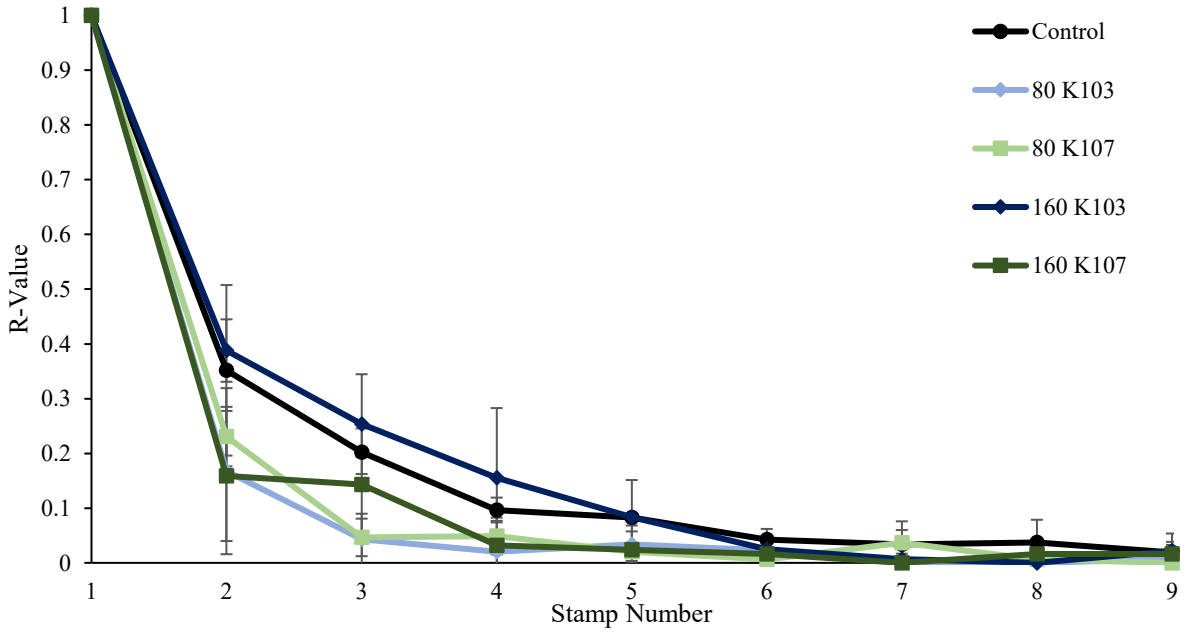

Figure 5.3. Rate of release analysis for 1.0 µm PTFE control and PTFE-LNs that underwent a 0-minute recovery phase. Plotted are the average and standard deviation values for the dry PTFE control as black circles, and the PTFE-LNs: 80 µL K103 plotted with light blue diamonds, 80 µL K107 with light green squares, 160 µL K103 navy blue diamonds, and 160 µL K107 as dark green squares.

0.253 ±0.091 and 0.143 ±0.103. Further analysis of the R-values at stamp number three found that the control PTFE filters (0.202 ±0.009) were significantly different from the 80 μL K103 PTFE-LN's rate of release (P=0.04) and the 160 K107 PTFE-LN's rate of release (P=0.03) via Welch two sample t-tests. Analysis conducted on the CFU counts for the first stamp and total CFU transfer resulted in statistical significance between the control filter and the 80 μL K103, 80 μL K107, and 160 μL K107 PTFE-LNs with P-values of 0.04, 0.009, and 0.006 respectively for total CFUs transferred (**Table E.3**). Compared to analysis of just the CFUs transferred during the first stamp (**Table E.4**), significant differences existed between the bare control and PTFE-LNs infused with 80 μL K107, 160 μL K103, and 160 μL K107 with P-values of 0.04, 0.05, and 0.02, respectively.

The results from the 0-minute recovery data highlight how the evaluation of bare PTFE and PTFE-LNs must be rooted in a multifaceted approach. When looking at just the raw colony forming unit counts, the amount of captured pathogen transferred and cultured, the control PTFE filters outperformed all four LNs. For both the first stamp and total transfer analysis, the control PTFE filters transferred a significantly higher amount of *E. coli* colonies than 75% of the LNs. By this analysis, the bare filters would be preferred to capture-and-transfer to yield the highest number of pathogens in the environment after a 0-minute recovery phase. However, this analysis is blind to the transfer efficiency of these filters. That is where the rate of release analysis comes into play. As demonstrated by **Figure 5.3**, it is the LNs that are outperforming the control PTFE filters, with exception to the 160 μL K103 PTFE-LNs. Focusing on the low-volume low-viscosity (80 μL K103) Liquid Net which had a significantly better rate of release at the third stamp when compared to the bare control, it is worth noting how quick this filter

approached a rate of release near zero. These results suggest that LN filtration is preferential to the control filtration when releasing the total capture pathogenic load in as few steps as possible is required. This analytical method is important when considering pathogens of interest, or biological threats, that are expected to be in relative low concentration within the total bioaerosol composition.

The second recovery phase explored used the 15-minute isolation period. This experiment was independent of the 0-minute recovery phase but was conducted and performed in the same manner. Loaded into the ultrasonic diffuser was a starting concentration of 4.80×10^5 CFU/mL. The 15-minute recovery phase data set resulted in several differences compared to the

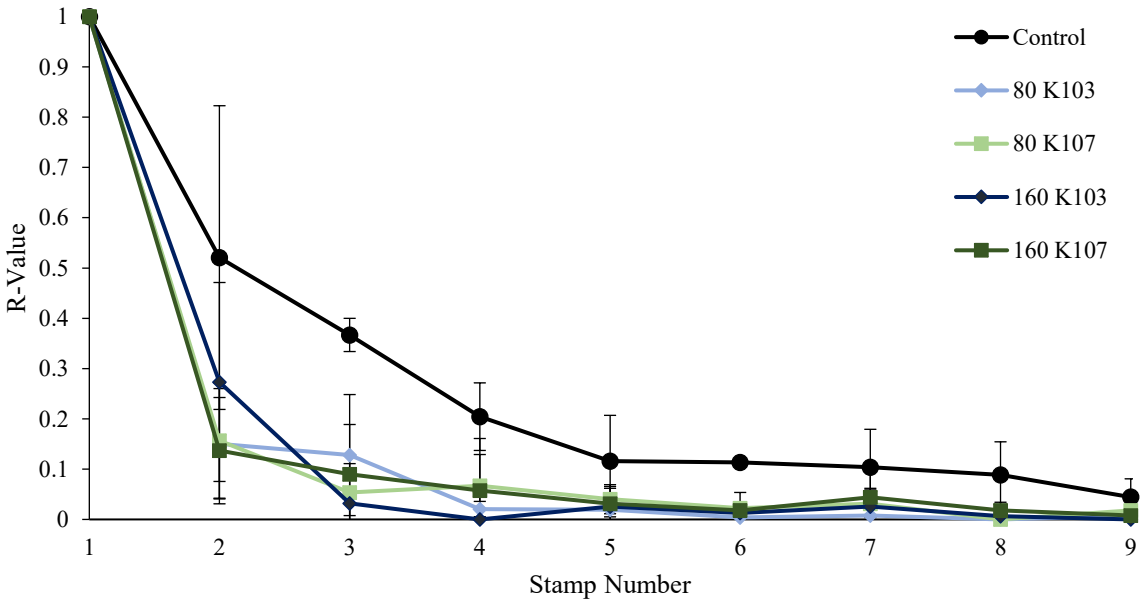

Figure 5.4. Rate of release analysis for 1.0 μm PTFE control and PTFE-LNs that underwent a 15-minute recovery phase. Plotted are the average and standard deviation values for the dry PTFE control as black circles, and the PTFE-LNs: 80 μL K103 plotted with light blue diamonds, 80 μL K107 with light green squares, 160 μL K103 navy blue diamonds, and 160 μL K107 as dark green squares.

0-minute recovery baseline. The rate of release results are shown in **Figure 5.4.** For this data set, the ANOVA found no significant differences between any of the PTFE-LN configurations as was previously found between the infusion viscosities with the 0-minute recovery data. Furthermore, investigation into the control PTFE and PTFE-LNs transfer totals for both the cumulative count (**Table E.7**) and first stamp (**Table E.8**) found no interactions of statistical significance. However, Welch two sample t-tests revealed significant differences with the rate of release values at the third stamp between the control PTFE R-value, 0.37 ±0.03, and the high-volume low-viscosity PTFE-LN, 0.03 ± 0.03 (P=0.0005), as well as both high viscosity PTFE-LNs: low-volume 0.05 ±0.06 (P=0.006) and high-volume 0.09 ±0.10 (P=0.001). This continued for the fourth stamp between the bare control and high-volume low-viscosity (160 μL K103) PTFE-LN, with a P-value of 0.05, and the low-volume low-viscosity (80 μL K103) PTFE-LN nearly achieving statistical significance (P=0.055).

Results from the 15-minute recovery set indicate the potential benefits of some recovery period between the end of filtration and transferring captured pathogens for culture analysis. Unlike to the 0-minute baseline, the control PTFE filters did not significantly release more *E. coli* colonies in either the first stamp or cumulative metrics in comparison to any of the PTFE-LNs. Moving to the rate of release analysis (**Fig. 5.4**), multiple PTFE-LNs outperformed the control at the third and fourth stamps. It is worth drawing attention to the high-volume low-viscosity (160 μL K103) PTFE-LN's rate of release numbers. This PTFE-LN configuration had higher R-values than the control for stamps 2-4 during in the baseline data set; now for the 15-minute recovery data, this PTFE-LN maintained lower R-values than the control throughout all stamps and

achieved statistical difference in stamps 3 and 4. These results suggest the need for a 15-minute recovery phase before stamping filters for pathogen transfer.

Completing the recovery phase analysis of the 1.0 μm PTFE filters was the 30-minute recovery data set. The starting concentration for this independent set of filtrations was 6.90×10^5 CFU/mL. Again, the addition of time between filtration and stamping, in this case 30-minutes, eliminated the statistical difference between the CFUs transferred in total (**Table E.11**) and during the first stamp (**Table E.12**) between the dry controls and the PTFE-LNs that was seen in the 0-minute baseline. Rate of release values for the bare PTFE controls and PTFE-LNs are displayed in **Figure 5.5**. However, unlike the 15-minute recovery data set, the best-performing (PTFE-LN with the lowest R-value) did not achieve statistical significance compared to the

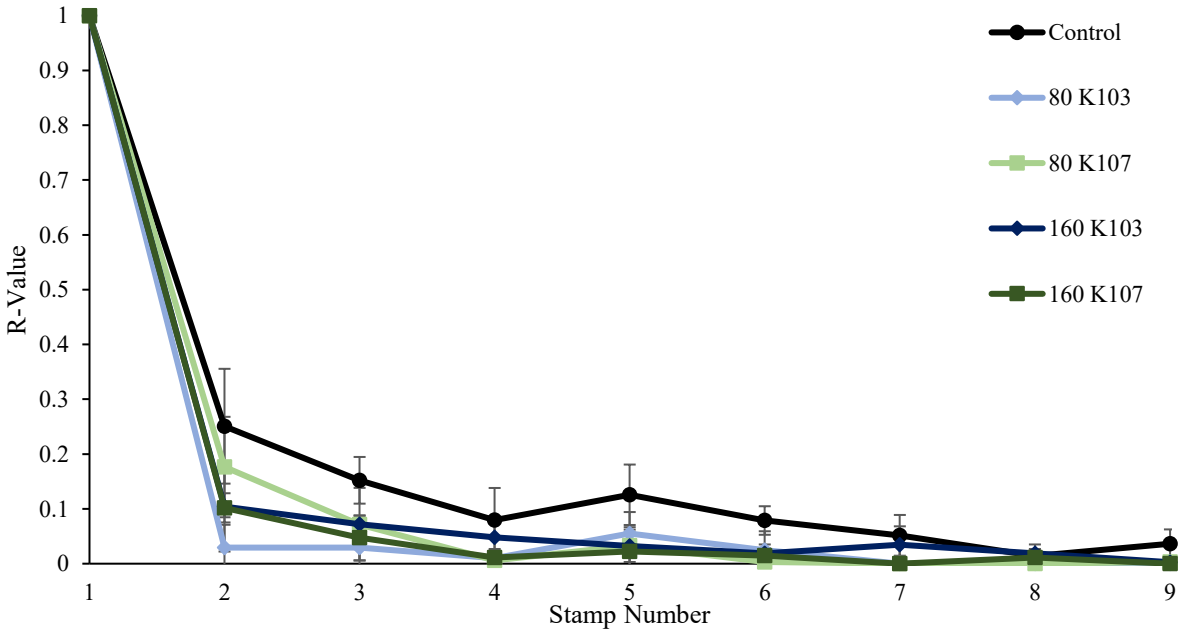

Figure 5.5. Rate of release analysis for 1.0 μm PTFE control and PTFE-LNs that underwent a 30-minute recovery phase. Plotted are the average and standard deviation values for the bare PTFE control as black circles, and the PTFE-LNs: 80 μL Krytox 103 plotted with light blue diamonds, 80 μL Krytox 107 with light green squares, 160 μL Krytox 103 navy blue diamonds, and 160 μL Krytox 107 as dark green squares.

control. In every case, stamps 2-4, the best performing PTFE-LN was the low-volume low-viscosity (80 μL K103) configuration, the P-values in order were 0.077, 0.077, and 0.354. Since the ANOVA and Tukey HSD analysis indicated no significant difference between the PTFE-LN configurations within the 30-minute recovery data set, no further tests were conducted.

While the final data set from the 1.0 μm time-based recovery experiments did not contain any significant interactions within its own data, there was one point of statistical significance involving this data set. The Tukey HSD post hoc test investigating the interactions of the recovery time between the three data sets during the second stamp yielded a P-value of 0.05 between the 0- and 30-minute recovery data sets. This statistical significance is a result of the overall lower R-values at the second stamp after a 30-minute recovery (**Fig. 5.5**) as compared to the 0-minute baseline (**Fig 5.2**). Again, as seen for the 15-minute recovery, rate of release results (**Fig. 5.4**) for all PTFE-LNs were lower than those of the bare control.

The improvements to PTFE-LN performance in the 15- and 30-minute as compared to the 0-minute baseline are reminiscent of the improvements to flux recovery reported after a recovery period with PTFE liquid-gated membranes, in which the liquid re-equilibriates.[19] The improvements to the rate of release values between the 0- and 30-minute recovery sets at the second stamp, and P-value of 0.0005 between the R-values of 160 μL K103 PTFE-LN and control at the third stamp for the 15-minute recovery are strong indicators that a recovery phase is necessary for Liquid Nets to efficiently transfer their pathogens for culture analysis. Previous work with silicone-based liquid-infused surfaces demonstrated the risk of entrapping microdroplets of *E. coli* due to embedding and formation of the wrapping layer over the pathogens.[161] These results may account for the lower CFU transfer totals in comparison to the

bare PTFE controls, as well as why the recovery phase improves the rate of release for the PTFE-LNs.

5.3.3. 10 µm Pore Size

Testing on an increased pore size, 10 µm, was performed to explore a potential option in which less material (both PTFE an PFPE) are required, potentially providing a more economic LN configuration. The first data set collected with the 10 µm PTFE filters had a recovery phase of 15-minutes. Due to the increased pore size and decreased filter thickness, the infusing volumes were changed to continue using the near minimum and maximum infusing volumes. For the 10 µm PTFE filters, these volumes were 40 and 80 µL, with their respective infusing densities (µl/cm^2) listed in **Table 5.1**. A starting concentration of 6.50×10^5 CFU/mL was loaded

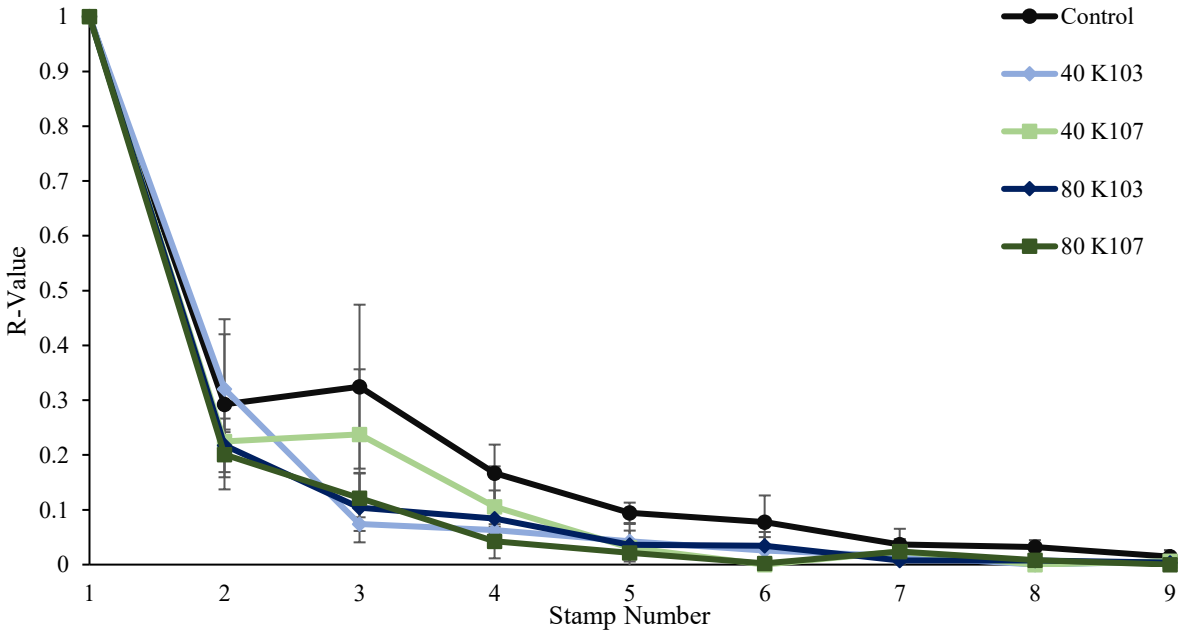

Figure 5.6. Rate of release analysis for 10 µm PTFE control and PTFE-LNs that underwent a 15-minute recovery phase. Plotted are the average and standard deviation values for the dry PTFE control as black circles, and the PTFE-LNs: 40 µL Krytox 103 plotted with light blue diamonds, 40 µL Krytox 107 with light green squares, 80 µL Krytox 103 navy blue diamonds, and 80 µL Krytox 107 as dark green squares.

into the ultrasonic diffuser. Statistical analysis conducted on the total CFUs transferred (**Table F.3**) and focused in on the first stamp (**Table F.4**) resulted in no significant differences between the controls and Liquid Nets. Furthermore, investigation of the rate of release data, **Figure 5.6**, between the best performing PTFE-LNs (lowest R-value) and control filters for stamps 2–4 all returned P-values > 0.05, indicating no significant difference. While there were no instances of statistical significance within the 15-minute recovery phase data, it worth noting that the general trend of the PTFE-LNs having lower R-values compared to the bare control PTFE filters continued, with exception to the 40 μL K103 PTFE-LNs in the second stamp, for this data set.

The direct follow-up to the 15-minute recovery data was the 30-minute recovery investigation of the 10 μm PTFE filters. For this independent experiment, a starting concentration of 9.90×10^5 CFU/mL was used. As previously reported for the 15-minute recovery data, no significant difference was detected between the bare control filters and the PTFE-LNs for both the total CFU transfer (**Table F.7**) and the first stamp CFU counts (**Table F.8**). However, that is where the similarity in results between the two recovery phases ends. Several key significant interactions exist within the data from the rate of release calculations displayed in **Figure 5.7**. In the comparison of the PTFE-LNs to the bare control filters, statistical significance was found at the third stamp. The control PTFE filters had an R-value of 0.318 ±0.044, whereas the high viscosity PTFE-LNs registered R-values of 0.141 ±0.0034 (40 μL K107) and 0.063 ±0.022 (80 μL K107); the corresponding P-values between the control filters and the high-viscosity PTFE-LNs were 0.01 and 0.006, by order of increasing volume. As previously noticed with the 1.0 μm PTFE-LNs, a delayed recovery time increased the performance of the LNs rate of release. While stamps two and four did not yield significant differences, several significant interactions

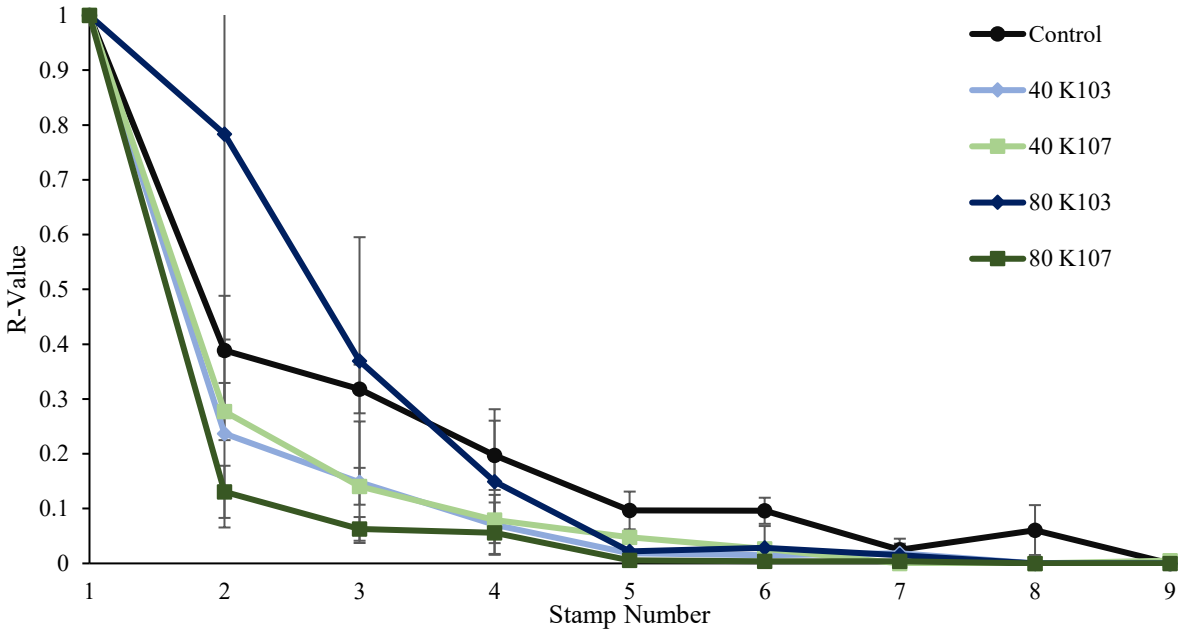

Figure 5.7. Rate of release analysis for 10 μm PTFE control and PTFE-LNs that underwent a 30-minute recovery phase. Plotted are the average and standard deviation values for the bare PTFE control as black circles, and the PTFE-LNs: 40 μL Krytox 103 plotted with light blue diamonds, 40 μL Krytox 107 with light green squares, 80 μL Krytox 103 navy blue diamonds, and 80 μL Krytox 107 as dark green squares.

within the PTFE-LN rate of release data were noted from the ANOVA and ensuing Tukey HSD analysis. Specific to the 30-minute recovery, the 80 μL K107 PTFE-LNs outperformed the 80 μL K103 PTFE-LNs during the second stamp registering a P-value of 0.04. During the analysis of the second stamp's rate of release data, significant interactions within the Viscosity, and the Viscosity and Volume interaction were found. For viscosity alone, the K107 and K103 had a P-value of 0.04. Additionally, the viscosity~volume analysis resulted in a P-value of 0.05 between the 80 μL K107 and 80 μL K103 PTFE-LNs. The final significant interaction at the second stamp from the Tukey HSD analysis was between the 80 μL K107 PTFE-LN in the 15-minute data set (**Fig. 5.6**) and the 80 μL K103 PTFE-LN in the 30-minute data set (**Fig. 5.7**). This comparison

exists between the best performing PTFE-LN for the 15-minute recovery compared to the worst performing PTFE-LN for the 30-minute recovery set.

The results from the 10 μm PTFE filter and liquid nets both reinforce the lessons from the 1.0 μm experiments while adding slight nuance to liquid net filtration. However, a relatively small sample size of each condition (n=3) is a limitation on the depth of the study. For both pore sizes, the liquid nets improved the rate of release compared to the bare control filters. However, the time to recovery, volume, and viscosity were all different between the two sets. The results from the ANOVA indicate that viscosity and volume significantly affect the performance in release rate for liquid net filtration. For a PTFE-LN with a 10 μm pore size, the conditions that yielded the best results occurred after a 30-minute recovery period with the high-volume-high-viscosity PTFE-LN.

5.3.4. Temperature-Based Recovery

The final experiment with the PTFE filters was conducted to determine the effects of temperature over an extended 24-hour recovery period. A concentration of 1.64×10^6 CFU/mL of *E. coli* in PBS was used during this run. For this experiment, 27 filters were fun through the aerosolization and filtration protocol (**Table G.1**) and set to recover over the course of 24 hours in one of three locations, an incubator set to 40 °C, inside the biological safety cabinet at 26 °C, or in the laboratory refrigerator at 4 °C. Each temperature condition had a set of three 1.0 μm PTFE bare control, and the low (80 μL) and high (160 μL) volume K103 1.0 μm PTFE-LNs. Results from the CFU analysis revealed all filters, including the controls and PTFE-LNs, that underwent recovery at 40 °C had zero CFUs present on all agar plates (**Table G.2**). Lack of *E. coli* colonies present is most likely attributed to their desiccation and death after extended periods at

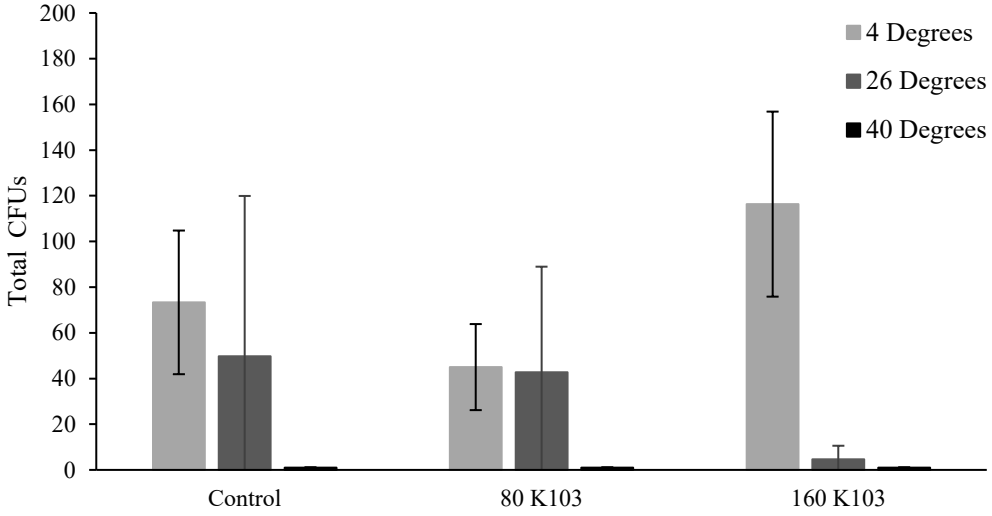

Figure 5.8. Total CFU counts for the 1.0 μm PTFE filters and liquid nets that underwent a 24-hour recovery at 4 ℃ (light grey), 26 ℃ (dark grey), and 40 ℃ (black). The bars represent the average and standard deviation of three independent filters, plotted by infusion volume: dry control, 80 μL of Krytox 103, and 160 μL of Krytox 107, n=3 for each treatment.

relatively high temperature.[162] The Welch two-sample t-tests revealed no significant difference between the PTFE-LNs and the dry controls, shown in **Figure 5.8**. However, ANOVA and Tukey HSD tests did reveal in several key differences. The Tukey HSD post hoc test investigating the data within the temperature groups revealed significance difference between the 26 ℃ and 4 ℃ data sets, P-value 0.03 (0.0250), as well as the 40℃ and 4 ℃ data sets (P=0.0026). Furthermore, multiple significant differences were found within the temperature~volume associations. Most notably, the 160 μL PTFE-LNs between 26 ℃ and 4 ℃ resulted in a P-value of 0.01. The 160 μL PTFE-LNs that recovered at 4 ℃ had the highest totals at 54.3 ±22.4 CFUs, compared to 4.7 ±5.9 CFUs the same PTFE-LN that recovered at 26 ℃. Finally, the 160 μL PTFE-LN at 4 ℃ also had significant difference with both PTFE-LNs at 40 ℃, in which both p-values were 0.009, due to the lack of any CFUs at 40 ℃. In incidence of statistical significance only occurred at the second stamp. Similar to the ANOVA and Tukey HSD conducted on the CFU totals, significant difference was found between the 4℃ (**Fig. 5.9A**)

and 26 °C (**Fig. 5.9B**) with a P-value of 0.001; as well as between 4 °C and 40 °C resulting in a P-value <0.001. Additionally, the 160 µL PTFE-LN within the 4 °C (R-value 0.526 ±0.042) was found to be

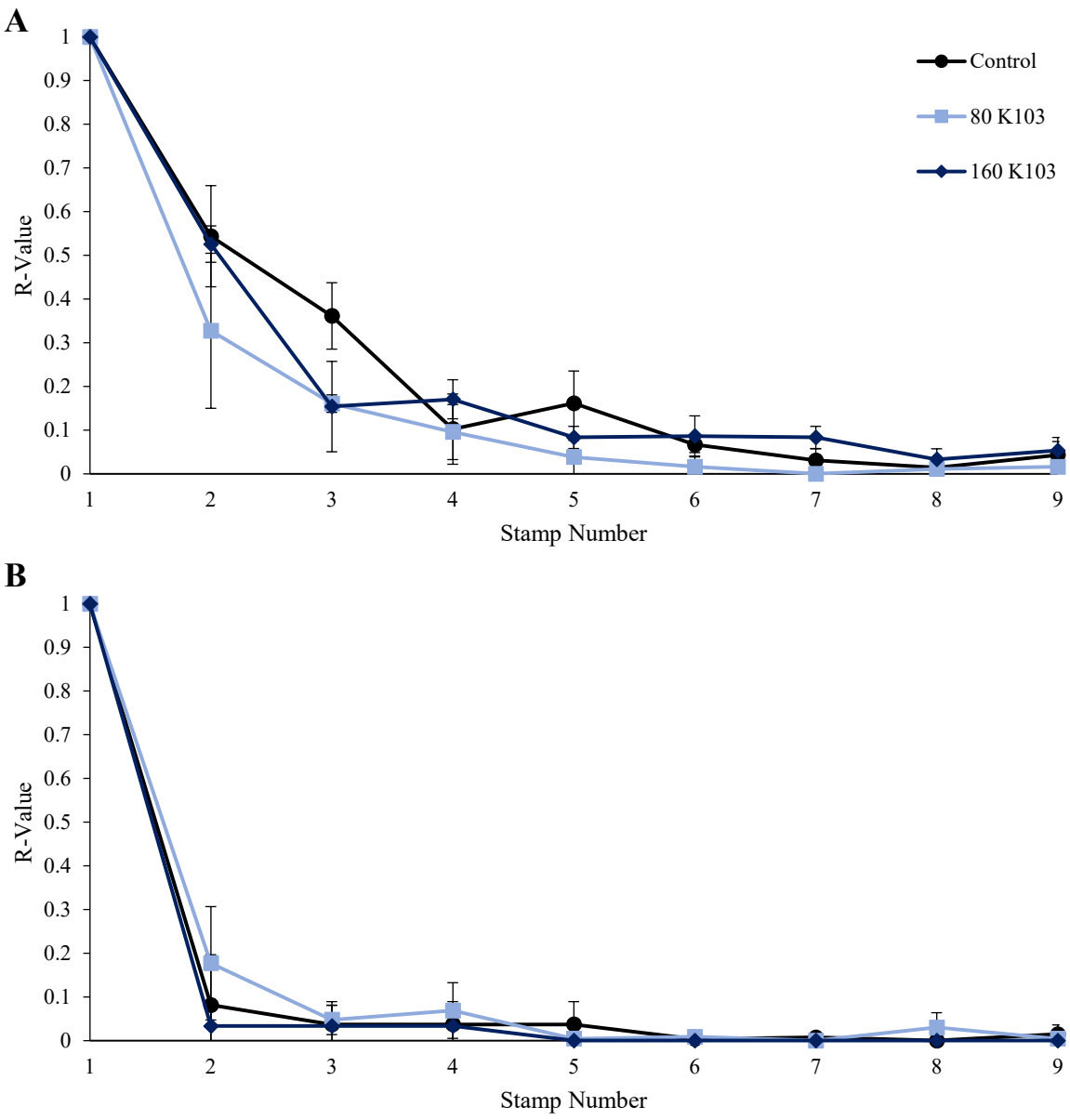

Figure 5.9. Rate of release analysis Total CFU counts for the 1.0 µm PTFE filters and liquid nets that underwent a 24-hour recovery at 4 °C (A), and 26 °C (B). The dry controls (black circles), 80 µL of Krytox 103 (light blue squares), and 160 µL of Krytox 107 (navy blue diamonds) were tested in triplicate (n=3). Due to the lack of any CFUs, the 40 °C recovery data was not included in the figure.

statistically different than the 80 μL PTFE-LN (R-value 0.177 ±0.130) and the 160 μL PTFE-LN (R-value 0.033 ±0.047) of the 26 °C data set, with P-values of 0.03 (0.0265) and 0.002, respectively. These data show that while the 160 μL PTFE-LN of the 4 °C recovery data transferred the most amount of *E. coli*, it took significantly more stamps to release its captured droplets onto the agar plates for culture compared to the 26 °C recovery data. Overall, the results from this experiment continue to support the benefits of using a high-volume low-viscosity PTFE-LN for liquid net filtration. The 160 μL K103 PTFE-LN not only had the highest yield of CFUs transferred while maintaining favorable rate of release values. The higher amount of *E. coli* transferred from liquid nets stored at lower temperatures aligns with basic principles of biological sample preservation.

5.4. Conclusions

The intent of this study was to apply the principles of liquid-infused surfaces to design filters that easily capture bioaerosols and then enable a simple transfer for culture-based analysis. Using commercially available PTFE filters and PFPE infusing liquid, these new liquid nets met the surface property characteristics previously reported in other liquid-infused surfaces and liquid-gated membranes. This study set out to establish the optimal parameters for liquid net filtration by investigating the effects of the PFPE infusion volume, PFPE viscosity, PTFE pore size, recovery phase time, and recovery temperature. LN filtration experiments on the 1.0 μm PTFE filters revealed significant improvements in the rate of release values after a 15-minute recovery phase with the high viscosity liquid nets (P-values 0.006 and 0.001), and even greater significance with the high-volume low-viscosity liquid net (P=0.0005). The better performance of the high-volume low-viscosity 1.0 μm PTFE-LN in releasing surface pathogens

was supported during the 24-hour recovery experiment, where that liquid net configuration outperformed all other liquid nets in total CFUs transferred and cultured. When the pore size of the PTFE filters was increased to 10 μm, an improved rate of release performance over the dry controls was observed after a 30-minute recovery phase with the high-viscosity PTFE-LNs, with P-values of 0.01 and 0.006 for the low- and high-volume liquid nets, respectively. The results of this study support the claim that liquid net filtration improves the performance of filter-based air sampling by improving the filter's (PTFE-LN) rate of release.

5.5. Acknowledgements

The author thanks Junie Fong her contributions to the characterization of the filters, and Prof. Emeritus Bill Halteman for his guidance during the statistical analysis portion of the work. This work was supported by the National Science Foundation [1939710]; the University of Maine Research Reinvestment Funds; the University of Maine Graduate School of Biomedical Science and Engineering; and the Maine Space Grant Consortium Graduate Fellowship. Parts of this chapter are being prepared for peer-review publication and have been incorporated into a patent application.

CHAPTER 6

INVESTIGATION OF NON-TRADITIONAL LIQUID-INFUSED SURFACES FOR LIQUID NET FILTRATION

6.1. Introduction

The success of the PTFE and PFPE liquid nets provoked the curiosity to explore non-traditional liquid-infused surface combinations to form liquid nets. With traditional liquid-infused surfaces, there is a chemical affinity between the substrate's surface and the infusing, or lubricating, oil. To expand outside of traditional LISs would mean that the two materials are no longer limited to an established chemical affinity to fabricate liquid nets that improve bioaerosol capture and release mechanisms. In this chapter, two non-traditional filter substrates are tested for LN filtration, meltblown polypropylene high-efficiency particulate air (HEPA) filters and cellulose nanofiber mats (CNFM).

The first substrate investigated for LN filtration was the meltblown polypropylene. HEPA filters are designed for long-term filtration, only needing to be replaced on an annual or semi-annual basis, but modifications could allow the existing infrastructure to become a key contributor to biosurveillance efforts. While not a conventional means of air sampling, HEPA filters play a critical role in the infection control strategies.[140] A recent study using a portable HEPA filtration unit in a simulated COVID isolation room reached upwards of 20 air changes per hour, above the recommended 12, while capturing 98% of the surrogate aerosols.[163] Upgrading the existing air handling infrastructure in areas where bioaerosol contamination is a high-risk environment, such as hospitals, travel hubs, entertainment venues, and schools, to

liquid net filtration could open a new method for monitoring the presence and spread of biological threats.

In this set of experiments, the surface characterization experiments conducted on HEPA filters was built on the foundation laid for PTFE analysis. In addition to the SEM images for surface topography, contact angle analysis for bare filter wetting behavior, and sliding angle tests for dynamic interactions between the PFPE oil and sample droplet, a crystal violet (CV) staining test was added. The CV molecule is positively charged and will stain the negative charged bacteria and organic matter used in this study. The CV test will serve as an indicator of how well the PFPE oil is wetting the polypropylene fibers. If a strong physical interaction exists between the fibers and the PFPE oil, then the CV will be repelled, and filters will have minimal staining. Applying the lessons from PTFE-LN filtration experiments, the HEPA filters were wetted with the low viscosity K103 with a high volume, near the filter's saturation point. After aerosolization of the *E. coli*, dry controls and HEPA-LNs were isolated for a 15-minute recovery phase and then stamped for culture analysis. The CV staining and liquid net filtration results from the HEPA-LNs demonstrate that, in the absence of strong chemical affinity between the two materials, physical interactions like capillary forces enabled the PFPE oil and HEPA filters to form stable liquid nets. The results from the aerosolization experiments demonstrated that HEPA-LNs provided a consistent release of the captured *E. coli* droplets, improving upon the bare control HEPA filters.

The successful expansion of liquid net filtration to the meltblown polypropylene HEPA filters meant that the chemical affinity between the filter's material and the lubricant oil were required to create functional liquid layers. Looking to again test the limits of liquid net

filtration, another non-LIS combination in cellulose and PFPE is explored. The second filter substrate tested for LN filtration was a cellulose nanofiber mat (CNFM). Products derived from renewable resources, previously mentioned in **Chapter 2**, are increasingly important to provide climate-friendly solutions. If CNFMs have success in LN filtration then LNs could be manufactured by both synthetic and biological polymers.

Surface characterization results from the HEPA experiments demonstrated that the LNs do not need to have a low tilt angle in order improve the rate of release. However, the improvement of the HEPA-LNs to repel the CV may be an important indicator of success. Thus, the dry control CNFMs and CFNM-LNs were tested for their retention of CV stain. Continuing with the lessons from both PTFE and HEPA filtration experiments, the CNFMs were infused with the low viscosity K103 with a high volume, near the filter's saturation point. Again, based on the previous results dry controls and CNFM-LNs were isolated for a 15-minute recovery phase and then stamped to transfer captured *E. coli* for culture analysis. The results presented in this chapter demonstrate that a lack of physical interaction between the CNFMs and PFPE oil, like capillary forces, in addition to the absence of chemical affinity between the two materials rendered CNFM-PFPE filters a non-viable option for liquid net filtration.

6.2. Materials and Methods

6.2.1. HEPA Surface Characterization

All meltblown polypropylene discs were cut from H13 HEPA filters (Nanjing Blue Sky Filter Co.) to 17 mm diameter, ~2.27 cm^2. Liquid layer stability tests were performed to determine the maximum wetting volume of K130 with 160 μL and 320 μL. Six HEPA filters were wetted with 160 μL, and another six wetted with 320 μL. Initial masses of the membranes

were recorded at 0 h. Then three filters from each volume were left horizontal (n=3), while the other three were tilted vertical (n=3) for 24 hours. Masses of the wetted membranes were recorded, and statistical analysis was performed via Welch two sample t-test in R-Studio. Surface topography images via SEM, contact and sliding angle measurements detailed in **Section 5.2.1** were repeated for the HEPA filters, with 160 μL K103 wetted HEPA filters used in the sliding angle tests. For the CV staining tests, five dry control HEPA filters and five 160 μL K103 HEPA-LN filters were placed into six-well plates. Each filter or LN was placed into its own well for 10 minutes in a 5 mL bath of 0.1% CV. Filters were then washed in baths of DI water until excess CV was no longer leaving the sample. Images were collected with the EOS 5D Mark II camera and uploaded to ImageJ. Percent biofilm coverage was conducted by converting the image to 8-bit grayscale, setting manual threshold pixel values to a lower limit value of 1 and upper limit of 140, marking the entire filter as the region of interest, and measuring the area as percent coverage.

6.2.2. CNFM Surface Characterization

Electrospun cellulose nanofiber mats were fabricated and provided by Shao-Hsiang "Joe" Hung in the lab of Jessica Schiffman at the University of Massachusetts Amherst. Prior to shipping, characterization at the Schiffman lab indicated the CNFM had an average thickness of 70-90 μm and effective pore size of 4–8 μm. CNFMs prepared for contact angle and sliding angle measurements were cut to 17 mm diameter, 2.27 cm^2. Contact angle, SEM, and sliding angle measurements were replicated from protocol in **Section 5.2.1**; however, filters were only tested once per filter (n=3) and the CNFM-LNs were wetted with 40 μL of K103 with a volume

per area of 13.3 ±1.8 μL/cm^2. The CV staining protocol from **Section 6.2.1** was repeated for the dry control CNFMs (n=5) and 40 μL K103 CNFMs (n=5), in which filters were cut to 25 mm.

6.2.3. HEPA Aerosol Filtration

Liquid net filtration experiments were conducted with HEPA filters cut to the size of the filter housing, 17 mm or 2.27 cm^2. Each filtration experiment had an alternating run order (available in **Appendix H)** between the dry control HEPA filters (n=3) and HEPA-LNs (n=3), wetted with 160 μL K103. The aerosolization and filtration protocol followed was based on the **Section 4.4.2**, again with the additional step in which the filtration system and loaded diffuser were run for a 15-minute build-up phase before the first HEPA filter was inserted and cycled. The recovery time was set to 15 minutes before the physical stamping was conducted nine times onto the LB agar plates. Rate of release calculations (**Section 5.2.5**) were conducted for each filter. The statistical analysis conducted between the dry controls and LNs was performed in R-Studio, following the protocol described in **Section 5.2.2**.

6.2.4. CNFM Aerosol Filtration

Six CNFMs were cut to the size of the filter housing, 2.27 cm^2, so each filter condition had an n=3. While the three controls were left as is, the three liquid nets were wetted with 40 μL of K103. The aerosolization and filtration protocol followed was based on the **Section 4.4.2**, again with the additional step in which the filtration system and loaded diffuser were run for a 15-minute build-up phase before the first CFNM was inserted and cycled. The concentration of the *E. coli* and PBS solution loaded into the diffuser for this experiment was 1.46×10^6 CFU/mL. The recovery time was set to 15 minutes before the physical stamping was conducted nine times

onto the LB agar plates. The filters were run in alternating order, available in **Appendix I**. Rate of release calculations (**Section 5.2.5**) were conducted for each filter.

6.3. Results and Discussion

6.3.1. HEPA Surface Characterization

The first experiment conducted was the investigation of the liquid layer's stability over the course of 24 hours on the HEPA filters. For the HEPA filters wetted with 160 μL of K103, the initial volume/area measurement (n=6) was 56.8 ±3.7 μL/cm^2 and went down 43.8 ±3.7 μL/cm^2 for the horizontal filters (n=3) and 40.9 ±0.5 μL/cm^2 for the vertical filters (n=3). This loss of Krytox over time was found to not be significant (P=0.2) via the Mann-Whitney test. In conducting the same test with 320 μL, the initial infusing value was 55.7 ±7.6 μL/cm^2 (n=6). After 24 hours, the horizontal HEPA filters (n=3) were at 39.4 ±2.6 μL/cm^2 and the vertical filters (n=3) measured at 41.7 ±1.8 μL/cm^2. Again, this drop in Krytox was found to not be significant (P=0.5) via the Welch two sample t-test. The 24-hour values were compared between the two volumes and were again found to be not significantly different (P=0.3). This is due to the HEPA filters reaching their saturation point and the 320 μL sample had significant volume bleed-off of the Krytox oil from the filter. Thus, the HEPA filters wetted with 320 μL of K103 essentially lost ~160 μL due to the immediate oversaturation of the HEPA filter. This experiment provided the information needed to use 160 μL as the volume for fabricating HEPA-LNs, as well as provided evidence to support the claim that HEPA filters would retain the PFPE lubricant oil via weak-chemical association and/or physical interactions like capillary forces.

The surface topography of the meltblown polypropylene HEPA filters is visible in **Figure 6.1A**. As surface roughness increases, capillary forces between the surfaces and wetting

liquids increases.[103,164] The relatively large fiber and resulting pore network is noted, in comparison to the 1.0 PTFE filters in **Figure 5.2A**. The contact angle measurements (**Fig. 6.1B**) on the HEPA filters resulted in an angle of 89 ±23°. The filter with the lowest contact angle was 67 ±6° compared to the largest contact angle at 118 ±3°. The meltblown fabrication process created irregular surface topography (**Fig. 6.1A**) creating a non-homogeneous surface texture, accounting for the variability in contact angle results. Results from the sliding angle measurements yielded failure. These failures are caused by the droplets being pinned to the surface of the filters and not being able to slide at angles ≤45°, the cutoff for the sliding angle test. This pinning is most likely attributed to the roughness of the surface topography, and the PFPE oil only coating the fibers and not forming a bed of liquid for the droplet to freely move atop of. For the final surface characterization assay, HEPA filters were also submerged in CV to understand the repellent nature of the bare control HEPA filters and the HEPA-LNs. Representative images of the CV-stained control and 160 μL K103 HEPA filters are shown in **Figures 6.1C*i*** and **6.1C*ii***. Percent biofilm coverage for the control HEPA filters was 93.3 ±3.9% compared to the HEPA-LNs at 15.8 ±6.4%, and a statistically significant difference determined via the Welch two sample t-test (P-value < 0.001). These results reinforce the claim from the liquid layer stability experiments, in

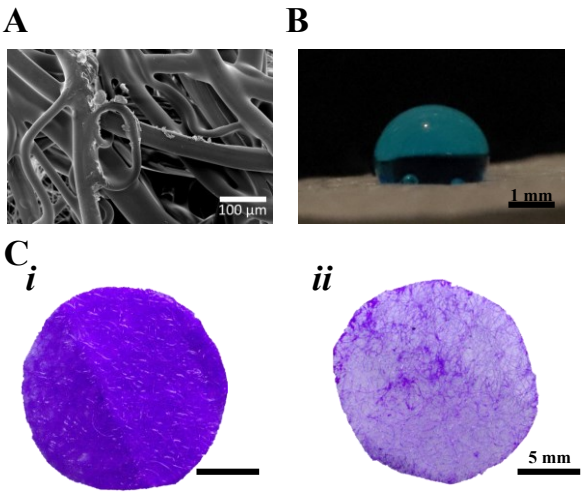

Figure 6.1. A) Surface topography of the HEPA filter via SEM at 200× magnification. B) Representative images of the HEPA's 89 ±23° contact angle measurement. C) CV-stained control (*i*) and 160 μL K103 liquid net (*ii*).

which the polypropylene fibers and PFPE lubricant oil have some interaction to resist the adhesion of the CV dye. This interaction is most likely a combination of weak fluorine-hydrogen bonding with capillary forces between the fibers and oil.[164,165]

6.3.2. CNFM Surface Characterization

The hydrophilicity of the cellulose in the CNFMs was confirmed as the water droplet completely wetted the mats, resulting in a contact angle of 0 ±0°. Due to the droplets completely wetting the CNFMs, each mat was only tested once. This trend again continued for the sliding angle measurements, in which both the dry controls and 40 µL K103 CNFMs did not register a sliding angle. The water droplet wetted the bare control CNFMs immediately. Whereas the droplet began to integrate into the CNFM-LN immediately and eventually fully wetted the CNFM-LN, again unable to register a sliding angle and failing the test. The failure of the CNFM-LN to register a sliding angle is indicative of the incompatibility between the CNFM and PFPE lubricant oil. For the water droplet to fully wet the CNFM-LN suggests that the PFPE oil is not being retained by physical interactions, such as capillary forces, nor a chemical affinity.

Images of the CNFM's surface topography is shown in **Figure 6.2A**. Representative

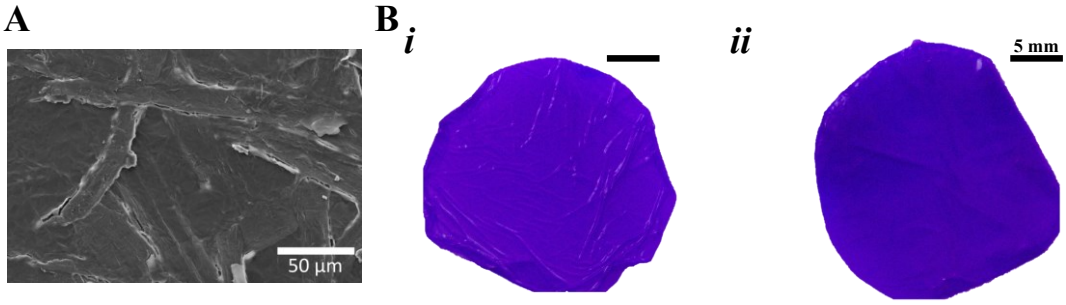

Figure 6.2. A) SEM image at 500× magnification of CNFM's surface. B) Representative images of bare control CNFM (*i*) and CNFM wetted with 40 µL K103 (*ii*) after crystal violet staining. Both samples are fully stained by the CV solution.

images of the CV retention tests are shown for the bare control, **Figure 6.2B*i***, and CNFM-LN, **Figure 6.2B*ii***. As seen in **Figure 6.2**, both the control CNFM and CNFM-LN were stained by the CV solution across the entire filters' cross-sectional area. These results align with the failure exhibited in the sliding angle measurements. This repeated failure of the CNFM-LNs to repel the CV solution supports the claim that the combination of cellulose nanofibers and PFPE oil do not form a stable LN, and thus are incapable of releasing captured airborne pathogens.

6.3.3. HEPA Aerosol Filtration

Two independent data sets were collected on the liquid net filtration experiments for the HEPA filters. The first data set had a starting concentration of 1.43×10^{6} CFU/mL, whereas the second liquid net filtration experiment measured of 6.80×10^{5} CFU/mL. The rate of release calculations were conducted for each independent data set, **Figure 6.3*i*** and **6.3,** with the control HEPA (grey lines with circle markers) and HEPA-LN (blue lines and diamond markers) filters. Statistical analysis, using the Welch two sample t-test, at the fourth stamp found a significant difference (P=0.03) between the bare control R-value of 1.16 ±0.24 and the HEPA-LN's value of 0.41 ±0.15. Since the rate of release calculation is a normalized metric, the two data sets were able to be combined for analysis. The combined rate of release calculations resulted in significant difference between the dry controls and HEPA-LNs at stamps 3 and 4, both calculations via the Welch two sample t-test. At the third stamp, the dry controls had an R-Value of 2.37 ±1.62 compared to the liquid nets' 0.57 ±0.25, resulting in a P-value of 0.04. Next, the P-value at the fourth stamp was 0.04 where the rate of release for the dry controls measured 2.19 ±1.56, compared to 0.48 ±0.15 calculated for the HEPA-LNs. One observation from the rate of release data is the irregular behavior of the bare control HEPA filters. The first data set

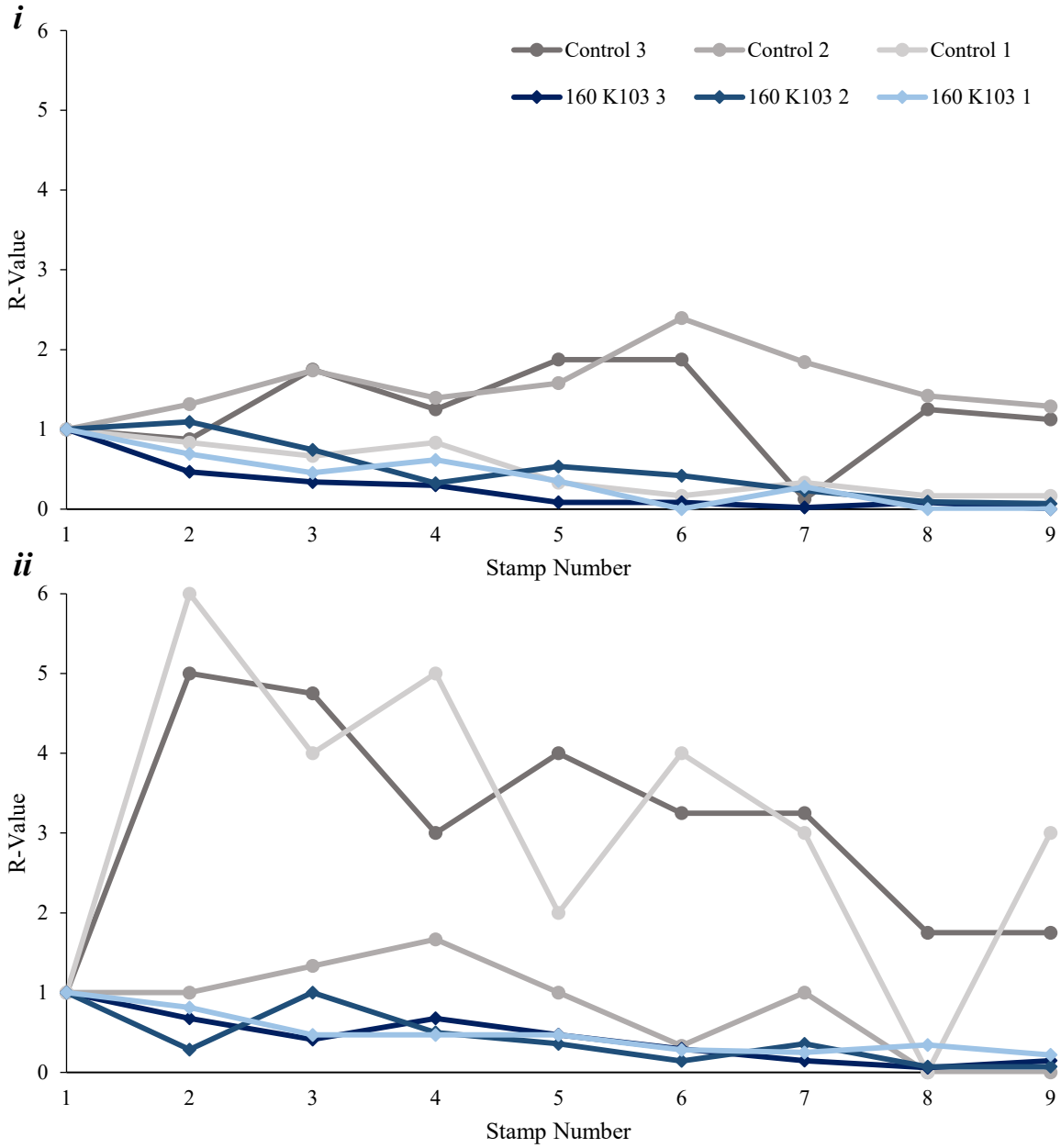

Figure 6.3. Rate of release analysis for the first (*i)* and second (*ii*) data sets using meltblown polypropylene HEPA filters. The dry control HEPA filters (grey circles) and 160 μL K103 HEPA-LNs (blue diamonds) are graphed as individual filter performance.

maintained a rate of release greater than or equal to one (R ≥ 1) for 63.0% and 88.9% of all measured stamps in the first (**Table H.2)** and second (**Table H.5)** data sets, respectively. Conversely, the HEPA-LNs recorded a rate of release value equal to or less than one (R ≤ 1) for

96.3 % (**Table H.2**) and 100% (**Table H.5**) of their recorded stamps. Furthermore, the bare control filters had an increased amount of CFUs transferred from the previous stamp 33.3% of the time, the same incidence rate for both data sets. Compared to the HEPA-LNs, this increase in transfer occurred 14.8% and 18.5% of the time in the first in second data set, respectively. These trends in release rate highlight the stabilizing effect that the PFPE oil has on the HEPA filters for liquid net filtration. The rate of release consistently decreases towards zero with each transfer and was significantly lower for the HEPA-LNs compared to the dry controls for both stamps 3 and 4. These results demonstrate that the stability previously seen in the liquid layer stability and CV staining experiments translated to the improvements in rate of release by using liquid net filtration.

Examination of the transferred *E. coli* colonies during the first stamp (**Table H.3**) are noticeably higher for the HEPA-LNs, 52.7 ±11.0 CFUs, over the bare control's 19.3 ±13.3 CFUs, although the results from the t-test were just outside of the confidence interval (P=0.054). This was again the case for the second data set (**Table H.7**) with the first stamp transfers for the control HEPA filters coming to 2.67 ±1.25 CFUs, compared to 26.7 ±8.99 CFUs for the HEPA-LNs (P=0.06). However, the cumulative CFU transfer counts did not align between the data sets, however, neither set contained significant difference between the controls and the liquid nets. The first data set had a higher total count for the controls (**Table H.4**), whereas the second data set had greater total transfer for with the HEPA-LNs (**Table H.8**).

A major effort was invested into chemical removal of the captured *E. coli* droplets in order to simplify the extraction process. A chemical removal process would eliminate the need for multiple transfer stamps and provide a scalable method for liquid nets. The protocol

involved a two-liquid solution. The first liquid, Novec 7100 Engineering Fluid (3M), a non-toxic hydrofluoroether solvent,[166] was selected to dissolve the PFPE oil away from the filter. The second liquid selected was PBS, where the charged negatively charged *E. coli* would migrate for extraction and analysis. However, detailed in **Appendix J** are the multiple iterations of this process that failed. These failures are most likely caused by the Novec fluid interacting with the *E. coli* in such a way that prevents their growth on agar plates. Future studies in which the downstream analysis is changed from culturing on agar plates to real time-polymerase chain reaction analysis may circumvent the reported failures and open the door for chemical extraction.

6.3.4. CNFM Aerosol Filtration

Again, the rate of release was used as the chief determinant of filter performance, shown in **Figure 6.4**, with each CNFM and CNFM-LN graphed as individual filter performance. During the stamping process the second and third CNFMs ripped down the center after four and seven stamps, respectively. None of the CNFM-LNs were destroyed during the stamping process. The control CNFMs (grey lines with circular markers) rate of release values of the control decreased towards zero as the stamp number increased, with exception to CNFM 1 stamp 3 and CNFM3 stamp 4, whereas the CNFM-LNs (blue lines with diamond markers) never fell below a release rate less than 0.5 aside from CNFM-LN 3's final stamp and when zero CFUs were transferred with CNFM-LN 1. The median number of CFUs transferred during the first stamp of the control CFNMs was 50, compared to that of 16 for the CNFM-LNs. This trend continued as the total CFUs transferred for the control CNFMs was 227 compared to 127 of the CNFM-LNs. The lack in chemical affinity between the cellulose-based filter and the PFPE

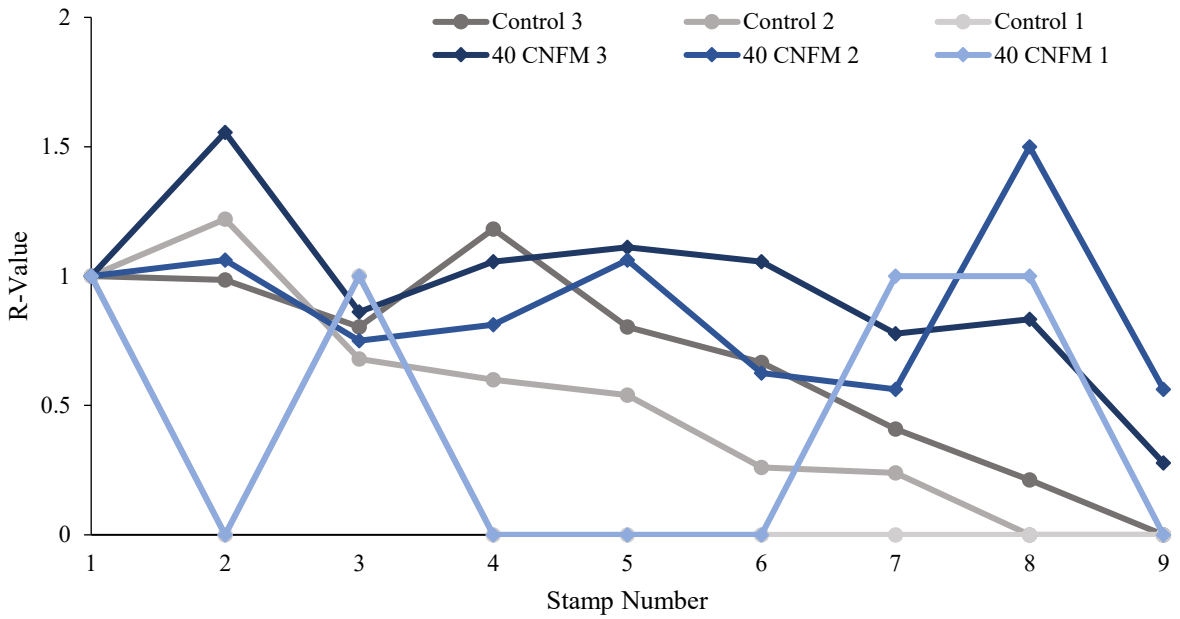

Figure 6.4. CNFM rate of release analysis, where each dry control (grey circles) and 40 µL K103 CNFM (blue diamonds) is graphed as individual filter performance.

lubricant oil is most likely the cause for inconsistent release of the captured aerosol. The inconsistent rate of release coupled with (crystal violet data) suggest that cellulose nanofiber mats should not be fabricated for use in liquid net filtration.

6.4. Conclusions

Due to the success of the PTFE filters for liquid net filtration, the idea was expanded to non-traditional LISs. Here, it is demonstrated that meltblown polypropylene HEPA filters are also a viable filter material to form liquid nets when wetted with a high-volume low-viscosity PFPE oil. Despite failing the sliding angle test, the HEPA-LNs maintained a stable liquid layer after 24 hours and repelled a significant amount of CV stain. This combination of results suggest that capillary forces are maintaining a coat of PFPE oil around the HEPA's fibers, forming liquid net. More evidence for this claim was added when the aerosolization rate of release data was significantly better for the HEPA-LNs compared to the values of the dry controls. Surprisingly,

even the first stamp transfer was improved for the HEPA-LNs compared to the dry controls. These results demonstrate that HEPA filters, a widely-used air filtration material, can successfully serve as the substrate for liquid nets and outperform bare HEPA filters in releasing capture bacteria. The failure of the CNFM-LNs to improve upon the filtration performance of the bare CNFMs suggests the need for either chemical affinity between the filter and the infusing oil, as in the case for PTFE-LNs.

6.5. Acknowledgements

The author thanks Shao-Hsiang "Joe" Hung and Dr. Jessica Schiffman for providing the CNFMs, along with Junie Fong and Justin Hardcastle for their contributions to the characterization data. This work was supported by the National Science Foundation [1939710]; the University of Maine Research Reinvestment Funds; the University of Maine Graduate School of Biomedical Science and Engineering; and the Maine Space Grant Consortium Graduate Fellowship. Parts of this chapter are being prepared for peer-review publication and have been incorporated into a patent application.

CHAPTER 7

CONCLUSIONS AND RECOMMENDATIONS

As previously mentioned, the lack of direct applications using liquid-infused surfaces was the motivation to contribute meaningful research towards the progress of the field. In this dissertation, two successful applications of liquid-infused surfaces with technology transfer capabilities have been developed.

The first engineering solution delivered a low-cost paper-based platform that simultaneously localized and concentrated waterborne samples. In **Chapter 2**, the issue of sample loss within point-of-care devices was established as the motivation to provide a new method of handling biological samples for downstream analysis. It was then demonstrated how mass-manufactured SRP could be infused, in one step, with PDMS oil to create the paper-based liquid-infused surfaces that resisted bacterial adhesion. Then, in **Chapter 3**, the various 3D geometries were shown in how the design of the paper-based system could intrinsically multiplex a large volume, or an array of manual aliquots could be localized and concentrated into predetermined zones. The hallmark claim from this chapter was the concentration of *S. aureus* and especially *E. coli* after a 10-fold evaporation in the solution, *E. coli* had concentrated nearly 2.5-fold above the expected value.

The second direct application of liquid-infused surfaces was the creation of liquid net filtration, laid out in **Chapter 4**. The need for liquid net filtration stemmed from the lack of standardization across air sampling methods, but especially driven by the minimized analytical techniques filter-based air sampling enable. **Chapter 5** established that liquid nets could be

fabricated via traditional liquid-infused surface principles in matching the chemistries of the PTFE filter and the PFPE infusing oil. Optimization of the 1.0 μm PTFE-LNs found that a high-volume low-viscosity liquid net significantly improved the rate at which the captured *E. coli* droplets were released compared to the bare control filters after a 15-minute recovery phase. Additional tests showed that similar results could be obtained for 10 μm PTFE-LNs, but with the high-viscosity PFPE infusing oil after a 30-minute recovery phase. These results meant that liquid net filtration provided a new method that improved the rate at which captured bioaerosol would be released for culture analysis, potentially improving the odds for detection of low-concentration biological threats.

With the success of the PTFE filters forming liquid nets, non-traditional liquid-infused surfaces were explored. The first material investigated was meltblown polypropylene HEPA filters, detailed in **Chapter 6**. Surface characterization tests supported the claim that the HEPA filters and the low-viscosity PFPE oil formed a stable association, most likely from capillary forces, that enabled the liquid net filtration without matching chemistries. Results from the aerosolization and filtration experiments demonstrated that the HEPA-LNs significantly improved the rate of release for the captured *E. coli*, but it also improved the first stamp transfer totals (narrowly outside of the 95% confidence interval). However, the success found with the HEPA filters did not continue for the cellulose nanofiber mats. The failure of the CNFMs to form liquid nets confirms the hypothesis that either strong chemical affinity or strong physical interactions, like capillary forces, are required between the filter material and the infusing/wetting oil in order to form liquid nets.

While the physical removal of the bioaerosol for culture analysis is a valid technique currently implemented in air sample handling,[144] it has its limitations. Chemical extraction of the captured bioaerosols will not only aid in scaling liquid net filtration for high surface area filters. Furthermore, it will most likely be a one-step removal, eliminating the multiple stamps needed to fully remove all captured pathogens as demonstrated by **Chapters 5** and **6**. While attempts to use a combination of Novec 7100 engineering fluid and PBS failed (**Appendix J)** further investigation with aerosolized viruses analyzed via real time-polymerase chain reaction and infectivity assays are active projects in collaboration with the Dr. Melissa Maginnis and her team.

REFERENCES

(1) Sin, M. L.; Mach, K. E.; Wong, P. K.; Liao, J. C. Advances and Challenges in Biosensor-Based Diagnosis of Infectious Diseases. *Expert Rev Mol Diagn* **2014**, *14* (2), 225–244.

(2) Wang, S.; Lifson, M. A.; Inci, F.; Liang, L.-G.; Sheng, Y.-F.; Demirci, U. Advances in Addressing Technical Challenges of Point-of-Care Diagnostics in Resource-Limited Settings. *Expert Rev Mol Diagn* **2016**, *16* (4), 449–459.

(3) Clatworthy, A. E.; Pierson, E.; Hung, D. T. Targeting Virulence: A New Paradigm for Antimicrobial Therapy. *Nat. Chem. Biol.* **2007**, *3* (9), 541–548.

(4) Laxminarayan, R.; Duse, A.; Wattal, C.; Zaidi, A. K. M.; Wertheim, H. F. L.; Sumpradit, N.; Vlieghe, E.; Hara, G. L.; Gould, I. M.; Goossens, H.; et al. Antibiotic Resistance-the Need for Global Solutions. *The Lancet Infectious Diseases*. 2013, pp 1057–1098.

(5) Inpatient Care for Septicemia or Sepsis: A Challenge for Patients and Hospitals. *Natl. Cent. Heal. Stat. Data Br.* **2011**, *62*.

(6) Edelsberg, J.; Weycker, D.; Barron, R.; Li, X.; Wu, H.; Oster, G.; Badre, S.; Langeberg, W. J.; Weber, D. J. Prevalence of Antibiotic Resistance in US Hospitals. *Diagn. Microbiol. Infect. Dis.* **2014**, *78* (3), 255–262.

(7) Noyce, R. S.; Lederman, S.; Evans, D. H. Construction of an Infectious Horsepox Virus Vaccine from Chemically Synthesized DNA Fragments. *PLoS One* **2018**, *13* (1), 1–16.

(8) Ozancih, R.; Bartholomew, R.; Bruckner-Lea, C.; Hess, C.; Arce, J. *Biodetection Technologies for First Responders: 2015 Edition*; 2015.

(9) Imperiale, M.; Boyle, P.; Carr, P. A.; Densmore, D.; DiEuliis, D.; Ellington, A.; Gronvall, G. K.; Haas, C.; Kanabrocki, J.; Morgan, K.; et al. *Biodefense in the Age of Synthetic Biology*; The National Academies Press: Washington D.C., 2018.

(10) Yang, Y.; Noviana, E.; Nguyen, M. P.; Geiss, B. J.; Dandy, D. S.; Henry, C. S. Paper-Based Microfluidic Devices: Emerging Themes and Applications. **2017**.

(11) Yetisen, A. K.; Akram, M. S.; Lowe, C. R. Paper-Based Microfluidic Point-of-Care Diagnostic Devices. *Lab Chip* **2013**, *13* (12), 2210–2251.

(12) Drain, P. K.; Hyle, E. P.; Noubary, F.; Freedberg, K. A.; Wilson, D.; Bishai, W. R.; Rodriguez, W.; Bassett, I. V. Diagnostic Point-of-Care Tests in Resource-Limited Settings. *Lancet. Infect. Dis.* **2014**, *14* (3), 239–249.

(13) Volpatti, L. R.; Yetisen, A. K. Commercialization of 3D-Printed Microfluidic Devices. *Trends Biotechnol.* **2014**, *32* (7), 347–350.

(14) Xu, H.; Clarke, A.; Rothstein, J. P.; Poole, R. J. Viscoelastic Drops Moving on Hydrophilic and Superhydrophobic Surfaces. *J. Colloid Interface Sci.* **2018**, *513*, 53–61.

(15) Wong, T.-S.; Kang, S. H.; Tang, S. K. Y.; Smythe, E. J.; Hatton, B. D.; Grinthal, A.; Aizenberg, J. Bioinspired Self-Repairing Slippery Surfaces with Pressure-Stable Omniphobicity. *Nature* **2011**, *477* (7365), 443–447.

(16) Howell, C.; Grinthal, A.; Sunny, S.; Aizenberg, M.; Aizenberg, J.; Howell, P. C. Designing Liquid-Infused Surfaces for Medical Applications: A Review. *Adv. Mater.* **2018**, No. 1802724, 79.

(17) Juthani, N.; Howell, C.; Ledoux, H.; Sotiri, I.; Kelso, S.; Kovalenko, Y.; Tajik, A.; Vu, T. L.; Lin, J. J.; Sutton, A.; et al. Infused Polymers for Cell Sheet Release. *Sci. Rep.* **2016**, *6*, 9.

(18) Kovalenko, Y.; Sotiri, I.; Timonen, J. V. I.; Overton, J. C.; Holmes, G.; Aizenberg, J.; Howell, C. Bacterial Interactions with Immobilized Liquid Layers. *Adv. Healthc. Mater.* **2016**, 1–9.

(19) Overton, J. C.; Weigang, A.; Howell, C. Passive Flux Recovery in Protein-Fouled Liquid-Gated Membranes. *J. Memb. Sci.* **2017**, *539*, 257–262.

(20) Mackie, G.; Gao, L.; Yau, S.; Leslie, D. C.; Waterhouse, A. Clinical Potential of Immobilized Liquid Interfaces: Perspectives on Biological Interactions. *Trends Biotechnol.* **2018**, 1–13.

(21) Sotiri, I.; Overton, J. C.; Waterhouse, A.; Howell, C. Immobilized Liquid Layers: A New Approach to Anti-Adhesion Surface for Medical Applications. *Exp. Biol. Med.* **2016**, *241* (9), 909–918.

(22) Manna, U.; Lynn, D. M. Fabrication of Liquid-Infused Surfaces Using Reactive Polymer Multilayers: Principles for Manipulating the Behaviors and Mobilities of Aqueous Fluids on Slippery Liquid Interfaces. *Adv. Mater.* **2015**, *27* (19), 3007–3012.

(23) Hao, C.; Liu, Y.; Chen, X.; Li, J.; Zhang, M.; Zhao, Y.; Wang, Z. Bioinspired Interfacial Materials with Enhanced Drop Mobility: From Fundamentals to Multifunctional Applications. *Small* **2016**, *12* (14), 1825–1839.

(24) Mistura, G.; Pierno, M. Drop Mobility on Chemically Heterogeneous and Lubricant-Impregnated Surfaces. *Adv. Phys. X* **2017**, *2* (3), 591–607.

(25) Quéré, D. Non-Sticking Drops. *Reports Prog. Phys.* **2005**, *68* (11), 2495–2532.

(26) Li, J.; Ueda, E.; Paulssen, D.; Levkin, P. A. Slippery Lubricant-Infused Surfaces: Properties and Emerging Applications. *Adv. Funct. Mater.* **2018**, *1802317*, 1802317.

(27) He, W.; Liu, P.; Zhang, J.; Yao, X. Emerging Applications of Bioinspired Slippery Surfaces in Biomedical Fields. *Chem. - A Eur. J.* **2018**, *24* (56), 14864–14877.

(28) Lafuma, A.; Quéré, D. Slippery Pre-Suffused Surfaces. *EPL* **2011**, *96* (56001).

(29) Smith, J. D.; Dhiman, R.; Anand, S.; Reza-Garduno, E.; Cohen, R. E.; McKinley, G. H.; Varanasi, K. K. Droplet Mobility on Lubricant-Impregnated Surfaces. *Soft Matter* **2013**, *9* (6), 1772–1780.

(30) Gao, L.; McCarthy, T. J. Contact Angle Hysteresis Explained. *Langmuir* **2006**, *22* (14), 6234–6237.

(31) Daniel, D.; Timonen, J. V. I.; Li, R.; Velling, S. J.; Aizenberg, J. Oleoplaning Droplets on Lubricated Surfaces. *Nat. Phys.* **2017**, *13* (10), 1020–1025.

(32) Preston, D. J.; Song, Y.; Lu, Z.; Antao, D. S.; Wang, E. N. Design of Lubricant Infused Surfaces. *ACS Appl. Mater. Interfaces* **2017**, *9* (48), 42383–42392.

(33) Keiser, A.; Keiser, L.; Clanet, C.; Quéré, D. Drop Friction on Liquid-Infused Materials. *Soft Matter* **2017**, *13* (39), 6981–6987.

(34) Guan, J. H.; Wells, G. G.; Xu, B.; McHale, G.; Wood, D.; Martin, J.; Stuart-Cole, S. Evaporation of Sessile Droplets on Slippery Liquid-Infused Porous Surfaces (SLIPS). *Langmuir* **2015**, *31* (43), 11781–11789.

(35) Kreder, M. J.; Daniel, D.; Tetreault, A.; Cao, Z.; Lemaire, B.; Timonen, J. V. I.; Aizenberg, J. Film Dynamics and Lubricant Depletion by Droplets Moving on Lubricated Surfaces. *Phys. Fluid Dyn.* **2018**, 1–10.

(36) Howell, C.; Vu, T. L.; Johnson, C. P.; Hou, X.; Ahanotu, O.; Alvarenga, J.; Leslie, D. C.; Uzun, O.; Waterhouse, A.; Kim, P.; et al. Stability of Surface-Immobilized Lubricant Interfaces under Flow. *Chem. Mater.* **2015**, *27* (5), 1792–1800.

(37) Sett, S.; Yan, X.; Barac, G.; Bolton, L.; Miljkovic, N. Lubricant-Infused Surfaces for Low Surface Tension Fluids: Promise vs Reality. *ACS Appl. Mater. Interfaces* **2017**, *9*, 36400–36408.

(38) Esteves, C. Self-Healing Functional Surfaces. *Adv. Mater. Interfaces* **2018**, *1800293*, 1–18.

(39) Howell, C.; Vu, T. L.; Lin, J. J.; Kolle, S.; Juthani, N.; Watson, E.; Weaver, J. C.; Alvarenga, J.; Aizenberg, J. Self-Replenishing Vascularized Fouling-Release Surfaces. *ACS Appl. Mater. Interfaces* **2014**, *6* (15), 13299–13307.

(40) Aizenberg, J.; Aizenberg, M.; Cui, J.; Dunn, S.; Hatton, B. D.; Howell, C.; Kim, P.; Wong, T.-S.; Yao, X. Slippery Self-Lubricating Polymer Surfaces. US Patent 9963597 B2, 2018.

(41) Cui, J.; Daniel, D.; Grinthal, A.; Lin, K.; Aizenberg, J. Dynamic Polymer Systems with Self-Regulated Secretion for the Control of Surface Properties and Material Healing. *Nat. Mater.* **2015**, *14*, 790–795.

(42) Zhao, H.; Xu, J.; Jing, G.; Prieto-López, L. O.; Deng, X.; Cui, J. Controlling the Localization of Liquid Droplets in Polymer Matrices by Evaporative Lithography. *Angew. Chemie Int. Ed.* **2016**, *55* (36), 10681–10685.

(43) Phan, N.; Moronuki, N. Combination of Silicon Microstructures and Porous Cellulose Nanofiber Structures to Improve Liquid-Infused-Type Self-Cleaning Function. *Precis. Eng.* **2018**, *51* (November 2017), 638–646.

(44) Zhang, C.; Xia, Y.; Zhang, H.; Zacharia, N. S. Surface Functionalization for a Nontextured Liquid-Infused Surface with Enhanced Lifetime. *ACS Appl. Mater. Interfaces* **2018**, *10* (6), 5892–5901.

(45) Sotiri, I.; Tajik, A.; Lai, Y.; Zhang, C. T.; Kovalenko, Y.; Nemr, C. R.; Ledoux, H.; Alvarenga, J.; Johnson, E.; Patanwala, H. S.; et al. Tunability of Liquid-Infused Silicone Materials for Biointerfaces. *Biointerphases* **2018**, *13* (6), 1–14.

(46) Kratochvil, M. J.; Welsh, M. A.; Manna, U.; Ortiz, B. J.; Blackwell, H. E.; Lynn, D. M. Slippery Liquid-Infused Porous Surfaces That Prevent Bacterial Surface Fouling and Inhibit Virulence Phenotypes in Surrounding Planktonic Cells. *ACS Infect. Dis.* **2016**, *2* (7), 509–517.

(47) Manna, Uttam; Raman, Namrata; Welsh, Michael A.; Zayas-Gonzalez, Yashira M.; Blackwell, Helen E.; Palecek, Sean P.; Lynn, D. M. Slippery Liquid-Infused Porous Surfaces That Prevent Microbial Surface Fouling and Kill Non-Adherent Pathogens in Surrounding Media: A Controlled Release Approach. *Adv Funct Mater.* **2016**, *26* (21), 3599–3611.

(48) Goudie, M. J.; Pant, J.; Handa, H. Liquid-Infused Nitric Oxide-Releasing (LINORel) Silicone for Decreased Fouling, Thrombosis, and Infection of Medical Devices. *Sci. Rep.* **2017**, *7* (1), 1–13.

(49) Wooh, S.; Butt, H.-J. A Photocatalytically Active Lubricant-Impregnated Surface. *Angew. Chem. Int. Ed. Engl.* **2017**, *56*, 4965–4969.

(50) Almeida, A. V; Manz, A.; Neuzil, P. Pyrosequencing on a Glass Surface. *Lab Chip* **2016**, *16*, 1063–1071.

(51) Li, X.; Wu, W.; Manz, A. Thermal Gradient for Fluorometric Optimization of Droplet PCR in Virtual Reaction Chambers. *Microchim Acta* **2017**, *184*, 3433–3439.

(52) Park, K. C.; Kim, P.; Grinthal, A.; He, N.; Fox, D.; Weaver, J. C.; Aizenberg, J. Condensation on Slippery Asymmetric Bumps. *Nature* **2016**, *531* (7592), 78–82.

(53) Ahn, J.; Jeon, J.; Heu, C. S.; Kim, D. R. Three-Dimensionally Programmed Slippery Wrinkles with High Stretchability for Tunable Functionality of Icephobicity and Effective Water Harvesting. *Adv. Mater. Interfaces* **2018**, *1800980*, 1–7.

(54) Liu, C.; Ding, H.; Wu, Z.; Gao, B.; Fu, F.; Shang, L.; Gu, Z.; Zhao, Y. Tunable Structural Color Surfaces with Visually Self-Reporting Wettability. *Adv. Funct. Mater.* **2016**, *26* (43), 7937–7942.

(55) Zheng, Y.; Cheng, J.; Zhou, C.; Xing, H.; Wen, X.; Pi, P.; Xu, S. Droplet Motion on a Shape Gradient Surface. *Langmuir* **2017**, *33* (17), 4172–4177.

(56) Guan, J. H.; Ruiz-Gutiérrez, É.; Xu, B. Bin; Wood, D.; McHale, G.; Ledesma-Aguilar, R.; Wells, G. G. Drop Transport and Positioning on Lubricant-Impregnated Surfaces. *Soft Matter* **2017**, *13* (18), 3404–3410.

(57) You, I.; Lee, T. G.; Nam, Y. S.; Lee, H. Fabrication of a Micro-Omnifluidic Device by Omniphilic / Omniphobic Patterning on Nanostructured Surfaces. *ACS Nano* **2014**, *8* (9), 9016–9024.

(58) Chen, X.; Ren, K.; Wang, J.; Lei, W.; Ji, J. Infusing Lubricant onto Erasable Microstructured Surfaces toward Guided Sliding of Liquid Droplets. *ACS Appl. Mater. Interfaces* **2017**, acsami.6b14081.

(59) Yu, C.; Zhu, X.; Li, K.; Cao, M.; Jiang, L. Manipulating Bubbles in Aqueous Environment via a Lubricant-Infused Slippery Surface. *Adv. Funct. Mater.* **2017**, *27* (29), 1–7.

(60) Wang, Y.; Ma, K.; Xin, J. H. Stimuli-Responsive Bioinspired Materials for Controllable Liquid Manipulation: Principles, Fabrication, and Applications. *Adv. Funct. Mater.* **2018**, *28* (6), 1–28.

(61) Daniel, D.; Mankin, M. N.; Belisle, R. a.; Wong, T.-S.; Aizenberg, J. Lubricant-Infused Micro/Nano-Structured Surfaces with Tunable Dynamic Omniphobicity at High Temperatures. *Appl. Phys. Lett.* **2013**, *102* (23), 231603.

(62) Bjelobrk, N.; Girard, H. L.; Subramanyam, S. B.; Kwon, H. M.; Quéré, D.; Varanasi, K. K. Thermocapillary Motion on Lubricant-Impregnated Surfaces. *Phys. Rev. Fluids* **2016**, *1* (6), 1–7.

(63) Manabe, K.; Matsubayashi, T.; Tenjimbayashi, M.; Moriya, T.; Tsuge, Y.; Kyung, K. H.; Shiratori, S. Controllable Broadband Optical Transparency and Wettability Switching of Temperature-Activated Solid/Liquid-Infused Nanofibrous Membranes. *ACS Nano* **2016**, *10* (10), 9387–9396.

(64) Wang, L.; Heng, L.; Jiang, L. Temperature Responsive Anisotropic Slippery Surface for Smart Control of Droplet Motion. *ACS Appl. Mater. interfaces Interfaces* **2018**, *10*, 7442–7450.

(65) Gao, C.; Wang, L.; Lin, Y.; Li, J.; Liu, Y.; Li, X.; Feng, S.; Zheng, Y. Droplets Manipulated on Photothermal Organogel Surfaces. *Adv. Funct. Mater.* **2018**, *1803072*, 1–7.

(66) Che, P.; Heng, L.; Jiang, L. Lubricant-Infused Anisotropic Porous Surface Design of Reduced Graphene Oxide Toward Electrically Driven Smart Control of Conductive Droplets' Motion. *Adv. Funct. Mater.* **2017**, *27* (22), 1–9.

(67) He, X.; Qiang, W.; Du, C.; Shao, Q.; Zhang, X.; Deng, Y. Modification of Lubricant Infused Porous Surface for Low-Voltage Reversible Electrowetting. *J. Mater. Chem. A* **2017**, *5* (36), 19159–19167.

(68) Oh, I.; Keplinger, C.; Cui, J.; Chen, J.; Whitesides, G. M.; Aizenberg, J.; Hu, Y. Dynamically Actuated Liquid-Infused Poroelastic Film with Precise Control over Droplet Dynamics. *Adv. Funct. Mater.* **2018**, *1802632*, 1–9.

(69) Brabcova, Z.; McHale, G.; Wells, G. G.; Brown, C. V.; Newton, M. I. Electric Field Induced Reversible Spreading of Droplets into Films on Lubricant Impregnated Surfaces. *Appl. Phys. Lett.* **2017**, *110* (12), 121603.

(70) Ng, A. H. C.; Fobel, R.; Fobel, C.; Lamanna, J.; Rackus, D. G.; Summers, A.; Dixon, C.; Dryden, M. D. M.; Lam, C.; Ho, M.; et al. A Digital Microfluidic System for Serological Immunoassays in Remote Settings. *Sci. Transl. Med.* **2018**, *10*, 1–12.

(71) Luo, J. T.; Geraldi, N. R.; Guan, J. H.; McHale, G.; Wells, G. G.; Fu, Y. Q. Slippery Liquid-Infused Porous Surfaces and Droplet Transportation by Surface Acoustic Waves. *Phys. Rev. Appl.* **2017**, *7* (1), 1–9.

(72) Song, Y.; Li, M.; Pan, X.; Wang, Q.; Li, D. Size-Based Cell Sorting with a Resistive Pulse Sensor and an Electromagnetic Pump in a Microfluidic Chip. *Electrophoresis* **2015**, *36* (3), 398–404.

(73) Khalil, K. S.; Mahmoudi, S. R.; Abu-Dheir, N.; Varanasi, K. K. Active Surfaces: Ferrofluid-Impregnated Surfaces for Active Manipulation of Droplets. *Appl. Phys. Lett.* **2014**, *105* (4).

(74) Wang, W.; Timonen, J. V. I.; Carlson, A.; Drotlef, D. M.; Zhang, C. T.; Kolle, S.; Grinthal, A.; Wong, T. S.; Hatton, B.; Kang, S. H.; et al. Multifunctional Ferrofluid-Infused Surfaces with Reconfigurable Multiscale Topography. *Nature* **2018**, *559* (7712), 77–82.

(75) Rigoni, C.; Ferraro, D.; Carlassara, M.; Filippi, D.; Varagnolo, S.; Pierno, M.; Talbot, D.; Abou-Hassan, A.; Mistura, G. Dynamics of Ferrofluid Drops on Magnetically Patterned Surfaces. *Langmuir* **2018**, *34* (30), 8917–8922.

(76) Yang, S.; Dai, X.; Stogin, B. B.; Wong, T.-S. Ultrasensitive Surface-Enhanced Raman Scattering Detection in Common Fluids. *Proc. Natl. Acad. Sci.* **2016**, *113* (2), 268–273. https://doi.org/10.1073/pnas.1518980113.

(77) Boreyko, J. B.; Polizos, G.; Datskos, P. G.; Sarles, S. A.; Collier, C. P. Air-Stable Droplet Interface Bilayers on Oil-Infused Surfaces. *Proc. Natl. Acad. Sci.* **2014**, *111* (21), 7588–7593.

(78) Paulssen, D.; Feng, W.; Pini, I.; Levkin, P. A. Formation of Liquid-Liquid Micropatterns through Guided Liquid Displacement on Liquid-Infused Surfaces. *Adv. Mater. Interfaces* **2018**, *1800852*, 1–8.

(79) Bruchmann, J.; Pini, I.; Gill, T. S.; Schwartz, T.; Levkin, P. A. Patterned SLIPS for the Formation of Arrays of Biofilm Microclusters with Defined Geometries. *Adv. Healthc. Mater.* **2017**, *1601082*, 1–9.

(80) Twine, N. B.; Norton, R. M.; Brothers, M. C.; Hauke, A.; Gomez, E. F.; Heikenfeld, J. Open Nanofluidic Films with Rapid Transport and No Analyte Exchange for Ultra-Low Sample Volumes. *Lab Chip* **2018**, *00* (1), 1–11.

(81) Glavan, A. C.; Martinez, R. V.; Maxwell, E. J.; Subramaniam, A. B.; Nunes, R. M. D.; Soh, S.; Whitesides, G. M. Rapid Fabrication of Pressure-Driven Open-Channel Microfluidic Devices in Omniphobic RFpaper. *Lab Chip* **2013**, *13* (15), 2922–2930.

(82) Pal, A.; Cuellar, H. E.; Kuang, R.; Caurin, H. F. N.; Goswami, D.; Martinez, R. V. Self-Powered, Paper-Based Electrochemical Devices for Sensitive Point-of-Care Testing. *Adv. Mater. Technol.* **2017**, *2* (10), 1–10.

(83) Pal, A.; Goswami, D.; Cuellar, H. E.; Castro, B.; Kuang, S.; Martinez, R. V. Early Detection and Monitoring of Chronic Wounds Using Low-Cost, Omniphobic Paper-Based Smart Bandages. *Biosens. Bioelectron.* **2018**, *117* (June), 696–705.

(84) Chung, D. C. K.; Huynh, S. H.; Ahmad Zahidi, A. A.; Liew, O. W.; Ng, T. W. Simultaneous Multidrop Creation with Superhydrophobic Wells for Field Environmental Sensing of Nanoparticles. *ACS Omega* **2018**, *3* (8), 9310–9317.

(85) Cate, D. M.; Adkins, J. A.; Mettakoonpitak, J.; Henry, C. S. Recent Developments in Paper-Based Microfluidic Devices. *Anal. Chem.* **2015**, *87*, 19–41.

(86) Akyazi, T.; Basabe-Desmonts, L.; Benito-Lopez, F. Review on Microfluidic Paper-Based Analytical Devices towards Commercialisation. *Anal. Chim. Acta* **2018**, *1001*, 1–17.

(87) Martinez, A. W.; Phillips, S. T.; Whitesides, G. M.; Carrilho, E. Diagnostics for the Developing World: Microfluidic Paper-Based Analytical Devices. *Anal. Chem.* **2010**, *82* (1), 3–10.

(88) Martinez, A. W.; Phillips, S. T.; Whitesides, G. M. Three-Dimensional Microfluidic Devices Fabricated in Layered Paper and Tape. *Proc. Natl. Acad. Sci. U. S. A.* **2008**, *105* (50), 19606–19611.

(89) Xu, B.; Du, Y.; Lin, J.; Qi, M.; Shu, B.; Wen, X.; Liang, G.; Chen, B.; Liu, D. Simultaneous Identification and Antimicrobial Susceptibility Testing of Multiple Uropathogens on a Microfluidic Chip with Paper- Supported Cell Culture Arrays. *Anal. Chem.* **2016**, No. 88, 11593–11600.

(90) Güder, F.; Ainla, A.; Redston, J.; Mosadegh, B.; Glavan, A.; Martin, T. J.; Whitesides, G. M. Paper-Based Electrical Respiration Sensor. *Angew. Chemie Int. Ed.* **2016**, *55*, 5727–5732.

(91) Li, X.; Ballerini, D. R.; Shen, W. A Perspective on Paper-Based Microfluidics: Current Status and Future Trends. *Biomicrofluidics* **2012**, *6* (011301), 1–13.

(92) Maxwell, E. J.; Mazzeo, A. D.; Whitesides, G. M. Paper-Based Electroanalytical Devices for Accessible Diagnostic Testing. *MRS Bull.* **2013**, *38*, 309–314.

(93) Oh, J.-M.; Chow, K.-F. Recent Developments in Electrochemical Paper-Based Analytical Devices. *Anal. Methods* **2015**, *7*, 7951–7960.

(94) Mahato, K.; Srivastava, A.; Chandra, P. Paper Based Diagnostics for Personalized Health Care: Emerging Technologies and Commercial Aspects. *Biosens. Bioelectron.* **2017**, *96*, 246–259.

(95) Choi, G.; Choi, S. Cellular Flow in Paper-Based Microfluidics. *Sensors Actuators B Chem.* **2016**, *237*, 1021–1026.

(96) Sunny, S.; Cheng, G.; Daniel, D.; Lo, P.; Ochoa, S.; Howell, C.; Vogel, N.; Majid, A.; Aizenberg, J. Transparent Antifouling Material for Improved Operative Field Visibility in Endoscopy. *Proc. Natl. Acad. Sci.* **2016**, *113* (42), 11676–11681.

(97) Zhang, D.; Xia, Y.; Chen, X.; Shi, S.; Lei, L. PDMS Infused Poly (High Internal Phase Emulsion) Template for the Construction of Slippery Liquid-Infused Porous Surface with Self-Cleaning and Self-Repairing Properties. *Langmuir* **2019**, *35*, 8276–8284.

(98) Yao, X.; Dunn, S. S.; Kim, P.; Duffy, M.; Alvarenga, J.; Aizenberg, J. Fluorogel Elastomers with Tunable Transparency, Elasticity, Shape-Memory, and Antifouling Properties. *Angew. Chem. Int. Ed. Engl.* **2014**, *53*, 4418–4422.

(99) MacCallum, N.; Howell, C.; Kim, P.; Sun, D.; Friedlander, R.; Ranisau, J.; Ahanotu, O.; Lin, J. J.; Vena, A.; Hatton, B.; et al. Liquid-Infused Silicone As a Biofouling-Free Medical Material. *ACS Biomater. Sci. Eng.* **2014**, *1*, 43–51.

(100) Yeong, Y. H.; Wang, C.; Wynne, K. J.; Gupta, M. C. Oil-Infused Superhydrophobic Silicone Material for Low Ice Adhesion with Long-Term Infusion Stability. *ACS Appl. Mater. Interfaces* **2016**, *8*, 32050–32059.

(101) Damle, V. G.; Tummala, A.; Chandrashekar, S.; Kido, C.; Roopesh, A.; Sun, X.; Doudrick, K.; Chinn, J.; Lee, J. R.; Burgin, T. P.; et al. "Insensitive" to Touch: Fabric-Supported Lubricant-Swollen Polymeric Films for Omniphobic Personal Protective Gear. *ACS Appl. Mater. Interfaces* **2015**, *7* (7), 4224–4232.

(102) Stalder, A. F.; Melchior, T.; Müller, M.; Sage, D.; Blu, T.; Unser, M. Low-Bond Axisymmetric Drop Shape Analysis for Surface Tension and Contact Angle Measurements of Sessile Drops. *Colloids Surfaces A Physicochem. Eng. Asp.* **2010**, *364*, 72–81.

(103) Kim, P.; Kreder, M. J.; Alvarenga, J.; Aizenberg, J. Hierarchical or Not? Effect of the Length Scale and Hierarchy of the Surface Roughness on Omniphobicity of Lubricant-Infused Substrates. *Nano Lett.* **2013**, *13*, 1793–1799.

(104) Zhang, J.; Wang, A.; Seeger, S. Nepenthes Pitcher Inspired Anti-Wetting Silicone Nanofi Laments Coatings: Preparation, Unique Anti-Wetting and Self-Cleaning Behaviors. *Adv. Funct. Mater.* **2014**, *24*, 1074–1080.

(105) Glavan, A. C.; Martinez, R. V.; Subramaniam, A. B.; Yoon, H. J.; Nunes, R. M. D.; Lange, H.; Thuo, M. M.; Whitesides, G. M. Omniphobic "R F Paper" Produced by Silanization of Paper with Fluoroalkyltrichlorosilanes. *Adv. Funct. Mater.* **2014**, *24*, 60–70.

(106) Regan, D. P.; Howell, C. Droplet Manipulation with Bioinspired Liquid-Infused Surfaces: A Review of Recent Progress and Potential for Integrated Detection. *Curr. Opin. Colloid Interface Sci.* **2019**, *39*, 137–147. https://doi.org/10.1016/j.cocis.2019.01.012.

(107) Paulssen, D.; Hardt, S.; Levkin, P. A. Droplet Sorting and Manipulation on Patterned Two-Phase Slippery Lubricant-Infused Surface. *ACS Appl. Mater. Interfaces* **2019**, *11*, 16130–16138.

(108) Centers for Disease Control and Prevention. *Antibiotic Resistance Threats in the United States*; 2013.

(109) Fournier, P.-E.; Drancourt, M.; Colson, P.; Rolain, J.-M.; La Scola, B.; Raoult, D. Modern Clinical Microbiology: New Challenges and Solutions. *Nat. Rev. Microbiol.* **2013**, *11*, 574–585.

(110) Murray, C. K.; Wilkins, K.; Molter, N. C.; Li, F.; Yu, L.; Spott, M. A.; Eastridge, B.; Blackbourne, L. H.; Hospenthal, D. R. Infections Complicating the Care of Combat Casualties During Operations Iraqi Freedom and Enduring Freedom. *J. Trauma Inj. Infect. Crit. Care* **2011**, *71*, S62–S73.

(111) Mattner, F.; Bange, F.; Meyer, E.; Seifert, H.; Wichelhaus, T. A.; Chaberny, I. F. Preventing the Spread of Multidrug-Resistant Gram-Negative Pathogens. *Dtsch. Arztebl. Int.* **2012**, *109* (3), 39–45.

(112) Gordon, V. D.; Davis-Fields, M.; Kovach, K.; Rodesney, C. A. Biofilms and Mechanics: A Review of Experimental Techniques and Findings. *J. Phys. D. Appl. Phys.* **2017**, *50* (223002), 1–12.

(113) Katsikogianni, M.; Missirlis, Y. F. Concise Review of Mechanisms of Bacterial Adhesion to Biomaterials and of Techniques Used in Estimating Bacteria-Material Interactions. *Eur. Cell. Mater.* **2004**, *8*, 37–57.

(114) Sun, M.; Bai, R.; Yang, X.; Song, J.; Qin, M.; Suo, Z.; He, X. Hydrogel Interferometry for Ultrasensitive and Highly Selective Chemical Detection. *Adv. Mater.* **2018**, *1804916*.

(115) Qin, M.; Sun, M.; Hua, M.; He, X. Bioinspired Structural Color Sensors Based on Responsive Soft Materials. *Curr. Opin. Solid State Mater. Sci.* **2018**.

(116) World Health Organization. *Managing Epidemics: Key Facts about Major Deadly Diseases*; Geneva, 2018.

(117) Saulnier, D. D.; Ribacke, K. B.; Schreeb, J. Von. No Calm After the Storm : A Systematic Review of Human Health Following Flood and Storm Disasters. *Prehosp. Disaster Med.* **2017**, *32* (5), 568–579.

(118) Culver, A.; Rochat, R.; Cookson, S. T. Public Health Implications of Complex Emergencies and Natural Disasters. *Confl. Health* **2017**, *11* (32), 1–7.

(119) Gao, A.; Liu, J.; Ye, L.; Schönecker, C.; Kappl, M.; Butt, H. J.; Steffen, W. Control of Droplet Evaporation on Oil-Coated Surfaces for the Synthesis of Asymmetric Supraparticles. *Langmuir* **2019**, *35* (43), 14042–14048.

(120) McBride, S. A.; Dash, S.; Varanasi, K. K. Evaporative Crystallization in Drops on Superhydrophobic and Liquid-Impregnated Surfaces. *Langmuir* **2018**, *34* (41), 12350–12358.

(121) Hu, J.; Wang, S.; Wang, L.; Li, F.; Pingguan-Murphy, B.; Jian, T.; Xu, F. Biosensors and Bioelectronics Advances in Paper-Based Point-of-Care Diagnostics. *Biosens. Bioelectron.* **2014**, *54*, 585–597.

(122) Glover, J.; Hewett, J.; Bernhards, R. C.; Mach, P.; Rivers, B.; Widder, M.; Curtis, T.; Cazares, L.; Brennan, L.; Lewis, J.; et al. *STATE OF THE ART REPORT: Methods for Investigating Chemical/Biological Weapons Use*; Washington D.C., 2018.

(123) Ducrée, J.; Haeberle, S.; Lutz, S.; Pausch, S.; von Stetten, F.; Zengerle, R. The Centrifugal Microfluidic Bio-Disk Platform. *J. Micromechanics Microengineering* **2007**, *17*, S103–S115.

(124) Garrett, T. R.; Bhakoo, M.; Zhang, Z. Bacterial Adhesion and Biofilms on Surfaces. *Progress in Natural Science*. 2008. https://doi.org/10.1016/j.pnsc.2008.04.001.

(125) Ramírez-Castillo, F. Y.; Loera-Muro, A.; Jacques, M.; Garneau, P.; Avelar-González, F. J.; Harel, J.; Guerrero-Barrera, A. L. Waterborne Pathogens: Detection Methods and Challenges. *Pathogens* **2015**, *4*, 307–334.

(126) Deshmukh, R. A.; Joshi, K.; Bhand, S.; Roy, U. Recent Developments in Detection and Enumeration of Waterborne Bacteria : A Retrospective Minireview. *Microbiologyopen* **2016**, *5* (6), 901–922.

(127) Fleury, B.; Kelley, W. L.; Lew, D.; Götz, F.; Proctor, R. A.; Vaudaux, P. Transcriptomic and Metabolic Responses of Staphylococcus Aureus Exposed to Supra-Physiological Temperatures. *BMC Microbiol.* **2009**, *9* (76), 1–12.

(128) Murata, M.; Fujimoto, H.; Nishimura, K.; Charoensuk, K.; Nagamitsu, H.; Raina, S.; Kosaka, T.; Oshima, T.; Ogasawara, N.; Yamada, M. Molecular Strategy for Survival at a Critical High Temperature in Eschierichia Coli. *PLoS One* **2011**, *6* (6), 1–9.

(129) Li, J.; Kleintschek, T.; Rieder, A.; Cheng, Y.; Baumbach, T.; Obst, U.; Schwartz, T.; Levkin, P. A. Hydrophobic Liquid-Infused Porous Polymer Surfaces for Antibacterial Applications. *ACS Appl. Mater. Interfaces* **2013**, *5*, 6704–6711.

(130) Petersen, E.; Koopmans, M.; Go, U.; Hamer, D. H.; Petrosillo, N.; Castelli, F.; Storgaard, M.; Al Khalili, S.; Simonsen, L. Comparing SARS-CoV-2 with SARS-CoV and Influenza Pandemics. *Lancet Infect. Dis.* **2020**, *20* (9), e238–e244.

(131) Nasir, Z. A.; Campos, L. C.; Christie, N.; Colbeck, I. Airborne Biological Hazards and Urban Transport Infrastructure: Current Challenges and Future Directions. *Environ. Sci. Pollut. Res.* **2016**, *23* (15), 15757–15766.

(132) Herfst, S.; Böhringer, M.; Karo, B.; Lawrence, P.; Lewis, N. S.; Mina, M. J.; Russell, C. J.; Steel, J.; de Swart, R. L.; Menge, C. Drivers of Airborne Human-to-Human Pathogen Transmission. *Curr. Opin. Virol.* **2017**, *22*, 22–29.

(133) Després, V. R.; Alex Huffman, J.; Burrows, S. M.; Hoose, C.; Safatov, A. S.; Buryak, G.; Fröhlich-Nowoisky, J.; Elbert, W.; Andreae, M. O.; Pöschl, U.; et al. Primary Biological Aerosol Particles in the Atmosphere: A Review. *Tellus, Ser. B Chem. Phys. Meteorol.* **2012**, *64* (1).

(134) Tellier, R.; Li, Y.; Cowling, B. J.; Tang, J. W. Recognition of Aerosol Transmission of Infectious Agents: A Commentary. *BMC Infect. Dis.* **2019**, *19* (1), 1–9.

(135) Lai, K. M.; Emberlin, J.; Colbeck, I. Outdoor Environments and Human Pathogens in Air. *Environ. Heal. A Glob. Access Sci. Source* **2009**, *8* (SUPPL. 1), 1–5.

(136) Taylor, P. W. Impact of Space Flight on Bacterial Virulence and Antibiotic Susceptibility. *Infect. Drug Resist.* **2015**, *8*, 249–262.

(137) Haines, S. R.; Bope, A.; Horack, J. M.; Meyer, M. E.; Dannemiller, K. C. Quantitative Evaluation of Bioaerosols in Different Particle Size Fractions in Dust Collected on the International Space Station (ISS). *Appl. Microbiol. Biotechnol.* **2019**, *103* (18), 7767–7782.

(138) Mangili, A.; Gendreau, M. A. Transmission of Infections during Commercial Air Travel [4]. *Lancet* **2005**, *365*, 989–996.

(139) Rogers, B. A.; Aminzadeh, Z.; Hayashi, Y.; Paterson, D. L. Country-to-Country Transfer of Patients and the Risk of Multi-Resistant Bacterial Infection. *Clin. Infect. Dis.* **2011**, *53*, 49–56.

(140) Saran, S.; Gurjar, M.; Baronia, A.; Sivapurapu, V.; Ghosh, P. S.; Raju, G. M.; Maurya, I. Heating, Ventilation and Air Conditioning (HVAC) in Intensive Care Unit. *Crit. Care* **2020**, *24* (1), 1–11.

(141) Lang, J. L.; Nursing, B. H1N1 09 Influenza —– An Aeromedical Perspective. *Australas. Emerg. Nurs. J.* **2010**, *13*, 53–60.

(142) Schulz-Stübner, S.; Henker, J.; Braun, J.; Kosa, R. Aerosol Distribution in the Cabin and Cockpit of an Ambulance Helicopter. *Infect. Control Hosp. Epidemiol.* **2020**, 1–2.

(143) Fujiyoshi, S.; Tanaka, D.; Maruyama, F. Transmission of Airborne Bacteria across Built Environments and Its Measurement Standards: A Review. *Front. Microbiol.* **2017**, *8* (NOV).

(144) NIOSH. Sampling and Characterization of Bioaerosols. *NIOSH Man. Anal. Methods* **2005**, No. 100, 4–7.

(145) Verreault, D.; Moineau, S.; Duchaine, C. Methods for Sampling of Airborne Viruses. *Microbiol. Mol. Biol. Rev.* **2008**, *72* (3), 413–444.

(146) Pan, M.; Lednicky, J. A.; Wu, C. Y. Collection, Particle Sizing and Detection of Airborne Viruses. *J. Appl. Microbiol.* **2019**, *127* (6), 1596–1611.

(147) Mainelis, G. Bioaerosol Sampling: Classical Approaches, Advances, and Perspectives. *Aerosol Sci. Technol.* **2020**, *54* (5), 496–519.

(148) Cox, J.; Mbareche, H.; Lindsley, W. G.; Duchaine, C. Field Sampling of Indoor Bioaerosols. *Aerosol Sci. Technol.* **2020**, *54* (5), 572–584.

(149) Fabian, P.; McDevitt, J. J.; Houseman, E. A.; Milton, D. K. Airborne Influenza Virus Detection with Four Aerosol Samplers Using Molecular and Infectivity Assays: Considerations for a New Infectious Virus Aerosol Sampler. *Indoor Air* **2009**, *19* (5), 433–441.

(150) Hou, X.; Hu, Y.; Grinthal, A.; Khan, M.; Aizenberg, J. Liquid-Based Gating Mechanism with Tunable Multiphase Selectivity and Antifouling Behaviour. *Nature* **2015**, *519* (7541), 70–73.

(151) Liu, W.; Wang, M.; Sheng, Z.; Zhang, Y.; Wang, S.; Qiao, L.; Hou, Y.; Zhang, M.; Chen, X.; Hou, X. Mobile Liquid Gating Membrane System for Smart Piston and Valve Applications. *Ind. Eng. Chem. Res.* **2019**, *58* (27), 11976–11984.

(152) Alvarenga, J.; Ainge, Y.; Williams, C.; Maltz, A.; Blough, T.; Khan, M.; Aizenberg, J. Research Update : Liquid Gated Membrane Filtration Performance with Inorganic Particle Suspensions. *APL Mater.* **2018**, *6* (100703), 1–10.

(153) Sheng, Z.; Wang, H.; Tang, Y.; Wang, M.; Huang, L.; Min, L.; Meng, H.; Chen, S.; Jiang, L.; Hou, X. Liquid Gating Elastomeric Porous System with Dynamically Controllable Gas/Liquid Transport. *Sci. Adv.* **2018**, *4* (2), 1–10.

(154) Bazyar, H.; Javadpour, S.; Lammertink, R. G. H. On the Gating Mechanism of Slippery Liquid Infused Porous Membranes. *Adv. Mater. Interfaces* **2016**, *3* (14), 3–8.

(155) Bazyar, H.; Lv, P.; Wood, J. A.; Porada, S.; Lohse, D.; Lammertink, R. G. H. Liquid-Liquid Displacement in Slippery Liquid-Infused Membranes (SLIMs). *Soft Matter* **2018**, *14* (10), 1780–1788.

(156) Bazyar, H.; Xu, L.; de Vries, H. J.; Porada, S.; Lammertink, R. Application of Liquid-Infused Membranes to Mitigate Biofouling. *Environ. Sci. Water Res. Technol.* **2020**.

(157) Zhao, L.; Li, R.; Xu, R.; Si, D.; Shang, Y.; Ye, H.; Zhang, Y.; Ye, H.; Xin, Q. Antifouling Slippery Liquid-Infused Membrane for Separation of Water-in-Oil Emulsions. *J. Memb. Sci.* **2020**, *611* (November 2019), 118289.

(158) Tesler, A. B.; Sheng, Z.; Lv, W.; Fan, Y.; Fricke, D.; Park, K.-C.; Alvarenga, J.; Aizenberg, J.; Hou, X. Metallic Liquid Gating Membranes. *ACS Nano* **2020**, *14*, 2465–2474.

(159) Jimmy, B.; Kentish, S.; Grieser, F.; Ashokkumar, M. Ultrasonic Nebulization in Aqueous Solutions and the Role of Interfacial Adsorption Dynamics in Surfactant Enrichment. *Langmuir* **2008**, *24* (18), 10133–10137.

(160) Regan, D. P.; Lilly, C.; Weigang, A.; White, L. R.; LeClair, E. J.; Collins, A.; Howell, C. Combining the Geometry of Folded Paper with Liquid-Infused Polymer Surfaces to Concentrate and Localize Bacterial Solutions. *Biointerphases* **2019**, *14* (4), 041005.

(161) Jiang, J.; Zhang, H.; He, W.; Li, T.; Li, H.; Liu, P.; Liu, M.; Wang, Z.; Wang, Z.; Yao, X. Adhesion of Microdroplets on Water-Repellent Surfaces toward the Prevention of Surface Fouling and Pathogen Spreading by Respiratory Droplets. *ACS Appl. Mater. Interfaces* **2017**, *9* (7), 6599–6608.

(162) Xie, X.; Li, Y.; Zhang, T.; Fang, H. H. P. Bacterial Survival in Evaporating Deposited Droplets on a Teflon-Coated Surface. *Appl. Microbiol. Biotechnol.* **2006**, *73* (3), 703–712.

(163) Mousavi, E. S.; Godri Pollitt, K. J.; Sherman, J.; Martinello, R. A. Performance Analysis of Portable HEPA Filters and Temporary Plastic Anterooms on the Spread of Surrogate Coronavirus. *Build. Environ.* **2020**, *183* (July), 107186.

(164) Butt, H.; Kappl, M. Normal Capillary Forces. *Adv. Colloid Interface Sci.* **2009**, *146*, 48–60.

(165) Alassod, A.; Xu, G. Comparative Study of Polypropylene Nonwoven on Structure and Wetting Characteristics. *J. Text. Inst.* **2020**.

(166) Sklodowska, K.; Jakiela, S. Enhancement of Bacterial Growth with the Help of Immiscible Oxygenated Oils. *RSC Adv.* **2017**, *7* (65), 40990–40995.

APPENDIX A

LIQUID-INFUSED POLYMER SURFACE CHARACTERIZATIONS

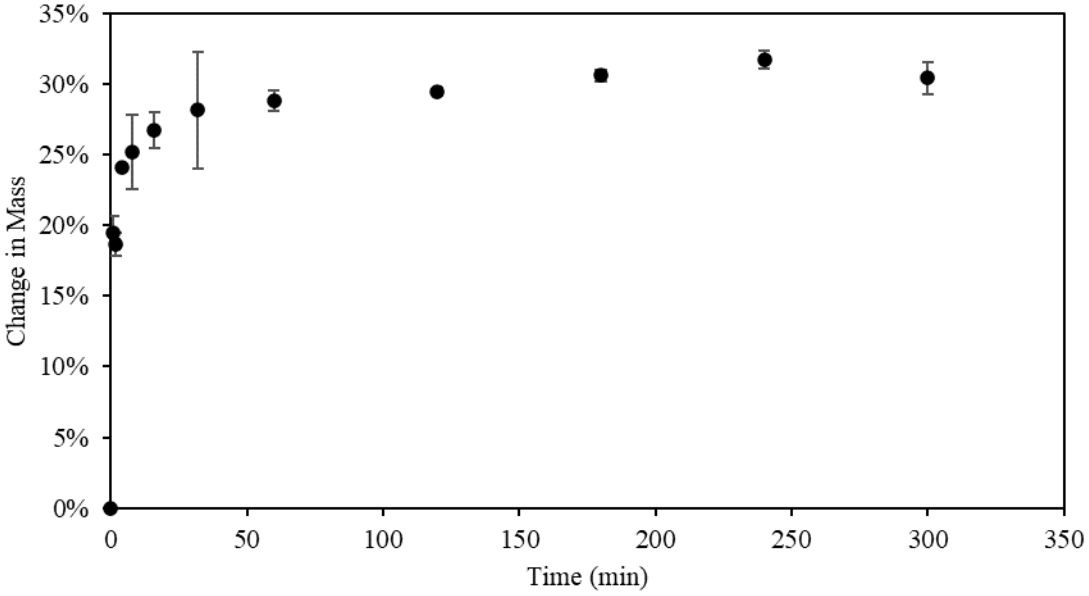

Figure A.1. Masses of SRP samples (1.5 x 4.0 cm) immersed in 10 cSt PDMS oil were recorded over time. The difference between the mass at each time point compared to the original mass of the SRP sample is plotted as the percent change in mass over time. Line of best fit shown by the dashed line, error bars represent standard deviation for n=3.

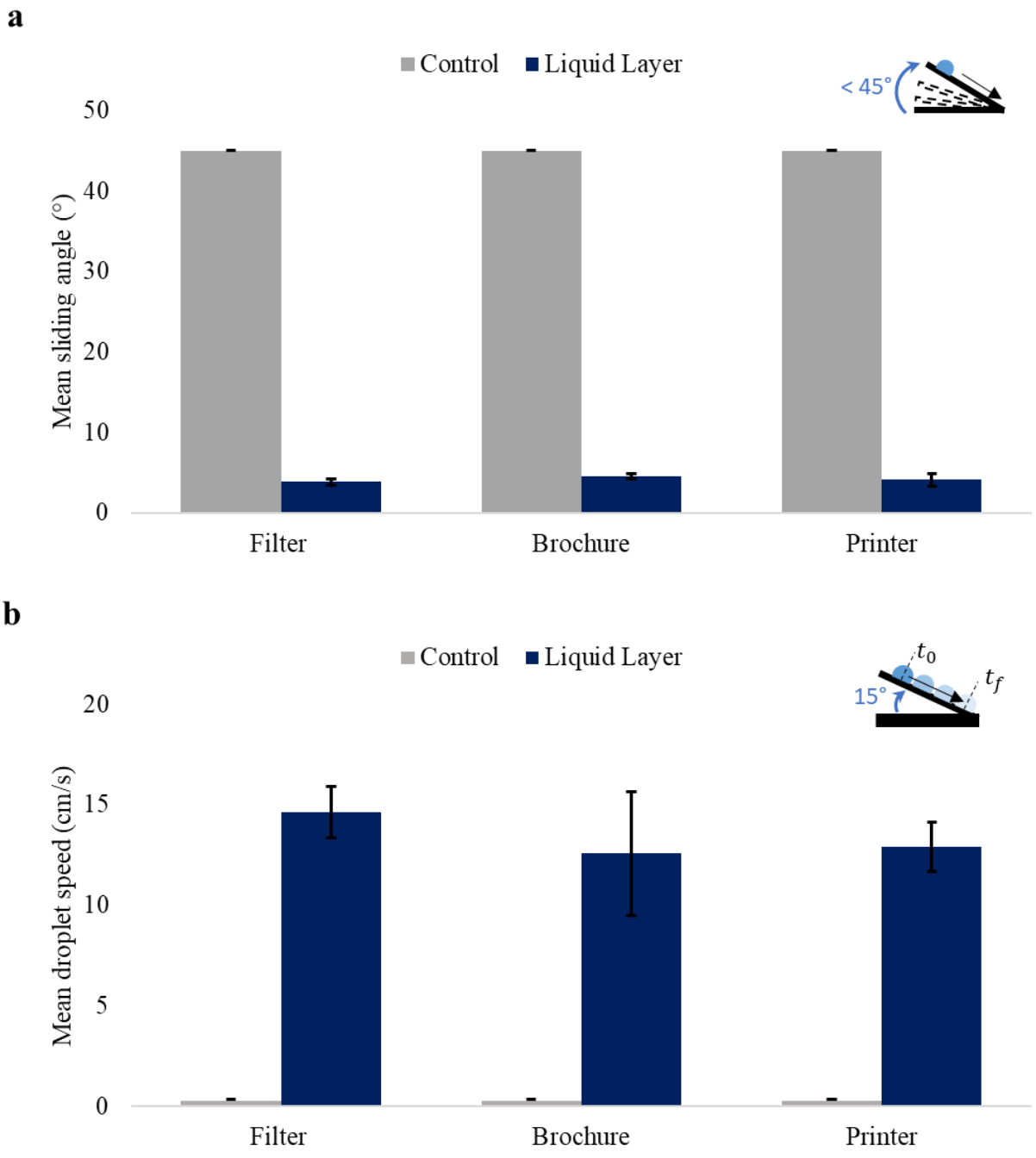

Figure A.2. (a) Droplet sliding angle and (b) droplet speed measurements plotted for filter, brochure, and printer paper. Dry control surfaces shown in gray and surfaces with a liquid layer shown in navy. Error bars represent standard deviation of three replicates on the same surface.

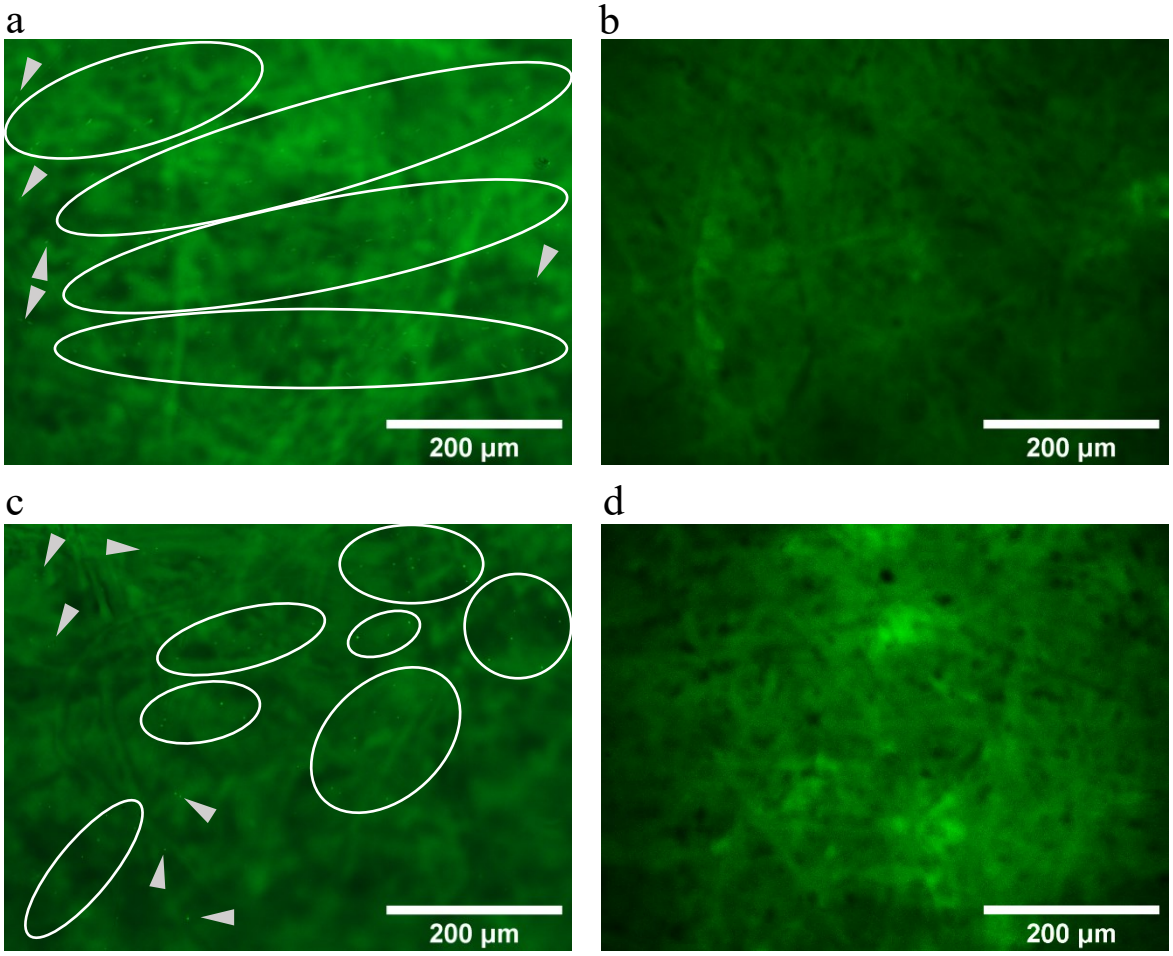

Figure A.3. (a) Image of a dry control SRP surface after a 50 µL droplet containing 10^8 CFU/mL of *E. coli* traveled the length of the surface. Arrows and circles indicate presence of bacteria on the surface. (b) Image from a z-stack conducted on the surface of the SRP surface with a liquid layer after the *E. coli* droplet retention test showing no green fluorescence from the bacteria. (c) Image of a dry control SRP surface after a 50 µL droplet containing 10^7 CFU/mL of *S. aureus* traveled the length of the surface. Arrows and circles indicate presence of bacteria on the surface. (d) Image from a z-stack conducted on the surface of the SRP surface with a liquid layer after the *S. aureus* droplet retention test showing no green fluorescence from the bacteria.

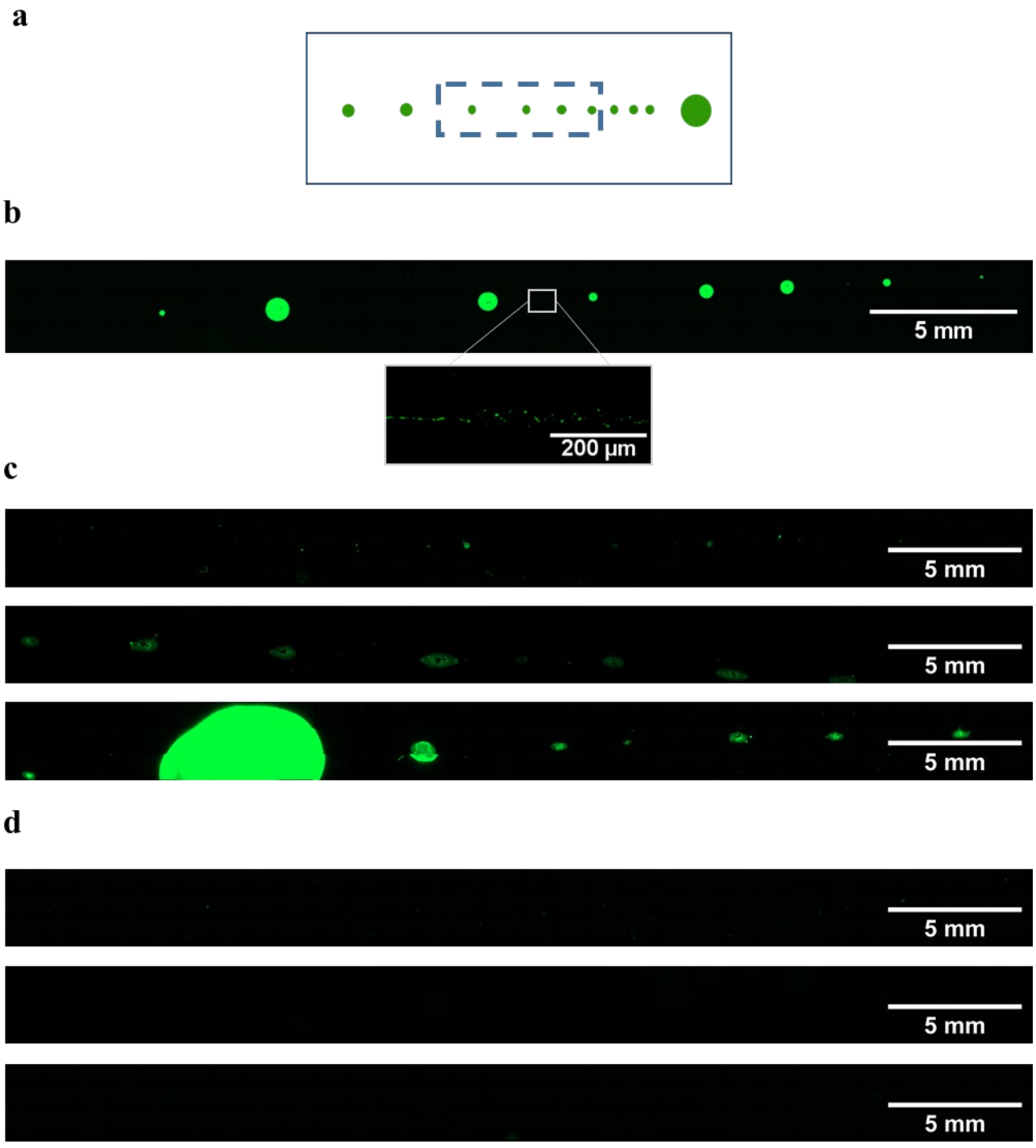

Figure A.4. (a) Schematic of the droplet's pathway on the PDMS surface, inset showing the area capture by the scans below. (b) Compiled fluorescence microscopy scan of a dry control PDMS surface after a droplet containing 10^8 CFU/mL of *E. coli* traveled across the surface with an inset showing a trail of individual bacterium between the large residual droplets. (c) Compiled scans of the *E. coli* droplet retention test on dry control PDMS surfaces (n=3). (d) Compiled scans of the *E. coli* droplet retention test on PDMS surfaces with a liquid layer (n=3).

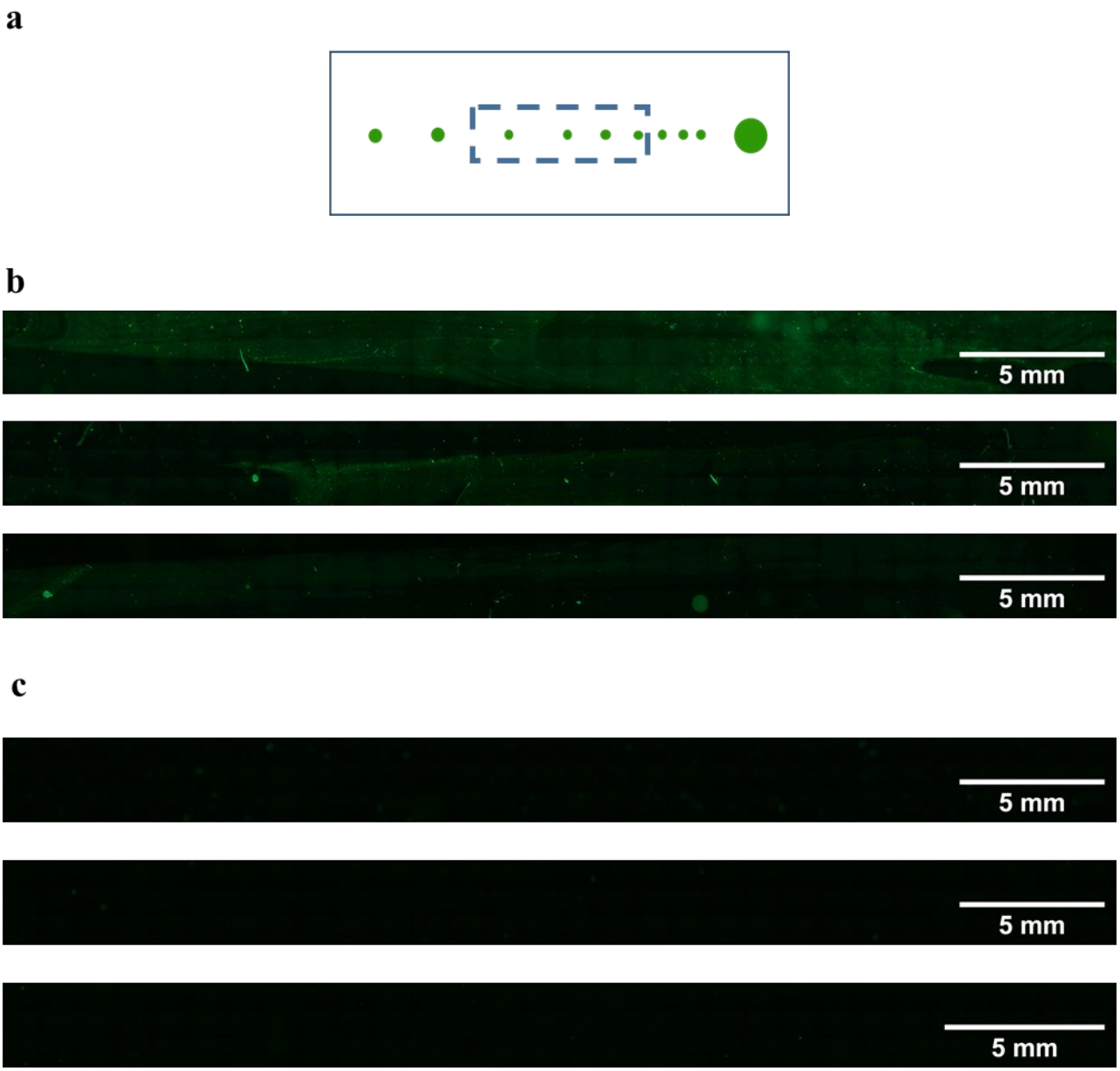

Figure A.5. (a) Schematic of the droplet's pathway on the PDMS surface, inset showing the area capture by the scans below. (b) Compiled fluorescence microscopy scan of a dry control PDMS surface after a droplet containing 10^7 CFU/mL of *S. aureus* (n=3). (c) Compiled scans of the *S. aureus* droplet retention test on PDMS surfaces with a liquid layer (n=3).

APPENDIX B

INVESTIGATION OF SRP CUPS' INFUSION LIQUID VISCOSITY

An experiment was constructed to investigate how varying the viscosity of the PDMS infusion oil would affect the rate of evaporation and potential patterns to localization. The 5 cm × 5 cm SRP cups were folded and prepared as discussed in Section 3.2.1. Three temperature ranges were explored, with a sample number of 2 (n =2) per infusion condition; for each temperature range there were SRP cups of the following viscosities: 1.5 cSt, 3 cSt, 7 cSt, 10 cSt, and the dry controls. Each cup was filled with 3 mL of dyed water (400 μL FD&C Blue #1 dye in 100 mL of water). The first set of SRP cups was placed in the -80 °C freezer. Every sample was frozen within 30 minutes and did not exhibit any changes amongst the conditions. The second set was placed in the Isotemp 60 L Oven (Thermo Fisher Scientific) at 70 °C and imaged at hour intervals of t = 0, 2, 4, 22, and 94 hours as seen in **Figure B.1**. At the four-hour observation, all of the liquid in the control and 1.5 cSt cups had evaporated, and the 3 cSt sample had been evaporated at the 22-hour mark. At the 94-hour observation, all oil had been evaporated from the 1.5 and 3 cSt cups, whereas the liquid samples had evaporated but oiled remained for the 7 and 10 cSt cups. The final set of SRP cups remained at in the ambient environment at room temperature. Observations were recorded at t = 0, 94, 144, 264, and 505 hours, as seen in **Figure B.2.** At the 94-hour mark, the liquid overlayer was gone from the 1.5 cSt samples. All liquid and oil had evaporated from the control through 3 cSt cups by the 264-hour mark, while one of the 7 cSt cups fell out of the study. At the final observation (505 hours), the liquid samples and oil remained for the 7 and 10 cSt samples. Original files were corrupted, but scans of the original data are provided below.

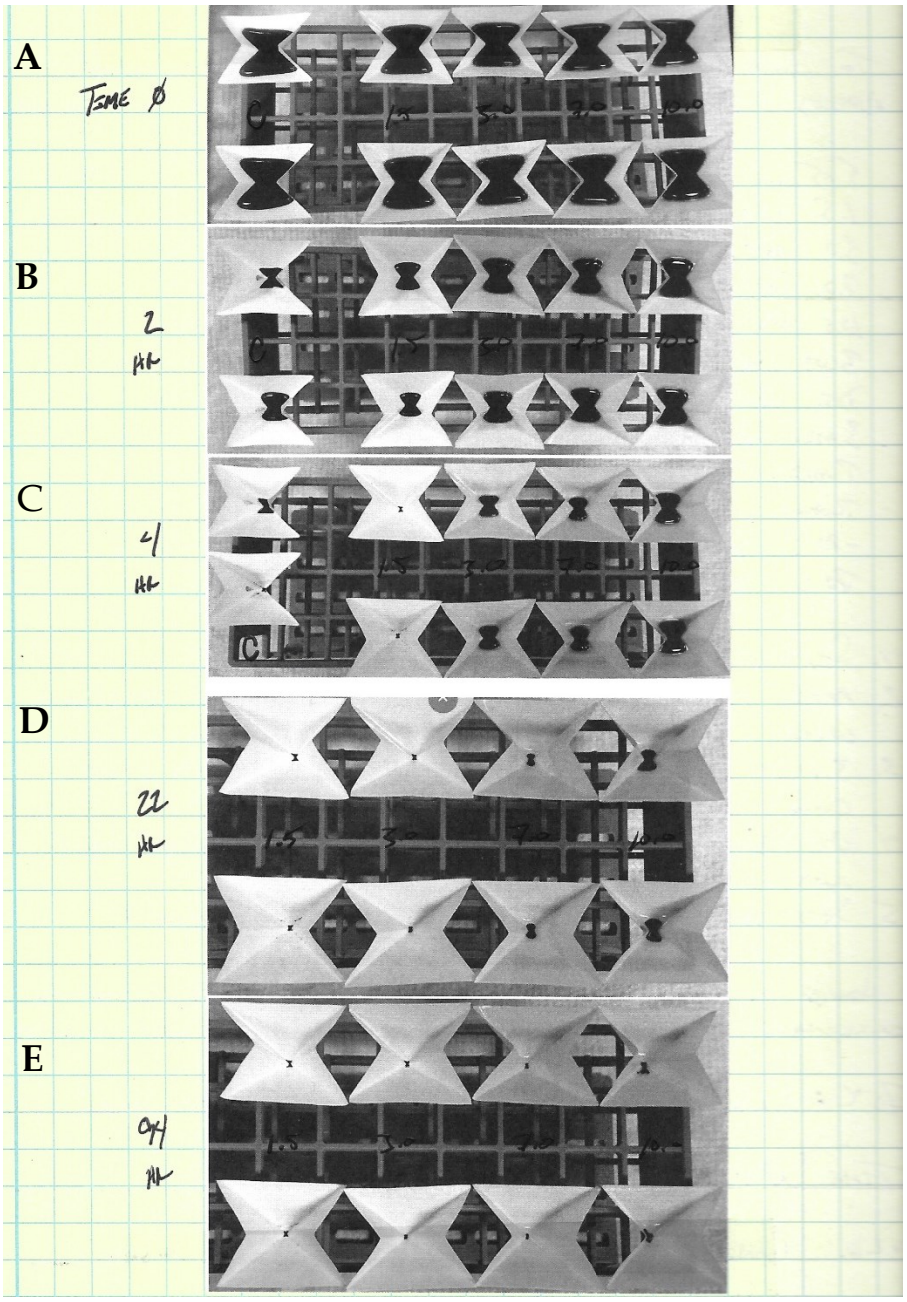

Figure B.1. Observation marks of SRP cups evaporating at 70 °C. SRP cups pictured in order, from left to right, are as follows, the control, 1.5 cSt, 3 cSt, 7 cSt, and 10 cSt, in duplicate for each photo. Controls are not pictured in Figure B.1D and Figure B.1E. A) Initial observation at t = 0 h. B) Second observation at t = 2 h. C) Third observation at t = 4 h, liquid has evaporated from the control and 1.5 cSt cups. D) Fourth observation at t = 22 h, liquid has evaporated from 3 cSt cups. E) Final observation at t = 94 h, liquid samples have evaporated from 7 and 10 cSt cups, but the PDMS oil remained.

Figure B.2. Observation of SRP at room temperature. SRP cups pictured in order, from left to right, are as follows, the control, 1.5 cSt, 3 cSt, 7 cSt, and 10 cSt, in duplicate for each photo. Observations are conducted at t= 0 h (A), t = 94 h (B), t = 144 h (C), t = 264 h (D), and t = 505 h (E). The second 7 cSt cup exited the study after 144 h. Liquid samples and oil remain for 7 and 10 cSt SRP cups at the final observation after 505 hours, while all other samples were evaporated.

APPENDIX C

BUBBLER SYSTEM PERFORMANCE DATA

Table C.1. Raw CFU Counts for 15-Minute Recovery

	Control	90 K103	90 K107	180 K103	180 K107
Data Set 1	0	37	52	0	52
	14	9	12	6	0
	0	65	2	0	43
Data Set 2	5	TNTC	15	5	4
	1	13	100	7	14
	18	11	35	2	33
	0	49	105	3	4
	0	1	156	0	17
	5	10	54	37	82
AVG	4.8	24.4	59.0	6.7	27.7
SD	6.4	21.5	48.6	11.0	25.8

Table C.2. Raw CFU Counts for 30-Minute Recovery

	Control	90 K103	90 K107	180 K103	180 K107
Data Set 1	0	49	34	1	7
	2	7	49	7	18
	3	16	98	0	10
Data Set 2	6	37	10	18	3
	2	11	94	3	0
	0	6	38	3	31
	0	67	43	3	0
	0	50	0	14	1
	0	50	142	7	22
AVG	1.4	32.6	56.4	6.2	10.2
SD	1.9	21.6	43.3	5.7	10.5

Table C.3. Normalized CFU Counts for 15-Minute Recovery

	Control	90 K103	90 K107	180 K103	180 K107
Data Set 1	0.0E+00	5.4E-04	7.6E-04	0.0E+00	7.6E-04
	2.1E-04	1.3E-04	1.8E-04	8.8E-05	0.0E+00
	0.0E+00	9.6E-04	2.9E-05	0.0E+00	6.3E-04
Data Set 2	6.6E-05	TNTC	2.0E-04	6.6E-05	5.3E-05
	1.3E-05	1.7E-04	1.3E-03	9.2E-05	1.8E-04
	2.4E-04	1.4E-04	4.6E-04	2.6E-05	4.3E-04
	0.0E+00	6.4E-04	1.4E-03	3.9E-05	5.3E-05
	0.0E+00	1.3E-05	2.1E-03	0.0E+00	2.2E-04
	6.6E-05	1.3E-04	7.1E-04	4.9E-04	1.1E-03

Table C.4. Normalized CFU Counts for 30-Minute Recovery

	Control	90 K103	90 K107	180 K103	180 K107
Data Set 1	0.0E+00	8.3E-04	5.8E-04	1.7E-05	1.2E-04
	3.4E-05	1.2E-04	8.3E-04	1.2E-04	3.1E-04
	5.1E-05	2.7E-04	1.7E-03	0.0E+00	1.7E-04
Data Set 2	4.7E-05	2.9E-04	7.8E-05	1.4E-04	2.3E-05
	1.6E-05	8.6E-05	7.3E-04	2.3E-05	0.0E+00
	0.0E+00	4.7E-05	3.0E-04	2.3E-05	2.4E-04
	0.0E+00	5.2E-04	3.4E-04	2.3E-05	0.0E+00
	0.0E+00	3.9E-04	0.0E+00	1.1E-04	7.8E-06
	0.0E+00	3.9E-04	1.1E-03	5.5E-05	1.7E-04

Table C.5. Normalized Counts ($\times 10^5$) Used for System Analysis

	Control	90 K103	90 K107	180 K103	180 K107
15-Min Avg	6.53	36.18	70.27	7.91	38.39
15-Min St. Dev.	8.75	28.47	60.30	13.27	32.11
30-Min Avg	1.79	33.27	64.62	5.53	11.95
30-Min St. Dev.	1.88	21.13	46.95	4.46	10.13

APPENDIX D

SYRINGE NEBULIZER SYSTEM PERFORMANCE DATA

Table D.1. Raw CFU Counts of First Run

	Filter 1	Filter 2	Filter 3
Control	0	0	0
90 K103	3	0	0
90 K107	1	0	2

Table D.2. Raw CFU Counts of Second Run

	Filter 1	Filter 2	Filter 3
Control	0	0	0
90 K103	0	0	1
90 K107	73	0	0

APPENDIX E

1.0 μM PTFE-LN DATA

Table E.1. Raw CFU Counts for 0-Minute Recovery

	Stamp 1	Stamp 2	Stamp 3	Stamp 4	Stamp 5	Stamp 6	Stamp 7	Stamp 8	Stamp 9	**Total**
80 K103 2	0	0	0	0	0	0	0	0	0	**0**
160 K103 1	11	4	3	1	0	0	0	0	0	**19**
80 K107 1	33	9	0	1	0	0	3	0	0	**46**
160 K107 1	12	7	1	0	2	0	0	0	0	**22**
C3	63	35	13	7	5	3	4	6	2	**138**
80 K103 3	49	18	1	3	1	2	0	0	1	**75**
80 K107 2	52	8	3	5	1	1	1	1	0	**72**
160 K107 2	21	6	5	2	0	0	0	1	1	**36**
160 K103 3	30	14	4	10	5	1	0	0	2	**66**
C1	62	20	13	4	5	1	0	1	0	**106**
80 K107 3	49	13	4	1	2	0	0	0	0	**69**
160 K103 2	48	16	17	2	4	2	1	0	0	**90**
80 K103 1	37	5	4	0	3	1	0	0	0	**50**
160 K107 3	42	8	8	0	3	2	0	0	0	**63**
C2	79	14	15	9	7	5	3	0	2	**134**

Table E.2. Rate of Release Calculations for 0-Minute Recovery

	Stamp 1	Stamp 2	Stamp 3	Stamp 4	Stamp 5	Stamp 6	Stamp 7	Stamp 8	Stamp 9
C3	1	0.5556	0.2063	0.1111	0.0794	0.0476	0.0635	0.0952	0.0317
C2	1	0.1772	0.1899	0.1139	0.0886	0.0633	0.0380	0.0000	0.0253
C1	1	0.3226	0.2097	0.0645	0.0806	0.0161	0.0000	0.0161	0.0000
80 K107 3	1	0.2653	0.0816	0.0204	0.0408	0.0000	0.0000	0.0000	0.0000
80 K107 2	1	0.1538	0.0577	0.0962	0.0192	0.0192	0.0192	0.0192	0.0000
80 K107 1	1	0.2727	0.0000	0.0303	0.0000	0.0000	0.0909	0.0000	0.0000
80 K103 3	1	0.3673	0.0204	0.0612	0.0204	0.0408	0.0000	0.0000	0.0204
80 K103 2	1	0.0000	0.0000	0.0000	0.0000	0.0000	0.0000	0.0000	0.0000
80 K103 1	1	0.1351	0.1081	0.0000	0.0811	0.0270	0.0000	0.0000	0.0000
160 K107 3	1	0.1905	0.1905	0.0000	0.0714	0.0476	0.0000	0.0000	0.0000
160 K107 2	1	0.2857	0.2381	0.0952	0.0000	0.0000	0.0000	0.0476	0.0476
160 K107 1	1	0.0000	0.0000	0.0000	0.0000	0.0000	0.0000	0.0000	0.0000
160 K103 3	1	0.4667	0.1333	0.3333	0.1667	0.0333	0.0000	0.0000	0.0667
160 K103 2	1	0.3333	0.3542	0.0417	0.0833	0.0417	0.0208	0.0000	0.0000
160 K103 1	1	0.3636	0.2727	0.0909	0.0000	0.0000	0.0000	0.0000	0.0000

Table E.3. Transferred CFUs for Stamp No. 1 of 0-Minute Recovery

	Avg	**Std Dev**
Control	68.0	7.8
80 K103	28.7	20.9
80 K107	44.7	8.3
160 K103	29.7	15.1
160 K107	25.0	12.6

Table E.4. Total CFUs Transferred of 0-Minute Recovery

	Avg	Std Dev
Control	126.0	14.2
80 K103	41.7	31.2
80 K107	62.3	11.6
160 K103	58.3	29.5
160 K107	40.3	17.0

Table E.5. Raw CFU Counts for 15-Minute Recovery

	Stamp 1	Stamp 2	Stamp 3	Stamp 4	Stamp 5	Stamp 6	Stamp 7	Stamp 8	Stamp 9	**Total**
80 K103 2	0	0	0	0	0	0	0	0	0	**0**
160 K103 1	0	0	0	0	0	0	0	0	0	**0**
80 K107 1	1	0	0	0	0	0	0	0	0	**1**
160 K107 1	0	0	0	0	0	0	0	0	0	**0**
C3	17	2	7	4	1	2	0	0	0	**33**
80 K103 3	83	16	24	3	2	1	2	0	1	**132**
80 K107 2	15	3	2	3	1	1	1	0	0	**26**
160 K107 2	101	26	23	16	8	4	12	4	1	**195**
160 K103 3	53	19	1	0	0	2	0	1	0	**76**
C1	45	38	16	12	2	5	6	7	2	**133**
80 K107 3	37	10	1	0	2	0	1	0	2	**53**
160 K103 2	13	6	1	0	1	0	1	0	0	**22**
80 K103 1	116	30	11	3	4	0	0	0	1	**165**
160 K107 3	72	11	3	1	1	1	1	1	1	**92**
C2	45	27	15	5	11	5	8	5	4	**125**

Table E.6. Rate of Release Calculations for 15-Minute Recovery

	Stamp 1	Stamp 2	Stamp 3	Stamp 4	Stamp 5	Stamp 6	Stamp 7	Stamp 8	Stamp 9
C3	1	0.1176	0.4118	0.2353	0.0588	0.1176	0.0000	0.0000	0.0000
C2	1	0.6000	0.3333	0.1111	0.2444	0.1111	0.1778	0.1111	0.0889
C1	1	0.8444	0.3556	0.2667	0.0444	0.1111	0.1333	0.1556	0.0444
80 K107 3	1	0.2703	0.0270	0.0000	0.0541	0.0000	0.0270	0.0000	0.0541
80 K107 2	1	0.2000	0.1333	0.2000	0.0667	0.0667	0.0667	0.0000	0.0000
80 K107 1	1	0.0000	0.0000	0.0000	0.0000	0.0000	0.0000	0.0000	0.0000
80 K103 3	1	0.1928	0.2892	0.0361	0.0241	0.0120	0.0241	0.0000	0.0120
80 K103 2	1	0.0000	0.0000	0.0000	0.0000	0.0000	0.0000	0.0000	0.0000
80 K103 1	1	0.2586	0.0948	0.0259	0.0345	0.0000	0.0000	0.0000	0.0086
160 K107 3	1	0.1528	0.0417	0.0139	0.0139	0.0139	0.0139	0.0139	0.0139
160 K107 2	1	0.2574	0.2277	0.1584	0.0792	0.0396	0.1188	0.0396	0.0099
160 K107 1	1	0.0000	0.0000	0.0000	0.0000	0.0000	0.0000	0.0000	0.0000
160 K103 3	1	0.3585	0.0189	0.0000	0.0000	0.0377	0.0000	0.0189	0.0000
160 K103 2	1	0.4615	0.0769	0.0000	0.0769	0.0000	0.0769	0.0000	0.0000
160 K103 1	1	0.0000	0.0000	0.0000	0.0000	0.0000	0.0000	0.0000	0.0000

Table E.7. Transferred CFUs for Stamp No. 1 of 15-Minute Recovery

	Avg	Std Dev
Control	35.7	13.2
80 K103	66.3	48.8
80 K107	17.7	14.8
160 K103	22.0	22.6
160 K107	57.7	42.5

Table E.8. Total CFUs Transferred for 15-Minute Recovery

	Avg	Std Dev
Control	97.0	45.4
80 K103	99.0	71.3
80 K107	26.7	21.2
160 K103	32.7	31.9
160 K107	95.7	79.7

Table E.9. Raw CFU Counts for 30-Minute Recovery

	Stamp 1	Stamp 2	Stamp 3	Stamp 4	Stamp 5	Stamp 6	Stamp 7	Stamp 8	Stamp 9	**Total**
80 K103 2	0	0	0	0	0	0	0	0	0	**0**
160 K103 1	2	0	0	0	0	0	0	0	0	**2**
80 K107 1	22	4	2	0	0	0	0	0	0	**28**
160 K107 1	44	3	0	0	0	0	0	0	0	**47**
C3	19	2	2	0	1	1	0	0	1	**26**
80 K103 3	11	0	0	0	1	0	0	0	0	**12**
80 K107 2	14	4	1	0	1	0	0	0	0	**20**
160 K107 2	30	4	3	1	2	1	0	1	0	**42**
160 K103 3	25	5	4	2	2	1	2	1	0	**42**
C1	70	21	10	7	13	8	6	2	4	**141**
80 K107 3	114	7	6	2	3	1	0	0	1	**134**
160 K103 2	125	14	7	8	2	2	3	2	1	**164**
80 K103 1	68	6	6	2	5	5	0	0	0	**92**
160 K107 3	96	10	4	0	0	1	0	0	0	**111**
C2	72	25	15	10	10	5	5	1	0	**143**

Table E.10. Rate of Release Calculations for 30-Minute Recovery

	Stamp 1	Stamp 2	Stamp 3	Stamp 4	Stamp 5	Stamp 6	Stamp 7	Stamp 8	Stamp 9
C3	1	0.1053	0.1053	0.0000	0.0526	0.0526	0.0000	0.0000	0.0526
C2	1	0.3472	0.2083	0.1389	0.1389	0.0694	0.0694	0.0139	0.0000
C1	1	0.3000	0.1429	0.1000	0.1857	0.1143	0.0857	0.0286	0.0571
80 K107 3	1	0.0614	0.0526	0.0175	0.0263	0.0088	0.0000	0.0000	0.0088
80 K107 2	1	0.2857	0.0714	0.0000	0.0714	0.0000	0.0000	0.0000	0.0000
80 K107 1	1	0.1818	0.0909	0.0000	0.0000	0.0000	0.0000	0.0000	0.0000
80 K103 3	1	0.0000	0.0000	0.0000	0.0909	0.0000	0.0000	0.0000	0.0000
80 K103 2	1	0.0000	0.0000	0.0000	0.0000	0.0000	0.0000	0.0000	0.0000
80 K103 1	1	0.0882	0.0882	0.0294	0.0735	0.0735	0.0000	0.0000	0.0000
160 K107 3	1	0.1042	0.0417	0.0000	0.0000	0.0104	0.0000	0.0000	0.0000
160 K107 2	1	0.1333	0.1000	0.0333	0.0667	0.0333	0.0000	0.0333	0.0000
160 K107 1	1	0.0682	0.0000	0.0000	0.0000	0.0000	0.0000	0.0000	0.0000
160 K103 3	1	0.2000	0.1600	0.0800	0.0800	0.0400	0.0800	0.0400	0.0000
160 K103 2	1	0.1120	0.0560	0.0640	0.0160	0.0160	0.0240	0.0160	0.0080
160 K103 1	1	0.0000	0.0000	0.0000	0.0000	0.0000	0.0000	0.0000	0.0000

Table E.11. Transferred CFUs for Stamp No. 1 of 30-Minute Recovery

	Avg	Std Dev
Control	53.7	24.5
80 K103	26.3	29.8
80 K107	50.0	45.4
160 K103	50.7	53.4
160 K107	56.7	28.4

Table E.12. Total CFUs Transferred for 30-Minute Recovery

	Avg	Std Dev
Control	103.3	54.7
80 K103	34.7	40.8
80 K107	60.7	52.0
160 K103	69.3	68.9
160 K107	66.7	31.4

APPENDIX F

10 μM PTFE-LN DATA

Table F.1. Raw CFU Counts for 15-Minute Recovery

	Stamp 1	Stamp 2	Stamp 3	Stamp 4	Stamp 5	Stamp 6	Stamp 7	Stamp 8	Stamp 9	**Total**
40 K103 2	56	11	5	4	3	1	1	0	1	**82**
80 K103 1	17	4	3	1	0	1	0	0	0	**26**
40 K107 1	25	6	10	5	1	0	1	0	0	**48**
80 K107 1	163	42	12	12	6	1	3	4	0	**243**
C3	142	61	61	27	17	11	10	4	2	**335**
40 K103 3	68	22	5	4	1	0	0	0	0	**100**
40 K107 2	50	12	6	1	1	0	0	0	1	**71**
80 K107 2	22	4	4	0	0	0	0	0	0	**30**
80 K103 3	53	8	6	2	1	0	0	0	0	**70**
C1	102	38	44	22	9	14	4	5	3	**241**
40 K107 3	31	6	6	3	1	0	1	0	0	**48**
80 K103 2	90	24	2	14	8	4	2	2	1	**147**
40 K103 1	34	15	2	2	2	2	1	0	0	**58**
80 K107 3	37	6	4	2	1	0	2	0	0	**52**
C2	53	4	6	5	4	1	0	1	0	**74**

Table F.2. Rate of Release Calculations for 15-Minute Recovery

	Stamp 1	Stamp 2	Stamp 3	Stamp 4	Stamp 5	Stamp 6	Stamp 7	Stamp 8	Stamp 9
C1	1	0.3725	0.4314	0.2157	0.0882	0.1373	0.0392	0.0490	0.0294
C2	1	0.0755	0.1132	0.0943	0.0755	0.0189	0.0000	0.0189	0.0000
C3	1	0.4296	0.4296	0.1901	0.1197	0.0775	0.0704	0.0282	0.0141
40 K103 1	1	0.4412	0.0588	0.0588	0.0588	0.0588	0.0294	0.0000	0.0000
40 K103 2	1	0.1964	0.0893	0.0714	0.0536	0.0179	0.0179	0.0000	0.0179
40 K103 3	1	0.3235	0.0735	0.0588	0.0147	0.0000	0.0000	0.0000	0.0000
40 K107 1	1	0.2400	0.4000	0.2000	0.0400	0.0000	0.0400	0.0000	0.0000
40 K107 2	1	0.2400	0.1200	0.0200	0.0200	0.0000	0.0000	0.0000	0.0200
40 K107 3	1	0.1935	0.1935	0.0968	0.0323	0.0000	0.0323	0.0000	0.0000
80 K103 1	1	0.2353	0.1765	0.0588	0.0000	0.0588	0.0000	0.0000	0.0000
80 K103 2	1	0.2667	0.0222	0.1556	0.0889	0.0444	0.0222	0.0222	0.0111
80 K103 3	1	0.1509	0.1132	0.0377	0.0189	0.0000	0.0000	0.0000	0.0000
80 K107 1	1	0.2577	0.0736	0.0736	0.0368	0.0061	0.0184	0.0245	0.0000
80 K107 2	1	0.1818	0.1818	0.0000	0.0000	0.0000	0.0000	0.0000	0.0000
80 K107 3	1	0.1622	0.1081	0.0541	0.0270	0.0000	0.0541	0.0000	0.0000

Table F.3. Transferred CFUs for Stamp No. 1 of 15-Minute Recovery

	Avg	Std Dev
Control	99.0	36.4
40 K103	52.7	14.1
40 K107	35.3	10.7
80 K103	53.3	29.8
80 K107	74.0	63.2

Table F.4. Total CFUs Transferred for 15-Minute Recovery

	Avg	Std Dev
Control	216.7	107.9
40 K103	80.0	17.2
40 K107	55.7	10.8
80 K103	81.0	50.0
80 K107	108.3	95.6

Table F.5. Raw CFU Counts for 30-Minute Recovery

	Stamp 1	Stamp 2	Stamp 3	Stamp 4	Stamp 5	Stamp 6	Stamp 7	Stamp 8	Stamp 9	**Total**
40 K103 2	0	0	0	0	0	0	0	0	0	**0**
80 K103 1	3	4	2	1	0	0	0	0	0	**10**
40 K107 1	33	8	5	3	2	1	0	0	0	**52**
80 K107 1	61	4	2	3	1	0	0	0	0	**71**
C3	8	2	3	2	1	1	0	1	0	**18**
40 K103 3	30	12	8	4	0	1	1	0	0	**56**
40 K107 2	57	20	10	2	2	1	0	0	0	**92**
80 K107 2	73	13	6	6	0	0	0	0	0	**98**
80 K103 3	59	38	19	5	3	5	0	0	0	**129**
C1	60	26	16	14	7	4	3	2	0	**132**
40 K107 3	63	15	6	7	3	2	0	0	1	**97**
80 K103 2	67	25	8	2	1	0	3	0	0	**106**
40 K103 1	90	28	16	7	5	1	2	0	0	**149**
80 K107 3	81	12	6	3	0	1	1	0	0	**104**
C2	83	40	26	9	4	8	2	2	0	**174**

Table F.6. Rate of Release Calculations for 30-Minute Recovery

	Stamp 1	Stamp 2	Stamp 3	Stamp 4	Stamp 5	Stamp 6	Stamp 7	Stamp 8	Stamp 9
C1	1	0.4333	0.2667	0.2333	0.1167	0.0667	0.0500	0.0333	0.0000
C2	1	0.4819	0.3133	0.1084	0.0482	0.0964	0.0241	0.0241	0.0000
C3	1	0.2500	0.3750	0.2500	0.1250	0.1250	0.0000	0.1250	0.0000
40 K103 1	1	0.3111	0.1778	0.0778	0.0556	0.0111	0.0222	0.0000	0.0000
40 K103 2	1	0.0000	0.0000	0.0000	0.0000	0.0000	0.0000	0.0000	0.0000
40 K103 3	1	0.4000	0.2667	0.1333	0.0000	0.0333	0.0333	0.0000	0.0000
40 K107 1	1	0.2424	0.1515	0.0909	0.0606	0.0303	0.0000	0.0000	0.0000
40 K107 2	1	0.3509	0.1754	0.0351	0.0351	0.0175	0.0000	0.0000	0.0000
40 K107 3	1	0.2381	0.0952	0.1111	0.0476	0.0317	0.0000	0.0000	0.0159
80 K103 1	1	1.3333	0.6667	0.3333	0.0000	0.0000	0.0000	0.0000	0.0000
80 K103 2	1	0.3731	0.1194	0.0299	0.0149	0.0000	0.0448	0.0000	0.0000
80 K103 3	1	0.6441	0.3220	0.0847	0.0508	0.0847	0.0000	0.0000	0.0000
80 K107 1	1	0.0656	0.0328	0.0492	0.0164	0.0000	0.0000	0.0000	0.0000
80 K107 2	1	0.1781	0.0822	0.0822	0.0000	0.0000	0.0000	0.0000	0.0000
80 K107 3	1	0.1481	0.0741	0.0370	0.0000	0.0123	0.0123	0.0000	0.0000

Table F.7. Transferred CFUs for Stamp No. 1 of 30-Minute Recovery

	Avg	Std Dev
Control	50.3	31.4
40 K103	40.0	37.4
40 K107	51.0	13.0
80 K103	43.0	28.5
80 K107	71.7	8.2

Table F.8. Total CFUs Transferred for 30-Minute Recovery

	Avg	Std Dev
Control	108.0	65.9
40 K103	68.3	61.5
40 K107	80.3	20.1
80 K103	81.7	51.5
80 K107	91.0	14.4

APPENDIX G

TEMPERATURE-BASED RECOVERY DATA

Table G.1. Raw CFU Counts Listed as Temperature/Volume/Krytox/Replicate Number

	Stamp 1	Stamp 2	Stamp 3	Stamp 4	Stamp 5	Stamp 6	Stamp 7	Stamp 8	Stamp 9	**Total**
40 Control 1	0	0	0	0	0	0	0	0	0	**0**
40 80µL K103 1	0	0	0	0	0	0	0	0	0	**0**
40 160µL K103 1	0	0	0	0	0	0	0	0	0	**0**
4 Control 1	14	7	6	3	3	1	0	0	1	**35**
4 80µL K103 1	11	3	2	2	1	0	0	0	0	**19**
4 160µL K103 1	84	47	12	9	4	2	4	1	1	**164**
26 Control 1	0	0	0	0	0	0	0	0	0	**0**
26 80µL K103 1	13	4	1	2	0	0	0	1	0	**21**
26 160µL K103 1	0	0	0	0	0	0	0	0	0	**0**
26 Control 2	0	0	0	0	0	0	0	0	0	**0**
26 80µL K103 2	76	17	5	4	1	2	0	1	1	**107**
26 160µL K103 2	10	1	1	1	0	0	0	0	0	**13**
40 Control 2	0	0	0	0	0	0	0	0	0	**0**
40 80µL K103 2	0	0	0	0	0	0	0	0	0	**0**
40 160µL K103 2	0	0	0	0	0	0	0	0	0	**0**
4 Control 2	35	15	14	1	2	3	1	0	2	**73**
4 80µL K103 2	42	6	7	3	1	2	0	0	2	**63**
4 160µL K103 2	30	14	1	6	3	4	3	2	2	**65**
4 Control 3	47	33	12	3	10	2	3	2	0	**112**
4 80µL K103 3	30	17	4	1	0	0	0	1	0	**53**
4 160µL K103 3	49	27	14	10	5	5	5	1	4	**120**
26 Control 3	90	22	10	10	10	1	2	0	4	**149**
26 80µL K103 3	0	0	0	0	0	0	0	0	0	**0**
26 160µL K103 3	1	0	0	0	0	0	0	0	0	**1**
40 Control 3	0	0	0	0	0	0	0	0	0	**0**
40 80µL K103 3	0	0	0	0	0	0	0	0	0	**0**
40 160µL K103 3	0	0	0	0	0	0	0	0	0	**0**

Table G.2. CFU Analysis Grouped by Temperature

	Stamp 1	Stamp 2	Stamp 3	Stamp 4	Stamp 5	Stamp 6	Stamp 7	Stamp 8	Stamp 9	**Total**
4 Control 1	14	7	6	3	3	1	0	0	1	**35**
4 Control 2	35	15	14	1	2	3	1	0	2	**73**
4 Control 3	47	33	12	3	10	2	3	2	0	**112**
4 80µL K103 1	11	3	2	2	1	0	0	0	0	**19**
4 80µL K103 2	42	6	7	3	1	2	0	0	2	**63**
4 80µL K103 3	30	17	4	1	0	0	0	1	0	**53**
4 160µL K103 1	84	47	12	9	4	2	4	1	1	**164**
4 160µL K103 2	30	14	1	6	3	4	3	2	2	**65**
4 160µL K103 3	49	27	14	10	5	5	5	1	4	**120**
26 Control 1	0	0	0	0	0	0	0	0	0	**0**
26 Control 2	0	0	0	0	0	0	0	0	0	**0**
26 Control 3	90	22	10	10	10	1	2	0	4	**149**
26 80µL K103 1	13	4	1	2	0	0	0	1	0	**21**
26 80µL K103 2	76	17	5	4	1	2	0	1	1	**107**
26 80µL K103 3	0	0	0	0	0	0	0	0	0	**0**
26 160µL K103 1	0	0	0	0	0	0	0	0	0	**0**
26 160µL K103 2	10	1	1	1	0	0	0	0	0	**13**
26 160µL K103 3	1	0	0	0	0	0	0	0	0	**1**
40 Control 1	0	0	0	0	0	0	0	0	0	**0**
40 Control 2	0	0	0	0	0	0	0	0	0	**0**
40 Control 3	0	0	0	0	0	0	0	0	0	**0**
40 80µL K103 1	0	0	0	0	0	0	0	0	0	**0**
40 80µL K103 2	0	0	0	0	0	0	0	0	0	**0**
40 80µL K103 3	0	0	0	0	0	0	0	0	0	**0**
40 160µL K103 1	0	0	0	0	0	0	0	0	0	**0**
40 160µL K103 2	0	0	0	0	0	0	0	0	0	**0**
40 160µL K103 3	0	0	0	0	0	0	0	0	0	**0**

Table G.3. Rate of Release Calculations

	Stamp 1	Stamp 2	Stamp 3	Stamp 4	Stamp 5	Stamp 6	Stamp 7	Stamp 8	Stamp 9
4 Control 1	1.000	0.500	0.429	0.214	0.214	0.071	0.000	0.000	0.071
4 Control 2	1.000	0.429	0.400	0.029	0.057	0.086	0.029	0.000	0.057
4 Control 3	1.000	0.702	0.255	0.064	0.213	0.043	0.064	0.043	0.000
4 80µL K103 1	1.000	0.273	0.182	0.182	0.091	0.000	0.000	0.000	0.000
4 80µL K103 2	1.000	0.143	0.167	0.071	0.024	0.048	0.000	0.000	0.048
4 80µL K103 3	1.000	0.567	0.133	0.033	0.000	0.000	0.000	0.033	0.000
4 160µL K103 1	1.000	0.560	0.143	0.107	0.048	0.024	0.048	0.012	0.012
4 160µL K103 2	1.000	0.467	0.033	0.200	0.100	0.133	0.100	0.067	0.067
4 160µL K103 3	1.000	0.551	0.286	0.204	0.102	0.102	0.102	0.020	0.082
26 Control 1	1.000	0.000	0.000	0.000	0.000	0.000	0.000	0.000	0.000
26 Control 2	1.000	0.000	0.000	0.000	0.000	0.000	0.000	0.000	0.000
26 Control 3	1.000	0.244	0.111	0.111	0.111	0.011	0.022	0.000	0.044
26 80µL K103 1	1.000	0.308	0.077	0.154	0.000	0.000	0.000	0.077	0.000
26 80µL K103 2	1.000	0.224	0.066	0.053	0.013	0.026	0.000	0.013	0.013
26 80µL K103 3	1.000	0.000	0.000	0.000	0.000	0.000	0.000	0.000	0.000
26 160µL K103 1	1.000	0.000	0.000	0.000	0.000	0.000	0.000	0.000	0.000
26 160µL K103 2	1.000	0.100	0.100	0.100	0.000	0.000	0.000	0.000	0.000
26 160µL K103 3	1.000	0.000	0.000	0.000	0.000	0.000	0.000	0.000	0.000
40 Control 1	1.000	0.000	0.000	0.000	0.000	0.000	0.000	0.000	0.000
40 Control 2	1.000	0.000	0.000	0.000	0.000	0.000	0.000	0.000	0.000
40 Control 3	1.000	0.000	0.000	0.000	0.000	0.000	0.000	0.000	0.000
40 80µL K103 1	1.000	0.000	0.000	0.000	0.000	0.000	0.000	0.000	0.000
40 80µL K103 2	1.000	0.000	0.000	0.000	0.000	0.000	0.000	0.000	0.000
40 80µL K103 3	1.000	0.000	0.000	0.000	0.000	0.000	0.000	0.000	0.000
40 160µL K103 1	1.000	0.000	0.000	0.000	0.000	0.000	0.000	0.000	0.000
40 160µL K103 2	1.000	0.000	0.000	0.000	0.000	0.000	0.000	0.000	0.000
40 160µL K103 3	1.000	0.000	0.000	0.000	0.000	0.000	0.000	0.000	0.000

APPENDIX H

HEPA-LN DATA

Table H.1. Raw CFU Counts for First HEPA Aerosolization Data Set

	Stamp 1	Stamp 2	Stamp 3	Stamp 4	Stamp 5	Stamp 6	Stamp 7	Stamp 8	Stamp 9	**Total**
B HEPA 1	12	10	8	10	4	2	4	2	2	**54**
160 HEPA 1	68	47	31	42	24	0	19	0	0	**231**
B HEPA 2	38	50	66	53	60	91	70	54	49	**531**
160 HEPA 2	43	47	32	14	23	18	10	4	3	**194**
B HEPA 3	8	7	14	10	15	15	1	10	9	**89**
160 HEPA 3	47	22	16	14	4	4	1	4	0	**112**

Table H.2. Rate of Release Calculations for First HEPA Data Set

	Stamp 1	Stamp 2	Stamp 3	Stamp 4	Stamp 5	Stamp 6	Stamp 7	Stamp 8	Stamp 9
B HEPA 3	1	0.8750	1.7500	1.2500	1.8750	1.8750	0.1250	1.2500	1.1250
B HEPA 2	1	1.3158	1.7368	1.3947	1.5789	2.3947	1.8421	1.4211	1.2895
B HEPA 1	1	0.8333	0.6667	0.8333	0.3333	0.1667	0.3333	0.1667	0.1667
160 HEPA 3	1	0.4681	0.3404	0.2979	0.0851	0.0851	0.0213	0.0851	0.0000
160 HEPA 2	1	1.0930	0.7442	0.3256	0.5349	0.4186	0.2326	0.0930	0.0698
160 HEPA 1	1	0.6912	0.4559	0.6176	0.3529	0.0000	0.2794	0.0000	0.0000

Table H.3. Transferred CFUs for Stamp No. 1 of First HEPA Data Set

	Avg	**Std Dev**
Control	19.3	13.3
160 HEPA	52.7	11.0

Table H.4. Total CFUs Transferred for First HEPA Data Set

	Avg	**Std Dev**
Control	224.7	217.1
160 HEPA	179.0	49.7

Table H.5. Raw CFU Counts for Second HEPA Aerosolization Data Set

	Stamp 1	Stamp 2	Stamp 3	Stamp 4	Stamp 5	Stamp 6	Stamp 7	Stamp 8	Stamp 9	**Total**
B HEPA 1	0	6	4	5	2	4	3	0	3	**6**
160 HEPA 1	32	26	15	15	15	9	8	11	7	**138**
B HEPA 2	3	3	4	5	3	1	3	0	0	**22**
160 HEPA 2	14	4	14	7	5	2	5	1	1	**53**
B HEPA 3	4	20	19	12	16	13	13	7	7	**111**
160 HEPA 3	34	23	14	23	16	10	5	2	5	**132**

Table H.6. Rate of Release Calculations for Second HEPA Data Set

	Stamp 1	Stamp 2	Stamp 3	Stamp 4	Stamp 5	Stamp 6	Stamp 7	Stamp 8	Stamp 9
B HEPA 3	1	5.0000	4.7500	3.0000	4.0000	3.2500	3.2500	1.7500	1.7500
B HEPA 2	1	1.0000	1.3333	1.6667	1.0000	0.3333	1.0000	0.0000	0.0000
B HEPA 1	1	6.0000	4.0000	5.0000	2.0000	4.0000	3.0000	0.0000	3.0000
160 HEPA 3	1	0.6765	0.4118	0.6765	0.4706	0.2941	0.1471	0.0588	0.1471
160 HEPA 2	1	0.2857	1.0000	0.5000	0.3571	0.1429	0.3571	0.0714	0.0714
160 HEPA 1	1	0.8125	0.4688	0.4688	0.4688	0.2813	0.2500	0.3438	0.2188

Table H.7. Transferred CFUs for Stamp No. 1 of Second HEPA Data Set

	Avg	**Std Dev**
Control	2.7	1.2
160 HEPA	26.7	9.0

Table H.8. Total CFUs Transferred for Second HEPA Data Set

	Avg	**Std Dev**
Control	46.3	46.2
160 HEPA	107.7	38.7

APPENDIX I

CNFM-LN DATA

Table I.1. Raw CFU Counts

	Stamp 1	Stamp 2	Stamp 3	Stamp 4	Stamp 5	Stamp 6	Stamp 7	Stamp 8	Stamp 9	**Total**
B CNFM 1	0	0	1	0	0	0	0	0	0	**1**
40 CNFM 1	0	0	1	0	0	0	1	1	0	**3**
B CNFM 2	50	61	34	30	27	13	12	0	0	**227**
40 CNFM 2	16	17	12	13	17	10	9	24	9	**127**
B CNFM 3	66	65	53	78	53	44	27	14	0	**400**
40 CNFM 3	36	56	31	38	40	38	28	30	10	**307**

Table I.2. Rate of Release Calculations

	Stamp 1	Stamp 2	Stamp 3	Stamp 4	Stamp 5	Stamp 6	Stamp 7	Stamp 8	Stamp 9
B CNFM 3	1	0.9848	0.8030	1.1818	0.8030	0.6667	0.4091	0.2121	0.0000
B CNFM 2	1	1.2200	0.6800	0.6000	0.5400	0.2600	0.2400	0.0000	0.0000
B CNFM 1	1	0.0000	1.0000	0.0000	0.0000	0.0000	0.0000	0.0000	0.0000
40 CNFM 3	1	1.5556	0.8611	1.0556	1.1111	1.0556	0.7778	0.8333	0.2778
40 CNFM 2	1	1.0625	0.7500	0.8125	1.0625	0.6250	0.5625	1.5000	0.5625
40 CNFM 1	1	0.0000	1.0000	0.0000	0.0000	0.0000	1.0000	1.0000	0.0000

Table I.3. Transferred CFUs for Stamp No. 1

	Avg	**Std Dev**
Control	38.7	28.1
40 CNFM	17.3	14.7

Table I.4. Total CFUs Transferred

	Avg	**Std Dev**
Control	209.3	163.4
40 CNFM	145.7	124.8

APPENDIX J

CHEMICAL EXTRACTION PROTOCOL AND NOTED FAILURES

A method was developed to release the captured aerosolized *E. coli* following the aerosolization protocol with dry control and HEPA-LNs from **Section 6.3.3.** Following the 15-minute recovery period, the filter would be placed in 15 mL conical tube with 0.5 mL of Novec 7100 Engineering Fluid (3M) and 2.0 mL of 1× PBS. The tube was shaken by hand for 60 s, as the two liquids are immiscible and difficult to form an emulsion. This was conducted so the fluorinated Novec solvent would strip away the Krytox 103 PFPE and associated bacteria from the fibers. Then, the conical tube was returned to the vertical position for 5 minutes, allowing the two liquid phases to separate and the negatively charged bacteria to potentially associate with the PBS over the fluorinated solvent. For CFU analysis, 200 μL from each liquid was plated onto separate LB agar plates and incubated for 24 h at 37 °C. For all experiments, 0 CFUs were grown on the LB agar plates that were samples from the fluorinated Novec solvent. Cultured plates from the PBS were also well-below expectations and highly varied. One potential reason for this method's failures is due to the reliance on culturing bacteria after association with two-fluorinated compounds, potentially interfering with their growth on agar plates. Future experiments with reovirus using real-time polymerase chain reaction and infectivity assays will shed light on this method's potential with viral pathogens and new analytical techniques.

BIOGRAPHY OF THE AUTHOR

Daniel Paul Regan was born and raised in Parma, Ohio and graduated from Parma Senior High in 2013. He majored in bioprocess engineering at Miami University, where his experiences with the Government Relations Network, the Engineering-in-Germany study abroad program, and researching under Dr. Michael Kennedy highlighted his time as an undergraduate. After earning a Bachelor of Science in Engineering in 2017, he began his doctoral studies at the University of Maine. Through the Graduate School of Biomedical Science and Engineering, Dan joined Dr. Caitlin Howell's research group working on liquid-infused surfaces. Driven by his passion to improve the nation's biodefense capabilities, Dan applied his research towards applications of biological sample handling and bioaerosol surveillance. As a result of his research efforts, Dan received Dr. Susan J. Hunter Research Impact Award, the College of Engineering's Graduate Assistant Research Award, and two Maine Space Grant Consortium Graduate Summer Fellowships. After receiving his degree, Dan will be joining Dr. Kenan Fears at the U.S. Naval Research Laboratory as an NRC Postdoctoral Research Associate. Dan is a candidate for the Doctor of Philosophy degree in Biomedical Engineering from the University of Maine in May 2021.